CONTROL OF PLASMA ETCHING OF SEMICONDUCTOR SURFACES

by

Hongbin Zhu

A Dissertation Submitted to the Faculty of the

DEPARTMENT OF CHEMICAL AND ENVIRONMENTAL ENGINEERING

In Partial Fulfillment of the Requirements
For the Degree of

DOCTOR OF PHILOSOPHY

WITH A MAJOR IN CHEMICAL ENGINEERING
In the Graduate College

THE UNIVERSITY OF ARIZONA

2 0 0 5

THE UNIVERSITY OF ARIZONA
GRADUATE COLLEGE

As members of the Final Examination Committee, we certify that we have read the dissertation prepared by Hongbin Zhu
entitled Control of Plasma Etching of Semiconductor Surfaces
and recommend that it be accepted as fulfilling the dissertation requirement for the Degree of Doctor of Philosophy.

Date: 21 Nov 2005
Anthony J. Muscat

Date: 21 Nov 2005
Farhang Shadman

Date: 21 Nov 2005
A. Eduardo Saez

Date: 21 Nov 2005
Steven Dvorak

Date: 21 Nov 2005
Harold G. Parks

Final approval and acceptance of this dissertation is contingent upon the candidate's submission of the final copies of the dissertation to the Graduate College.

I hereby certify that I have read this dissertation prepared under my direction and recommend that it be accepted as fulfilling the dissertation requirement.

Date: 21 Nov 2005
Dissertation Director: Anthony J. Muscat

STATEMENT BY AUTHOR

This dissertation has been submitted in partial fulfillment of requirements for an advanced degree at The University of Arizona and is deposited in the University Library to be made available to borrowers under rules of the Library.

Brief quotations from this dissertation are allowable without special permission, provided that accurate acknowledgment of source is made. Requests for permission for extended quotation from or reproduction of this manuscript in whole or in part may be granted by the head of the major department or the Dean of the Graduate College when in his or her judgment the proposed use of the material is in the interests of scholarship. In all other instances, however, permission must be obtained from the author.

SIGNED: _____

Hongbin Zhu

ACKNOWLEDGEMENTS

I would like to thank my advisor Professor Anthony J. Muscat and my co-advisor Dr. Michael J. Schabel;

I would like to thank all my groups memebers, especially Dr. Casey Finstad for his numerous discussion and direction in vacuum engineering, and Mr. Gerardo Montanto for his help in setting reaction system.

I would like to thank MEL support, Ms. Sarah Dahl and Dr. Victor Wells, and our mechanic technician Mr. Lorenzo Lujan.

Part of the work is supported by DOE grant DE-FG03-00ER54581.

Finally I would like to thank our department and our research center, for their generous support.

DEDICATION

To my family, for their love, support, and patience. Especially to my wife, Mei, for the happiness we enjoyed, for the difficult time we shared.

TABLE OF CONTENTS

TABLE OF CONTENTS – *Continued*

TABLE OF CONTENTS – *Continued*

LIST OF FIGURES

LIST OF FIGURES – *Continued*

LIST OF FIGURES – *Continued*

LIST OF FIGURES – *Continued*

LIST OF FIGURES – *Continued*

LIST OF FIGURES – *Continued*

LIST OF TABLES

ABSTRACT

The current semiconductor device manufacturing requires more strict control of plasma etching. In this research, plasma etching was investigated through gas phase characterization and interface reactions. Hydrogen and nitrogen were added to Ar plasmas to manipulate the electro-physical properties that were measured by a Langmuir probe system. Hydrogen addition modified the EEDF (electron energy distribution function) by increasing the electrons in high energy range. Adding N_2 formed a strong bi-Maxwellian distribution. Gas addition caused the transition between ohmic and stochastic heating. Ar-CH_4-H_2 and Ar-N_2-H_2 plasmas were also tested. Hydrogen atom beam was used on porous silicon dioxide based low-*k* films to remove silanol groups that were generated due to the damage of films during pattern transfer. At H_2 atom beam process at 150 °C moved close to 60% silanol groups were removed in less than 3 min with an etching rate of 15 Å/min. The apparent activation energy was 2.4 kcal/mol. Hydrogen atoms reacted with Si-O-Si and methyl groups. The etching mechanisms of CH_4/H_2/Ar plasma for InP were analyzed by a beam reactor system. Sputtering yield was measured, threshold energy was approximately 60 eV. Inert ion beam assisted chemical reactions gave higher etching rate. The CH_4 concentration had no strong effect on etching rate after 5%. Etching rate was not sensitive to temperature up to 150 °C. The adsorption of methyl groups to the surface was proposed as rate limiting step. Chemical reaction effectively reduced the surface roughness.

CHAPTER 1

Introduction

Plasma etching has been widely used for semiconductor device manufacturing. The ability to reach anisotropic etching makes it extremely important for modern semiconductor processes to form interconnect structures. With increased transistor density, more complicated interconnect structure is required, which needs more strict control of plasma etching. This means better control of etching rate, selectivity, uniformity, surface quality, reproducibility, and directionality.[7] Therefore, it is important to understand the details of plasma physics and chemistry. However, plasma etching is a challenging research subject due to its complexity. In the gas phase, hundreds of reactions can happen in parallel. On the interface, the ion incidence makes the surface reactions difficult for analysis. In general, plasma parameters are nonlinearly related with process parameters, which makes the system difficult to control. Therefore, it is necessary to simplify the system for fundamental mechanism analysis.

In this research, the analysis of plasma etching was approached through two steps to simplify the process yet still allowing a systematical investigation. The first step focused on the characterization and analysis of plasma properties in the gas phase with gas addition. The second step focused on the investigation of the reactions on the gas-solid interface. Three tasks were finished to improve the understanding of plasma etching according to this strategy.

In task 1, the research focused on the manipulation of electro-physical properties in a capacitively coupled plasma by gas addition. Three widely used additive gases: Ar, H_2, and N_2 were investigated in a GEC (gas electronic conference) chamber by Langmuir probe. General research of gas addition in plasma etching mainly focused on chemical reactions. In this work, the effect of gas addition on electro-physical properties was stressed and discussed in detail. The main work of task 1 is discussed in detail in chapter 3. Although Ar, H_2, and N_2 plasmas individually has been widely discussed, this is the first

systematical work in analysis of electro-physical properties change with gas concentration modification.

In task 2, the research focused on the chemical reactions on the plasma-solid interface; by removing ion incidence the plasma-solid interface reactions were simplified. A beam reactor system was built for this research. Hydrogen atom beam was used to remove silanol groups from ashed *p*-MSQ (porous-methylsilsesquioxane) film. Different experimental conditions were explored in order to obtain effective removal but without over etching the film. The main work of task 2 is discussed in detail in chapter 5. To our knowledge, this is the first work in investigating H atom reaction with silanol groups on *p*-MSQ films. It also enhanced the general understanding of plasma-solid interface reactions.

In task 3, the beam reactor was upgraded to contain both ion beam and atom beam. The combination of ion beam and atom beam provides better approximation for ion assisted etching, which is the most important format for plasma etching. At the same time, the individual ion and atom beam provides the advantage of independent control of incident ion flux, ion energy, and reactive neutrals, which simplifies the investigation of plasma etching. The InP etching by CH_4/H_2/Ar chemistry was chosen and analyzed in detail to obtain a better understanding of ion incidence assisted plasma-InP interface reactions. Through a comprehensive and systematic investigation of InP etching mechanisms, the adsorption was identified as rate limiting step. The main work of task 3 is discussed in detail in chapter 6. It provides an improved understanding of ion functions for general plasma etching with adsorption control.

Through these three tasks, plasma etching has been systematically investigated through gas phase characterization, interface chemical reaction, and interface ion assisted chemical reaction. It is expected that through this work improved understanding of plasma etching process can be obtained.

CHAPTER 2

Plasma Characterization and Langmuir Probe

2.1 Introduction

2.1.1 An introduction of the Langmuir probe

The Langmuir probe, also called the electrostatic probe, was first developed by Langmuir and Mott-Smith in the 1920s.[8] The simplest probe system is composed of a conductive wire and an external circuit. The conductive wire works as a probe and is located inside the plasma to collect ions and electrons. The external circuit is connected to the probe. The circuit provides sweeping voltage and measures the correspondent current. Fig. 2.1 presents a picture of our probe system in an Ar plasma. The light region in the photograph between the two electrodes is the glow discharge. The probe was located in this region. Fig.2.2 presented the schematic diagram of the probe and plasma system. The RF power propagated into the plasma chamber through the matching unit and coupled capacitor. The probe voltage source provided the sweeping voltage to the tuned probe and the responding current was measured. The following paragraph qualitatively describes the operation and analysis principles of the probe system and along with a more detailed description of the plasma system.

The probe in a plasma accepts charged particles impinging from both positively charged ions and negatively charged electrons. Assuming that the probe is a perfect non-reflection charge collector, and ion bombardment does not generate secondary emission electrons, then the probe will collect all of the charged particles that collide with it. A negative potential barrier between the probe and the bulk plasma will build up to balance the ion and electron flux. Surrounding the probe, a sheath region forms. A drop in potential difference is concentrated in this region. Once the charged particles cross the sheath edge, the negatively charged electrons are retarded and the positively charged ions are accelerated by this potential barrier. Therefore, the floating potential is defined

as the potential that probe receives equal electron and ion flux. If sweeping voltages are applied to the probe, the probe deviates from its floating state and forms a net current in the external circuit. A current gauge is used to read current for every voltage. Then an $I-V$ characteristic curve is obtained. A typical $I-V$ curve for an Ar plasma system is presented in Fig. 2.3.

The $I-V$ curve has three different regions. When the probe bias voltage V_B is higher than V_p (plasma potential), electrons are drawn to the probe and ions are expelled. This region is called the electron saturation region. When V_B is lower than V_f (floating potential), ion current begins to dominate the measured current. This region is called the ion saturation region. The region between V_f and V_p is called the electron retardation region because in this region, electrons are retarded by V_B and is the dominant component of the measured current. With certain physical assumptions and mathematical processes, plasma parameters such as plasma potential (V_p), floating potential (V_f), electron temperature (T_e), ion temperature (T_i), electron density (n_e), ion density (n_i), electron energy distribution function (EEDF), or electron energy probability function (EEPF), can be derived from the $I-V$ characteristic curve. The detailed method of parameters deduction is presented in following section

The Langmuir probe provides an effective method to measure plasma parameters with a relatively simple experimental set up. After its initial development by Langmuir and Mott-Smith, it has drawn a great amount of discussion in the the fields of probe structure and theoretical work. The continued development of plasma theory and computer technology has advanced the techniques for the Langmuir probe.[9, 10, 11, 12]

2.1.2 Langmuir Probe for RF Plasma

Radio frequency (RF, mostly at 13.56 MHz) powered plasma systems are widely used in the semiconductor industry. Compared with DC plasma, the RF systems have additional difficulties in applying Langmuir probe technology. Fig. 2.4 illustrates a simplified equivalent capacitively coupled RF plasma circuit diagram, where C_s and R_s stand for sheath region, C_p and R_p are for bulk plasma, C_w and R_w stand for wall contact. Several major problems that are addressed by Godyak are briefly discussed here.[10]

- RF distortion. As illustrated in the plasma equivalent circuit, the RF power source brings intrinsic RF oscillation of the plasma potential with respect to the ground. This oscillation can further be amplified by the nonlineality of the probe sheath. The result is serious distortion with respect to the collected DC current signal.

- Low-frequency noise and drift. It may originate from the instability of the supplied RF voltage, or from the instabilities of the plasma itself. The internal random fluctuations of plasma can also contribute to this problem.

- Probe contamination. During the measurement it is possible that a impurity layer can be deposited on the probe tip. This deposited layer modifies the probe work function, therefore affecting the collected current signal. If conductive materials are deposited on the probe holder, the collection area can be changed.

Different technologies were developed for RF plasma measurement. The structure and the equivalent circuit of the probe that was used in current research (Scientific System Inc.) are illustrated in Fig. 2.5 and Fig. 2.6. This design used several widely discussed and accepted technologies.[13] Those features are addressed in the following paragraph.

- A filter is installed to remove the RF power oscillation. The filter is composed of two mini-inductors. These inductors are tuned to the 1st and 2nd harmonic power frequency (13.56 and 27.12 MHz). Therefore, the power oscillation causes very high impedance in the filter and is then blocked. The filter is located very close to the collecting tip to avoid possible parasitic capacitance. The filter is indicated in the equivalent circuit by L_1, C_1. The parasitic capacitance is indicated by C_s.

- A metal sleeve is added to the probe holder. The metal sleeve works as a capacitor (C_2). This capacitor helps to reduce the sheath impedance of the probe to the plasma. The sheath impedance is indicated by the combination of C_p and R_p. The combination of C_2 with Z_p reduces the impedance of probe to plasma. It makes the probe more sensitive in receiving current signal.

- A reference probe is added to the collecting probe. The signal collected by the reference probe is amplified through an pre-amplifier and is used as compensation for the collecting probe. It helps in reducing the low-frequency noise and drift.

- Probe *in-situ* cleaning. The ECU (electronic circuit unit) can send a pulse voltage to the probe tip during the measurement. A saturated electron current will be drawn by this voltage and burns the tip to white-red. The possible deposited materials can then be burned out and the probe will be cleaned. Besides the *in-situ* cleaning, there is a recess gap between the probe tip and the holder which helps to avoid direct contact between the probe and its ceramic holder.

- The ECU has very low resistance. It can provide a sweep from $-100V$ to $100V$ in mini-seconds. The fast sweeping speed can suppress the noise from the plasma system.

- The dimensions of the probe and its holder need to be small. Smaller dimensions are useful in reducing the interruption of the plasma, but the dimensions need to be large enough to contain the inductor and to provide the space for air cooling.

This probe system has been widely used in the plasma research community and has proven itself to be an effective and reliable tool.[14, 15, 16, 17]

2.2 Experimental Setup and Data Processing

2.2.1 GEC System in Capacitive and Inductive Mode

Fig. 2.7 shows a schematic of the experimental arrangement and the system components. Fig. 2.8 shows the photo of the whole system. The GEC reference cell is a well-known system for plasma research, a detailed description of the cell is available by publication [18] and NIST website (www.nist.gov). The plasma was powered by a 13.56 MHz RF power supply (ENI power system Inc. OEM-6) through bottom electrode. The system used a manual matching network to reduce the reflected power. A through-line watt meter (Bird electronics Corp.) was used for measuring the RF power. In experiments the

reflected power was kept below 5% of input power. In the following sections, the input power refers to the net input power, in which the reflected power was subtracted from input power.

The base pressure for the cell was 2.0×10^{-7} Torr. Pressures during experiments were monitored by a Baratron absolute pressure gauge (MKS 220). Three MFCs (mass flow-rate controler) were used to control the gas flow rate seperately. The MFCs together with the throttle valve between the chamber and turbo pump adjusted the chamber pressure. A Balzers QMG420 mass spectrometer was used for leak detection and plasma characterization.

The Langmuir probe has been extensively used for plasma characterization. Design of the probe system and the data analysis have been widely discussed.[8, 12, 9, 7, 19] A commercially available RF-compensated probe system (SmartProbe, Scientific Systems Inc.) was used in this research. A detailed discussion of this probe system design and the theorectical background of the data analysis are available,[20, 21, 13] and discussed in following section. The parameters of electron density (n_e), ion density (n_i), electron temperature or average electron kinetic energy (T_e), floating potential (V_f), plasma potential (V_p), and electron energy distribution function (EEDF) were measured through the probe. For convenience to compare with Maxwellian distribution and other experimental results in the literature, the EEPF (electron energy probability function) was used in following sections. It was obtained by the Druyvesteyn method [10]

$$f(\epsilon) = \frac{2I"}{eA}\left(\frac{2m\epsilon}{e}\right)^{1/2} \tag{2.1}$$

where I" is the second order deriative of current and probe sweeping voltage, A is the probe collecting area, ϵ is the electron kinetic energy. The relationship between EEDF [$F(\epsilon)$] and EEPF [$f(\epsilon)$] is defined as $F(\epsilon) = \epsilon^{1/2} f(\epsilon)$. This probe system has been widely used in the plasma research community and has been demonstrated in GEC cells.[14, 15, 16, 17] During our experiments, the probe tip was located horizontally at the center of the electrode and vertically 1 cm from the top electrode.

Ar plasma was regularly measured to serve as the criterion of chamber and probe conditions. The plasma parameters for Ar were compared and agreed with literature.[21,

22, 23, 24, 19, 25] The probe tip was changed regularly. The gases that were used in current work were: Ar, US Airweld Speciality Gas, ultra high purity; H_2, Matheson Tri-Gas, 99.9999%; N_2, Nellcor Puritan Bennett, ultra high purity; CH_4, Matheson Trig-Gas, 99.999%.

This GEC system had been modified to an ICP (inductive coupled plasma) system. To use the GEC chamber as an ICP system, the top electrode was removed and was replaced with an glass window. A 5-turn copper coil was used as the antenna to inductively couple the power to the plasma. In order to reduce the capacitively coupled power, a Faraday shield was used between the glass window and the copper coil.

2.2.2 SmartProbe and Its Data Processing

The probe system in current research has a built-in program that calculates plasma parameters from a measured $I - V$ curve. The program routines are based on simple probe theory and the Laframboise theory. The routine based on simple probe theory provides a quick calculation of V_f, V_p, T_e, and provides an initial estimation for more complicated routines based on the Laframboise theory.[21] In the simple probe theory, V_f is the potential at $I = 0$ since at floating potential $I_e = I_i$, the ion current and electron current cancel each other. V_p is decided by $(d^2I/dV^2)_{V=V_p} = 0$ because dI/dV has a maximum at $V = V_p$. This can be explained through the $I - V$ curve in Fig. 2.3. When $V \geq V_p$, the $I - V$ curve enters into the electron saturation region, current increases drastically and resulted a maximum for dI/dV. T_e is decided by $I(V_p)/\int I(V) = e/T_e$ since this fraction corresponds to the average electron energy.

Laframboise theory uses a more complicated OML(orbital motion limited) method. This method was first developed by Langmuir and Mott-Smith.[8] It is based on the analysis of ion orbitals inside the sheath region. More detailed discussion about OML method and Laframboise theory are available in the literature.[9] A brief explanation of these program routines is illustrated in the following section. More detailed explanations are available in literature.[20]

Ion and electron current are expressed as

$$I_+(V)/I_{0+} = f\left(R_p/\lambda_d, \chi\right), \chi < 0 \tag{2.2}$$

$$I_e(V)/I_{0e} = f\left(R_p/\lambda_d, \chi\right), \chi > 0 \tag{2.3}$$

where $I_+(V)$ is the ion current function, $I_e(V)$ is the electron current function. I_{0+} is the random thermal ion current at plasma potential, I_{0e} is the random thermal electron current at plasma potential. The scaling factor is defined as $\chi = e(V - V_p)/kT_e$. $f\left(R_p/\lambda_d, \chi\right)$ is called expansion factor and is calculated by Laframboise theory in the zero-ion temperature limit. I_{0+} and I_{0e} can be calculated through $J = n\bar{v}/4$ by assuming a Maxwellian distribution.

$$I_{0+} = Zen_+R_p(2\pi kT_e/m_+)^{1/2} \tag{2.4}$$

$$I_{0e} = -en_eR_p(2\pi kT_e/m_e)^{1/2} \tag{2.5}$$

n_e, n_+, V_p are calculated by

$$n_e = \frac{-I_e(\chi)}{eR_p\left(2\pi kT_e/m_e\right)^{1/2} f\left(R_p/\lambda_d, \chi\right)}, \chi > 0 \tag{2.6}$$

$$n_+ = \frac{I_+(\chi)}{eR_p\left(2\pi kT_e/m_+\right)^{1/2} f\left(R_p/\lambda_d, \chi\right)}, \chi < 0 \tag{2.7}$$

$$V_p(new) = V_p(old) + \frac{kT_e}{e}\ln\left[I_{0e}(new)/I_{0e}(old)\right] \tag{2.8}$$

and kT_e is re-calculated after other parameters are corrected. The routines re-calculate those parameters until the results are self-consistent.

In the simple probe theory, the integration of $\mathrm{I(V)}$ directly for calculation of T_e neglects the possible ion current. However, the ion current is calculated and corrected in Laframboise theory. Therefore, Laframboise theory was used for all measurements. Simple probe theory was only used for a quick result and to provide an initial value to the program based on Laframboise theory.

2.2.3 An Introduction of Electron Collisions inside the Plasma

The formation of EEDF is affected by the plasma system design and process parameters. Fundamentally it is decided by the interaction of electrons with electromagnetic field and the collisions between electrons and electrons with neutrals, which also decide the electron impact reactions.

Based on the consideration of energy conservation, the collisions inside a weakly ionized plasma are elastic collisions and inelastic collisions. For an elastic collision, the colliding particles act as two hard sphere and momentum is conserved during the collision, only kinetic energy transfers between colliding particles. In an inelastic collision when electrons collide with heavy particles, the overall energy is conserved but the potential energy of the heavy particles is changed. Certain kinetic energy has been converted or gained through potential energy change. Therefore, the inelastic collisions generate ions and different neutral radicals.

In plasma, electron collisions are usually characterized by collision cross section σ and collision frequency ν, $\nu = n_g \sigma v$ where n_g is the target particles density.

If a distribution function is known, for example, a Maxwellian distribution, then it can be expressed as

$$\nu = n_g \left(\frac{m}{2\pi kT}\right)^{3/2} \int_0^\infty \sigma(v) v exp\left(-\frac{mv^2}{2kT}\right) 4\pi v^2 dv \tag{2.9}$$

In a plasma, there could be tens or hundreds of different kinds of inelastic collisions. For atom gas Ar, the electron induced inelastic collision can be generally divided into two kinds: electron impact ionization and electron impact excitation. They can be illustrated as

$$\mathrm{e} + \mathrm{Ar} \rightarrow \mathrm{Ar}^+ + 2\mathrm{e} \tag{2.10}$$

$$\mathrm{e} + \mathrm{Ar} \rightarrow \mathrm{e} + \mathrm{Ar}^* \tag{2.11}$$

In reverse, the electron lost due to recombination and de-excitation

$$\mathrm{e} + \mathrm{Ar}^+ \rightarrow \mathrm{Ar} + \mathrm{h}\nu \tag{2.12}$$

$$e + \mathrm{Ar}^* \rightarrow \mathrm{e} + \mathrm{Ar} + \mathrm{h}\nu \tag{2.13}$$

For molecular gases the inelastic collisions can be more complicated. Electron impact dissociation, direct molecular ionization, rotational and vibrational excitation all need to be considered. For example, in a hydrogen gas, additional reactions due to molecules can be illustrated as

$$\mathrm{e} + \mathrm{H}_2 \rightarrow \mathrm{H} + \mathrm{H} + \mathrm{e} \tag{2.14}$$

$$\mathrm{e} + \mathrm{H}_2 \rightarrow \mathrm{H}_2^+ + 2\mathrm{e} \tag{2.15}$$

$$\mathrm{e} + \mathrm{H}_2(\nu = 0) \rightarrow \mathrm{H}_2(\nu = 1) + 2\mathrm{e} \tag{2.16}$$

Electro-negative gases such as N_2, O_2, negative ions can be formed due to electron attachment

$$\mathrm{e} + \mathrm{N}_2 \rightarrow \mathrm{N}_2^- \tag{2.17}$$

which can be important reaction path for electron loss.

2.2.4 Electron Energy Distribution Function

The electron energy distribution function (EEDF) represents the distribution of electrons with different kinetic energies inside the plasma. It is a key concept in understanding the plasma chemistry, because electron induced dissociation and ionization sustains the plasma and generates the most reaction radicals. The EEPF was obtained through Druyvesteyn method as described in Eq. 2.1. In the software program, the EEDF is calculated numerically through $I - V$ curve and plotted as EEPF vs V. Note the units for $f_e(\varepsilon)$ are $eV^{-1}cm^{-3}$ (EEDF), for $f_p(\varepsilon)$ are $eV^{-3/2}cm^{-3}$ (EEPF). Fig 2.9 illustrates an EEPF plot for an Ar plasma at input power of 100 W and system pressure of 100 mTorr.

With known EEDF and gas collision cross section, different rate constants K for electron impact reactions can be calculated as

$$K = \int_0^\infty v\sigma(v)F(\epsilon)dE \tag{2.18}$$

The detailed descriptions of Boltzman equation and the Druyvesteyn method are included in the Appendix.

2.3 Results

2.3.1 Characterization of Capacitively Coupled Ar Plasma

Ar plasma parameters were measured with Langmuir probe in capacitively coupled mode for different input power and system pressure. Those measurements provide the parameter change with power and pressure, and also serve as calibration data for the chamber and probe condition. During this research work, Ar plasma was regularly measured and the data were compared.

Fig. 2.10 shows the $\mathrm{T_e}$ change with power at 50, 100, 150 and 200 W with four different pessures: 50, 100, 150 and 200 mTorr. Every power in this pressure range affected $\mathrm{T_e}$ similarly in trend. The $\mathrm{T_e}$ dropped fast between 50 to 100 mTor. For 100 W, it changed from 2.05 to 1.64. After 100 mTorr, the $\mathrm{T_e}$ changed slowly and $\mathrm{T_e}$ was more stable with changed pressure. From 100 to 200 mTorr at 100 W, it only dropped slightly around 0.05 eV. In this pressure range, lower power provided higher $\mathrm{T_e}$. For 100 mTorr, the $\mathrm{T_e}$ changed from 1.45 to 1.94 from 50 W to 200 W input power. These trends had also been observed by other researchers in similar configuration.[26, 10, 21]

Fig. 2.11 shows the change of electron density ($\mathrm{n_e}$, Fig. 2.11(a)) and ion density ($\mathrm{n_i}$, Fig. 2.11(b)) for those power (50-200 W) and pressure (50-200 mTorr) ranges. Both $\mathrm{n_e}$ and $\mathrm{n_i}$ displayed similar trends in these power and pressure ranges. These trends have also been mentioned in the literature.[26] For every system pressure, $\mathrm{n_e}$ increased almost linearly with input power. The changing rate increased with increased pressure. From 50 W to 200 W, for 50 mTorr, it changed from 1.8×10^{10} to 3.0×10^{10}, increased 1.7 times. For 200 mTorr, it changed from 7.0×10^{10} to 1.82×10^{11}, increased 2.6 times. Therefore, when system pressure was higher, the power effect on $\mathrm{n_e}$ was higher. Similarly, for 50 W input power, $\mathrm{n_e}$ changed from 1.6×10^{10} to 7.0×10^{10} from 50 W to 200 W. For 200 W input power, $\mathrm{n_e}$ changed from 2.6×10^{10} to 1.74×10^{11}. Therefore, when input power was higher, the system pressure effect on $\mathrm{n_e}$ was also stronger. The behavior of $\mathrm{n_i}$ with power

and pressure was similar as n_e. At four different system pressures, n_i increased with input power. At higher pressure, the effect of input power was higher. It should mention that n_e is not equal to n_i. This suggests the existence of possible negative ions, but also implied the restriction of accuracy for OML theory in calculating ion density in weakly ionized plasmas.

It is difficult to quantitatively describe the T_e, n_e, and n_i change with pressure and power. Qualitatively, in our pressure and power range, when system pressure increased, the collision frequency between electrons and neutrals increased. Therefore, the possibility for ionization increased, which resulted in the increase of n_e and n_i. Higher collision frequency between electrons with neutrals or between electrons with charged particles increased the power loss of electrons, therefore, the T_e decreased. When input power increased, more power was transferd to the plasma through electrons, which resulted in the increase of n_e and n_i. It also increased the collision frequency between electrons, which is the most effective in a weakly ionized plasma for electrons to transfer energy, therefore, the T_e decreased with increased source power.[26]

Fig. 2.12 shows the EEPF change with different pressure at 100 W input power. At 50 mTorr, the EEPF shows a likely bi-Maxwellian distribution structure at around 5-6 eV. When system pressure increased, the EEPF at low energy gradually flattened. The EEPF at 200 mTorr was more likely a Druyvesteyn distribution. This similar trend was also observed by Godyak in Ar plasma and had been reported by other researchers.[10, 13] It is a result of increased collision frequency between charged particles and between charged particles and neutrals due to increased system pressure.

2.3.2 Characterization of Inductively Coupled Ar Plasma

The GEC system could be operated under inductive mode when the system power coupling method was modified. The system pressure for this operation usually was lower compared with capacitive coupled system. Usually the plasma was turned on in capacitive mode first, with further increased power, the system could reach a critical power. After this power, the plasma lightness dramatically increased, which indicates the system has transferred from capacitive mode to inductive mode. Plasma system in inductive

mode has much higher electron and ion density compared with capacitive mode under similar system pressure and power.

Fig. 2.13 shows the electron density and ion density change with different power and pressure when system was operated under inductive mode. For Fig. 2.13(a) the curves show that two operating regions existed for the system. The $\mathrm{n_e}$ was low at 10 W for 116 mTorr, which indicate that the system was actually on capacitive mode. It increased fast untill the critical power, around 30 W. After this power, the system was on inductive mode and $\mathrm{n_e}$ increased slower. The $\mathrm{n_e}$ between capacitive mode and inductive mode was dramatically different, it was 7.5×10^9 at 20 W, but 8.6×10^{10} at 110W. This is almost two times higher compared with similar power and pressure in capacitive mode.

Fig. 2.14 shows the $\mathrm{T_e}$ change with different power and pressure. It can be observed that the $\mathrm{T_e}$ changed dramatically around the critical power for the mode transition. The $\mathrm{T_e}$ increased and dropped fast at this power. However, in a stable inductive mode, the $\mathrm{T_e}$ was more stable with further increased power.

2.4 Conclusions

Langmuir probe has been used in characterization of both capacitively coupled and inductively coupled Ar plasmas. The change of T_e, n_e, and EEDF with input power and gas pressure was tested. The general trends were verified by different literature results although no literature results in identical experimental conditions available.

2.5 Figures

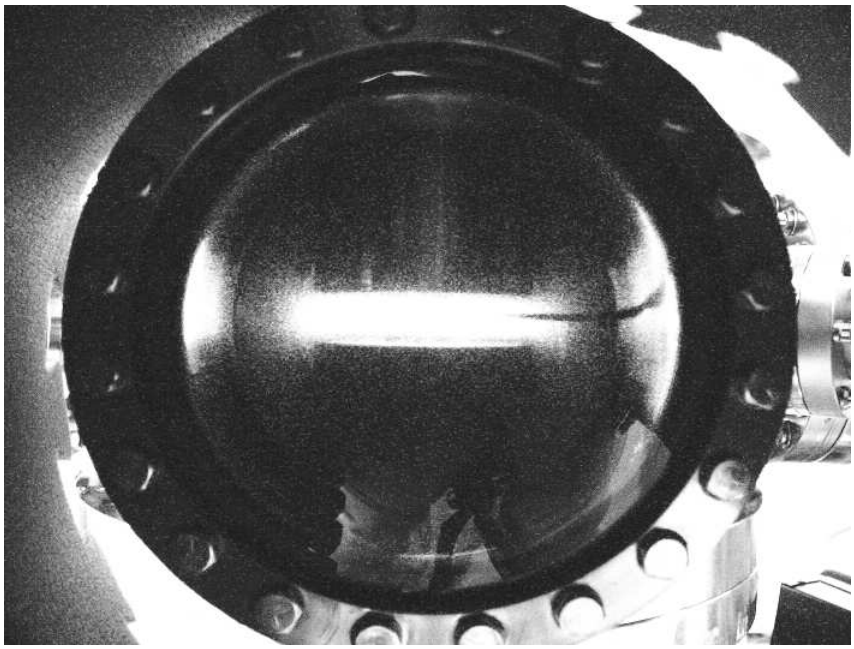

Figure 2.1: A picture of the probe system in a capacitively coupled Ar plasma.

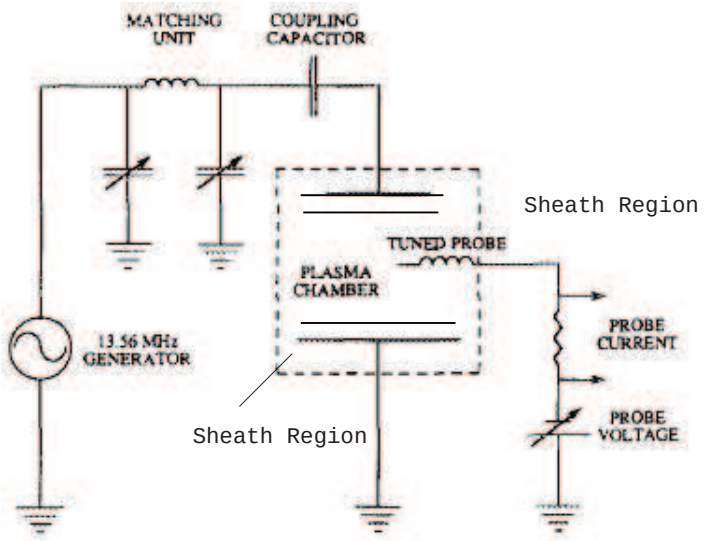

Figure 2.2: An equivalent circuit of typical probe setup in a capacitively coupled plasma, showing the power source, matching unit, plasma with sheath region, probe, and probe external circuit.

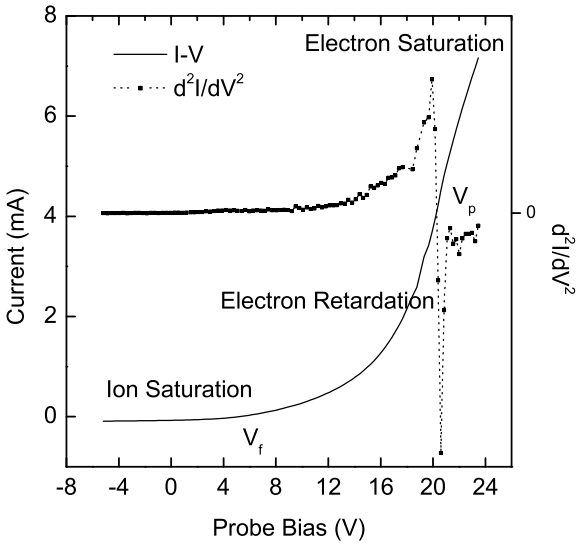

Figure 2.3: A typical I-V curve and its second order derivative from probe measurement. V_f floating potential, V_p plasma potential.

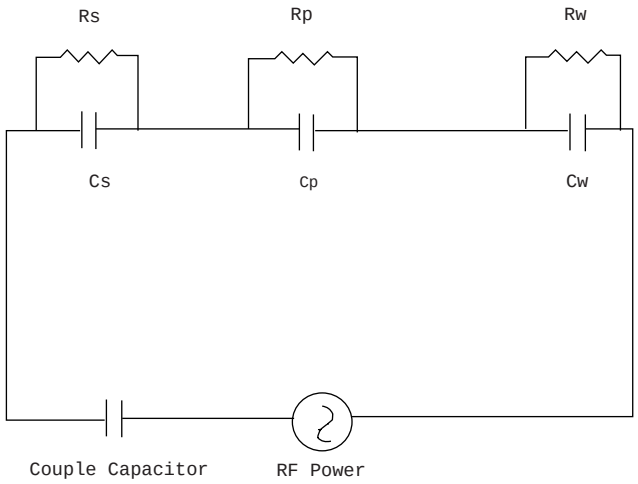

Figure 2.4: A simple equivalent circuit for a capacitively coupled plasma.

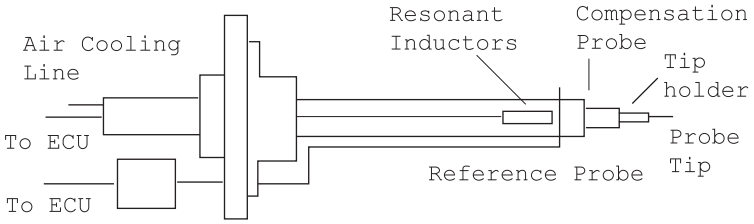

Figure 2.5: Illustration of the SmartProbe structure with probe tip, tip holder, compensation probe, reference probe, and the resonant inductors inside the holder.

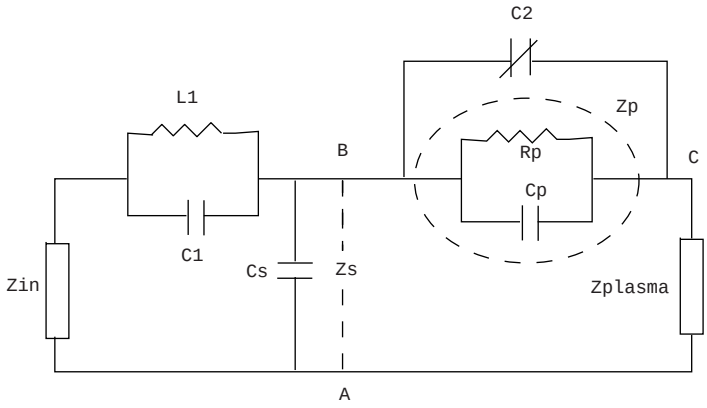

Figure 2.6: The simplified equivalent circuit of the SmartProbe inside the plasma.

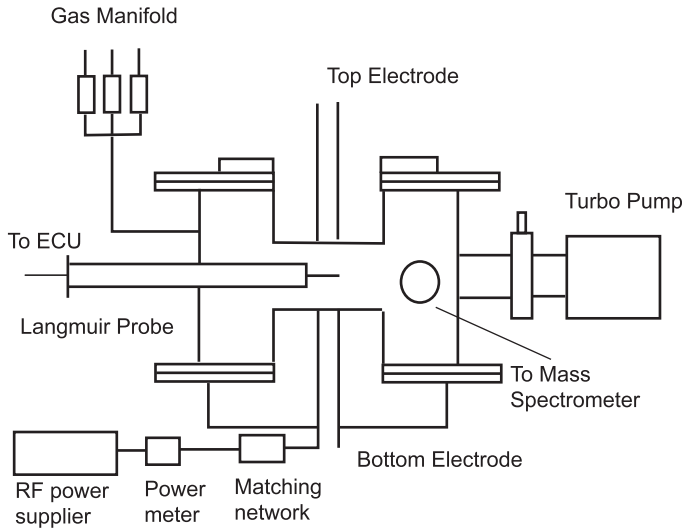

Figure 2.7: Schematic of experimental system showing the GEC chamber, Langmuir probe, RF power supplier, matching network, power meter, mass spectrometer, and gas manifold.

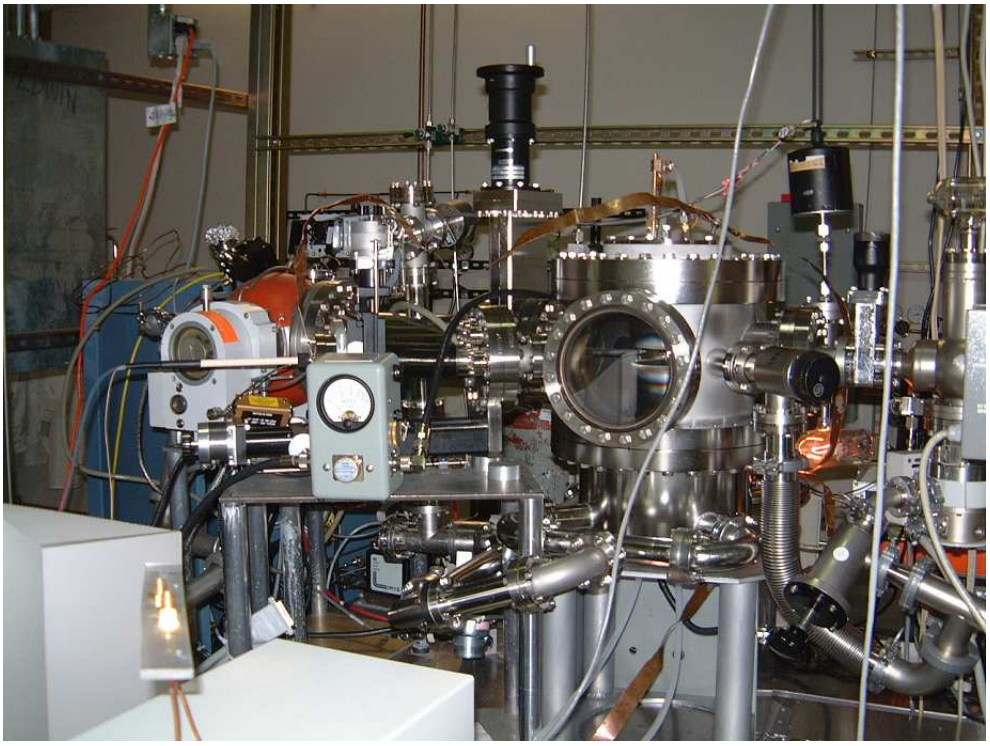

Figure 2.8: The photo of the GEC system with Langmuir probe

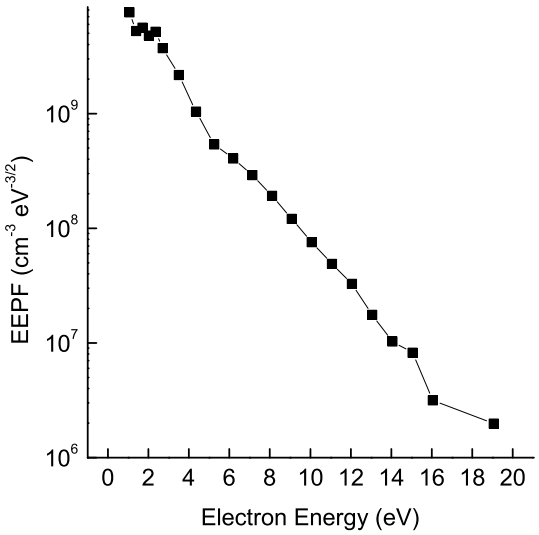

Figure 2.9: A typical EEPF plot for an Ar plasma in GEC system at power of 100 W and pressure of 100 mTorr

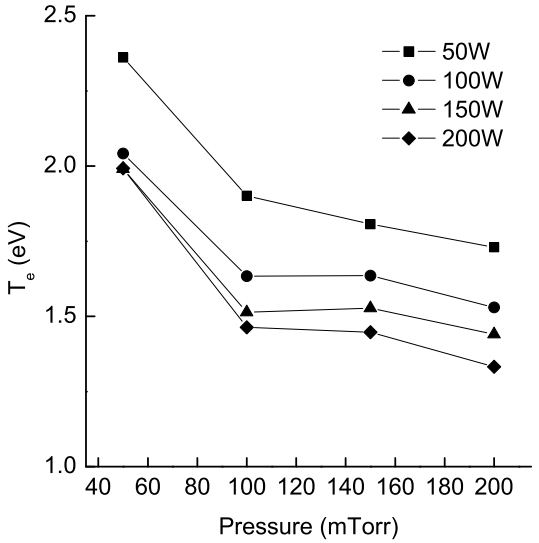

Figure 2.10: T_e change with power (50-200 W) and pressure (50-200 mTorr) in capacitively coupled Ar plasmas for GEC system.

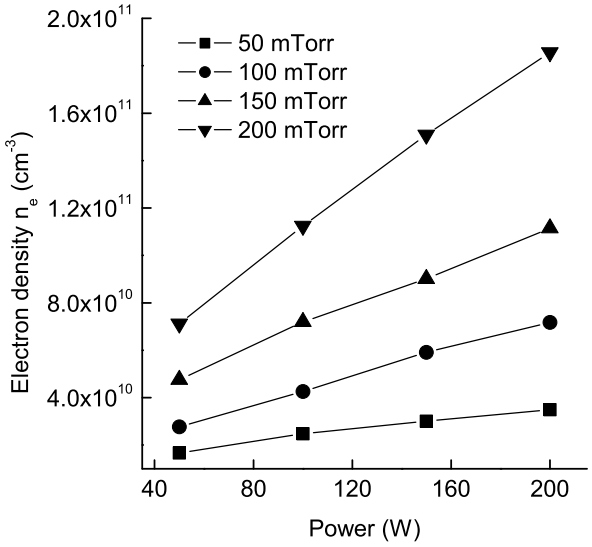

(a) n_e change with power and pressure for Ar plasma in GEC system

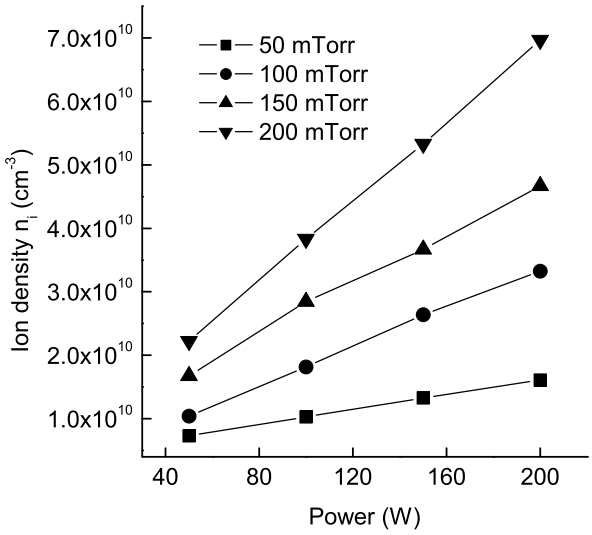

(b) n_i change with power and pressure for Ar plasma in GEC system

Figure 2.11: n_e, n_i change with power (50-200 W) and pressure (50-200 mTorr) in capacitively coupled Ar plasma in GEC system.

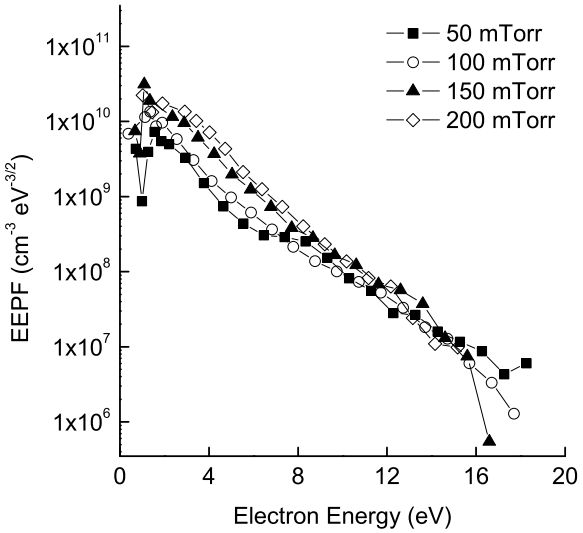

Figure 2.12: EEPF change with power (50-200 W) and pressure (50-200 mTorr) in capacitively coupled Ar plasmas in GEC system.

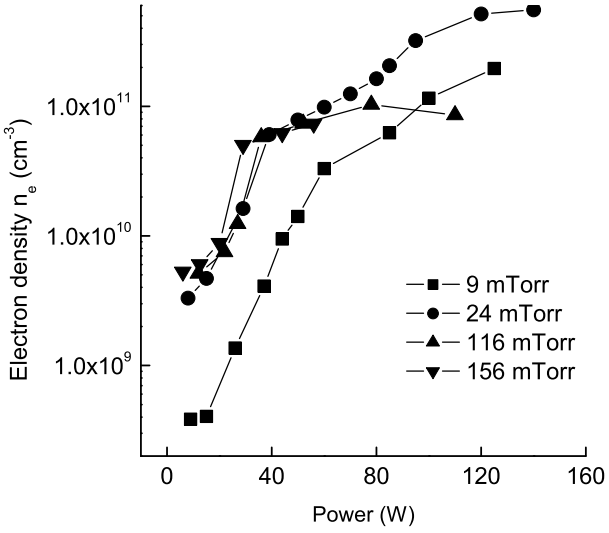

(a) n_e change with power and pressure for Ar plasma in GEC system

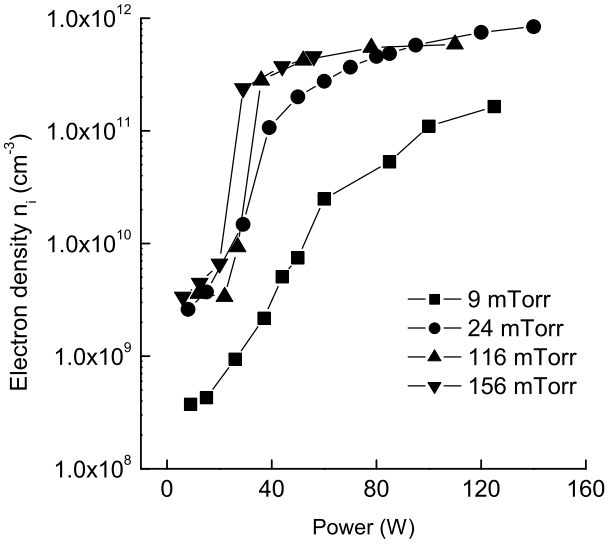

(b) n_i change with power and pressure for Ar plasma in GEC system

Figure 2.13: n_e, n_i change with power and pressure in inductively coupled Ar plasmas in GEC system

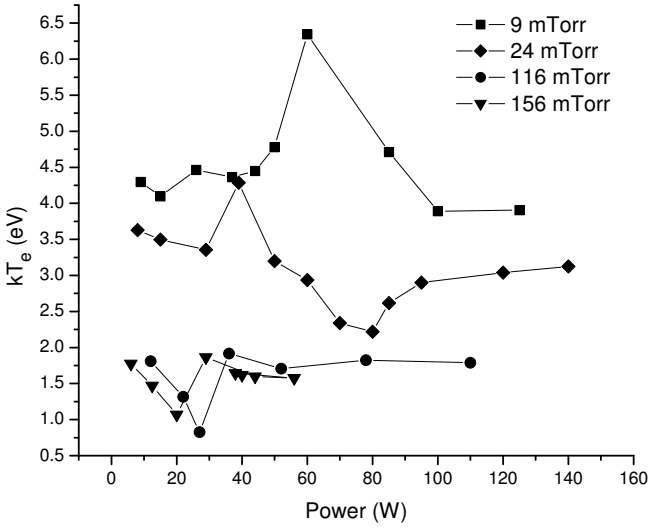

Figure 2.14: Inductively coupled Ar plasma, T_e change with power and pressure

CHAPTER 3

Manipulating Electron Physical Properties in a Capacitively Coupled Plasma by Gas Addition

3.1 Introduction

Electron impact reactions are the most important reactions for plasma chemistry because they are the major path to provide both ionic and neutral species. The electron physical properties, which are frequently characterized by the electron energy distribution function (EEDF) or the electron energy probability function (EEPF), electron temperature (T_e), and electron density (n_e), have important effect in those electron induced reactions. Understanding the elecron physical properties is very important in understanding and controling plasma chemistry.[17] After the electrons physical properties are known, together with specified gas species properties, rate constants for electron induced reactions, such as dissociation, excitation, and ionization, can be calculated for plasma modeling.[27, 28]

The electron physical properties are decided by the particular plasma system and the process parameters, which include reactor geometry, powering method, input power and frequency, system pressure, and gas species. By changing one or two parameters drastically, the electron physical properties can change strongly. A drastic change of electron physical properties usually accompanies a heating mode transition.[29] Typically three different heating mechanisms are presented in capacitively coupled plasmas: the stochastic heating, the ohmic heating, and the second electron emission heating. The detailed explanation of those heating modes is available in the literature.[29, 28] For capacitively coupled plasma, the stochastic heating and ohmic heating are especially important. Godyak *et al.* showed that the pressure changes modified the EEPF from bi-Maxwellian to Druyvesteyn, and compared different EEPF shapes between Ar and He in similar experimental conditions.[30, 10, 31] Franz showed the change of T_e in Ar, Cl_2, and BCl_3 plasmas with heating mode transition by modifying power and pressure.[26] The heating

mode transition and electron physical properties change due to the change of frequency were observed by Sugai *et al.*[32] The EEPF changes with pressure, specifically in GEC chambers, which was used in current work, are also available in literature. [25, 13]

In semiconductor industry, it is a common practice to mix different gaseous components to optimize the plasma processes.[7] The gas addition causes electron physical properties change. Bletzinger discussed the influence of attaching gases on the discharge properties.[33] Lee *et al.* modeled the T_e and n_e change with Ar and O_2 concentration in Ar-O_2 plasmas.[34] Schaffnit *et al.* showed drastical change of ionization and dissociate rate in the BCl_3-N_2-H_2-Ar system due to gas concentration changes.[35] The T_e change with gas components in Ar-H_2, and N_2-H_2 plasmas were discussed in literature.[36, 37, 38, 39] In current work, the H_2, D_2, and N_2 were added to Ar plasmas in a GEC chamber. The change of electron physical properties by gas components concentration changes are discussed in detail in this chapter. The mechanisms for the changes are suggested and further applied to Ar-CH_4-H_2 and Ar-N_2-H_2 plasmas.

3.2 Experimental Setup

Fig. 3.1 shows a schematic of the experimental arrangement and the system components. The GEC reference cell is a well-known system for plasma research, a detailed description of the cell is available in reference [18] and NIST website (www.nist.gov). The plasma was powered by a 13.56 MHz RF power supplier (ENI power system Inc. OEM-6) through bottom electrode. The system used a manual matching network to reduce the reflected power. A through-line watt meter (Bird electronics Corp.) was used for measuring the RF power. In the experiments, the reflected power was kept below 5% of input power. In the following sections, the input power refers to the net input power, in which the reflected power was subtracted from input power.

The base pressure for the cell was 2.0×10^{-7} Torr. Pressure during experiments was monitored by a Baratron absolute pressure gauge (MKS 220). Three MFCs (mass flow-rate controler) were used to control the gas flow rate seperately. The MFCs together with the throttle valve between the chamber and turbo pump adjusted the chamber pressure. A

Balzers QMG420 mass spectrometer was used for leak detection and plasma characterization.

The Langmuir probe has been extensively used for plasma characterization. Design of the probe system and the data analysis has been widely discussed.[8, 12, 9, 7, 19] A commercially available RF-compensated probe system (SmartProbe, Scientific Systems Inc.) was used in this research. A detailed discussion of this probe system design and the theorectical background of the data analysis is available.[20, 21, 13] The parameters of electron density (n_e), ion density (n_i), electron temperature or average electron kinetic energy (T_e), floating potential (V_f), plasma potential (V_p), and electron energy distribution function (EEDF) were measured through the probe. For convenience to compare with Maxwellian distribution and other experimental results in literatures, the EEPF (electron energy probability function) was used in following sections. It was obtained by Druyvesteyn method [10]

$$f(\epsilon) = \frac{2I"}{eA}\left(\frac{2m\epsilon}{e}\right)^{1/2} \tag{3.1}$$

where I" is the second order deriative of current and probe sweeping voltage, A is the probe collecting area, ϵ is the electron kinetic energy. The relationship between EEDF [$\mathrm{F}(\epsilon)$] and EEPF [$\mathrm{f}(\epsilon)$] is defined as $\mathrm{F}(\epsilon) = \epsilon^{1/2}\mathrm{f}(\epsilon)$. This probe system has been widely used in the plasma research community and has been demonstrated in GEC cells.[14, 15, 16, 17] During our experiments, the probe tip was located horizontally at the center of the electrode and vertically 1 cm from the top electrode.

Ar plasma was regularly measured to serve as the criterion of chamber and probe conditions. The plasma parameters for Ar were compared and agreed with the literature.[21, 22, 23, 24, 19, 25] The probe tip was changed regularly.

3.3 Results

3.3.1 H_2 and D_2 addition

Fig. 3.2 shows the changes of EEPF with H_2 concentration in Ar-H_2 plasmas at input power of 100 W and a system pressure of 100 mTorr. The H_2 concentration changed

from 0% to 23%. The Ar plasma displayed a weak bi-Maxwellian distribution when no H_2 was added, which can be approximated as two Maxwellian distributions with T_e of 1.3 and 5.2 eV that intersected at 5.2 eV. The EEPF shape cannot be described by simple combination of Maxwellian distribution after H_2 was added to the system. A transition region began to form. This transition region extended into higher energy with increased H_2 concentration. For 2% H_2, the transition region was mainly in 4 to 8 eV. For 7% H_2, the region was approximatedly from 4 to 12 eV. For 23% H_2, the EEPF shows as a curve after 4 eV, deviated strongly from Maxwellian distribution or their combinations. The formation of this transition region caused electrons population changed in different energy range. With increased H_2 concentration, electrons population increased at higher energy range. For example, the EEPF at 11 eV was 7.7×10^7 for 23% H_2 and 4.9×10^7 for 0% H_2, increased 60%. But the EEPF at 3.5 eV was 2.5×10^8 for 23% H_2 and 2.2×10^9 for 0% H_2, was one order lower.

Fig. 3.3 shows the changes of T_e (top) and n_e (bottom) with increased H_2 concentration for input powers of 50, 100, and 150 W and system pressures of 50 and 100 mTorr. For same pressure, a higher input power led to higher n_e and lower T_e. At same input power, a higher pressure led to higher n_e but lower T_e. These trends are in agreement with the T_e and n_e change for Ar plasma in the same measurement range. [40] For the measured input powers and system pressures, the T_e increased with increased H_2 concentration in a similar trend. At 50 W and 50 mTorr, T_e changed from 2.8 to 5.4 eV, increased 90% for H_2 concentration changes from 0% to 23%. At 150 W and 100 mTorr, for the same H_2 concentration, T_e changed about 120%, from 1.7 to 3.8 eV.

In the measured pressure and power range, the n_e decreased with increased H_2 concentration. At 50 W, 50 mTorr, from 0% to 23% H_2, n_e decreased from 1×10^{10} to 4.5×10^9, for 100 mTorr and 100 W in the same H_2 concentration range, the n_e decreased from 2.3×10^{10} to 7.9×10^9, both more than 50%. The n_e decreased slower at 50 mTorr compared with 100 mTorr. At 100 mTorr, the drop of n_e mainly happened within initial 9% H_2 addition.

Fig. 3.4 shows the changes of EEPF with D_2 concentration in Ar-D_2 plasmas with an input power of 100 W and a system pressure of 100 mTorr. The changes in EEPF

with D_2 concentration were very similar to the Ar-H_2 plasma. Once 2% D_2 was added to the system, a transition region formed, and this transition region extended into higher energy with increased D_2 concentration. This generally causes an increase in electron population at higher energy range and a drop at lower energy. Fig. 3.5 shows the changes of T_e (top) and n_e (bottom) with D_2 concentration in Ar-D_2 plasmas with input powers of 100 and 150 W and a system pressure of 100 mTorr. For comparison, T_e and n_e changes with H_2 concentration for 100 W and 100 mTorr in Ar-H_2 plasmas were plotted in the same figures. The general trends for T_e and n_e change with D_2 concentration are very similar to the Ar-H_2 plasma: the T_e increased but the n_e decreased when D_2 concentration increased. The changes of T_e at 100 W input power and 100 mTorr system pressure for Ar-H_2 and Ar-D_2 were very close to each other. The n_e for the Ar-H_2 system, however, was lower compared with the Ar-D_2 plasma at 100 W and 100 mTorr.

3.3.2 N_2 addition

Fig. 3.6 shows the changes of EEPF with N_2 concentration in Ar-N_2 plasmas with an input power of 100 W and a system pressure of 100 mTorr. When 6% N_2 was added to the system, the EEPF displayed a strong bi-Maxwellian distribution. It can be approximated as two Maxwellian distributions with T_e of 1.7 and 2.3 eV that intersected at 4 eV. The EEPF basically remained the same shape with further increasing N_2 concentration.

Fig. 3.7 shows the changes of T_e (top) and n_e (bottom) with N_2 concentration in Ar-N_2 plasmas with input power of 50, 100, and 150 W and system pressures of 50 and 100 mTorr. The N_2 concentration changed from 0% to 28%. The T_e displayed similar trends in the measured pressure and power range. It dropped quickly when N_2 concentration increased from 0% to 3% and then remained relatively stable as the N_2 concentration further increased. For example, at 100 W and 100 mTorr, the T_e decreased from 1.7 to 0.8 when the N_2 concentration changed from 0% to 4%, a drop of more than 50%. When the N_2 concentration changed from 4% to 28%, the T_e only changed from 0.8 to 0.7, around 10%. The T_e for the three input powers were close to each other at each pressure. The trend of n_e change with N_2 concentration was different at 50 and 100 mTorr. At 50 mTorr, the n_e was relatively stable with N_2 concentration. For example, at an input power of 100

W, the n_e changed from 7.7×10^9 to 6.5×10^9, a change of around 15%. At 100 mTorr, changes of n_e with N_2 concentration were stronger at 100 and 150 W input powers. But the change of n_e occurs mainly with the initial 3% N_2 addition. It remained stable with further increased N_2 concentration.

3.4 Discussion

At input power of 100 W and pressure of 100 mTorr, the Ar plasma showed a weak bi-Maxwellian distribution as T_e of 1.3 and 5.2 eV. It had an apparent T_e as 1.8 eV and n_e as 2.3×10^{10} cm^{-3}, which were used in calculations presented below. The Bohr velocity, $\mathrm{u_B} = (\mathrm{qT_e/m_i})^{1/2}$, where q is the electron charge and m_i is the Ar ion mass, was 2×10^3 m/s. The Deybe length, $\lambda_\mathrm{D} = (\epsilon_0 \mathrm{T_e/qn_0})^{1/2}$, was 0.07 mm, where ϵ_0 is vacuum permitivity and n_0 was approximated by n_e. Then ion plasma frequency $\omega_\mathrm{i} = (\mathrm{q^2 n_0/m_i \epsilon_0})^{1/2} = \mathrm{u_B}/\lambda_\mathrm{D}$ was 3.1×10^7 s^{-1}, the electron plasma frequency $\omega_\mathrm{e} = (\mathrm{q^2 n_0/m_e \epsilon_0})^{1/2} = (\mathrm{m_i/m_e})^{1/2}\,\omega_\mathrm{i}$ was 8.3×10^9 s^{-1}. The frequency comparison shows $(\omega_\mathrm{i}/\omega)^2 = 0.13 \ll 1$ and $(\omega_\mathrm{e}/\omega)^{1/2} = 1 \times 10^4 \gg 1$, where $\omega = 2\pi f = 8.52 \times 10^7$ s^{-1}. The parameter $(\mathrm{T_i/T_e})\,\mathrm{d}$ was 0.28 mm, where T_i is ion temperature and approximated around room temperature, d is the bulk plasma length, was around 1.94 cm through naked eye observation during experiment. The ion mean free path, $\lambda_\mathrm{i} = 1/\mathrm{n_g}\sigma_\mathrm{i}$, was 0.3 mm, where n_g is gas density and σ_i is ion-atom scattering cross section, and $(\mathrm{T_i/T_e})\,\mathrm{d} \leq \lambda_\mathrm{i}$

With the above conditions, the ohmic heating can be calculated as:

$$\bar{S}_{ohm} = 1.73 \frac{m_e}{2e} \frac{n_s}{n_0} \epsilon_0 \omega^2 \nu_m T_e^{1/2} V_1^{1/2} d \tag{3.2}$$

where stochastic heating is estimated by

$$\bar{S}_{stoc} \approx 0.45 \frac{m_e}{e}^{1/2} \epsilon_0 \omega^2 T_e^{1/2} V_1 \tag{3.3}$$

where V_1 is sheath voltage, $\mathrm{n_s/n_0} = 0.86\,(3 + \mathrm{l}/2\lambda_\mathrm{i})^{-1/2}$ is 0.13, ν_m is electron-neutral collision frequency and was approximated as 3×10^{-8} s^{-1}. The calculation then showed that $\bar{\mathrm{S}}_\mathrm{ohm} = 0.35 \mathrm{V}_1^{1/2}$ and $\bar{\mathrm{S}}_\mathrm{stoc} = 0.09 \mathrm{V}_1$, which gives a ratio as $\bar{S}_{stoc}/\bar{S}_{ohm} = 0.26 V_1^{1/2}$.

The above equations are used for symmetrical plane parallel geometry. Because GEC is an asymmetric chamber, the powering electrode area is far smaller than grounded electrode, the electron absorbed power through stochastic heating should be mainly through the powering electrode and the V_1 could be high. Literature shows for input powers of 10-60 W and pressure of 67 Pa, the Ar plasma in a GEC chamber had DC bias 100-400 V, which can be approximated for V_1.[25] More details regarding calculations above can be found in reference.[28]

3.4.1 Ar-H_2 plasma

The changes of EEPF, T_e and n_e by changing H_2 concentration were self-consistent: EEPF dropped at lower energy but increased at higher energy, as illustrated in Fig. 3.8. An increased T_e was expected. The power absorption is calculated by

$$S_{abs} = 2en_s u_s(\bar{V} + \epsilon_c + 2T_e) \tag{3.4}$$

where n_s is electron density at sheath edge, u_s is ion velocity at sheath edge, $\bar{V}$ is sheath voltage, ϵ_c is collision loss energy. With an increased T_e and constant input power, it was reasonable to expect the decrease of n_s, which was directly connected with n_e.

The modification of electron physical properties in plasmas by gas mixture is recoganized as "transparency effect",[41] which originates from the difference in collision cross section and threshold energy between different gas components. Quantitative explanation of this phenomenon needs detailed consideration of all electron impact reactions and the interaction between different gas components. Qualitatively, Ar has a very small σ_{tot} (total cross section) at low energy, it increases fast with increased electron energy. This was used by Godyak in explaining the two temperature EEPF structure in a capacitively coupled Ar plasma.[30] For H_2, the σ_{tot} is several times higher compared with Ar initially, but after 2-3 eV it drops with increased electron energy. After 6 eV, σ_{tot} for H_2 is lower compared with Ar. This difference has significant affect in electron physical properties. As an example, although ionization threshold energy for Ar and H_2 are close (15.7 and 15.4 eV), the difference in collision cross section implies that the ionization ratio for H_2

would be much lower compared with Ar at same pressure and input power, which partly explains the n_e drops with increased H_2 concentration in Ar-H_2 plasmas.

A more quantitative method can be obtained through comparison of the heating mechanisms. From Eqs. 3.2 and 3.3

$$\frac{\bar{S}_{ohm}}{\bar{S}_{stoc}} = 1.92 \left(\frac{m_e}{e}\right)^{1/2} \frac{n_s}{n_0} \nu_m V_1^{-1/2} d \tag{3.5}$$

One important parameter that is modified by gas addition is ν_m, the electron-neutral frequency, which can be expressed as

$$\nu_m = n_g K = n_g \int_0^\infty v\sigma(v) F(\epsilon) dE \tag{3.6}$$

where K is the rate constant. For Ar-H_2, as a simplified esimation, assum that the K is the sum of this rates for Ar and H_2 based on volume ratio, and use σ_{tot} to estimate them. The result was normalized with n_e and is illustrated in Fig.3.8. The K, and further ν_m was strongly modified by H_2 concentration. The increase of ν_m with H_2 addition increased the ratio of ohmic heating. The ohmic heating is due to the electric field acceleration in the bulk plasma and the collision between electrons and background gas, which results in higher T_e and lower n_e, which was confirmed through the experiment measurement.

The changes of electron physical properties by adding D_2 to Ar plasmas are very similar to the results obtained to H_2. D_2 has very close cross sections and threshold energies with H_2, but molecular mass for D_2 is two times higher. The similar experimental result between Ar-H_2 and Ar-D_2 plasmas further comfirmes that cross sections, rather than molecular mass, is the dominating factors for electron physical properties changes that happen in the plasma.

The concept of adding H_2 to modify electron physical properties in plasmas was applied to an Ar-CH_4 mixture. The results show that even in presence of CH_4, H_2 addition could still effectively change the electron physical properties. Fig. 3.10 shows the changes of EEPF with H_2 concentration in an Ar-CH_4(2%)-H_2 plasma with an input power of 100 W and a system pressure of 100 mTorr. Adding 2% CH_4 distorted the bi-Maxwellian distribution. With H_2 addition, the changes of EEPF for the Ar-CH_4(2%)-H_2 plasmas were similar to the Ar-H_2 plasma as described before. Fig. 3.11 shows the changes of T_e (top)

and n_e (bottom) with H_2 concentration in Ar-CH_4-H_2 plasmas with input powers of 50, 100, and 150 W and a system pressure of 50 mTorr. The system has similar trends as Ar-H_2 plasmas: T_e increases but n_e decreases with increased H_2 concentration, but the changes were smaller compared with Ar-H_2 plasmas in the same H_2 concentration. For example, At 100 W and system pressure of 50 mTorr, the T_e increases from 3.4 eV at 0% H_2 to 4.3 eV at 23% H_2, an increase of near 30%. The n_e in this H_2 concentration range decreases from 9×10^9 at 0% H_2 to 6×10^9 at 23% H_2, a drop of around 30%.

3.4.2 Ar-N_2 plasma

The N_2 addition to Ar plasma showed two significantly different features compared with Ar-H_2 plasmas. First, in Ar-N_2 plasmas the electron physical properties were very sensitive to initial concentration change (<6%), but remained more stable with further N_2 concentration increase. Second, the EEPF showed a strong bi-Maxwellian distribution with 6% N_2, this was accompanied by increased n_e and T_e.

The sensitivity of GEC system to N_2 was demonstrated by Sobolewski in another GEC chamber.[42] The experiment shows N_2 addition caused strong increase of resistivity. When N_2 increased from 0.1% to 10%, the resistivity increased from 570 Ω to 740 Ω. Similar results were observed for O_2 and H_2O addition. This phenomenon was predicted by Paranjpe *et al.*[43] They defined that electronegative plasma had the following property

$$k_i - k_a = \frac{D_a}{N\Lambda^2} \tag{3.7}$$

where k_i and k_a are the rate constants for ionization and atachment respectively, Λ is the effective length scale for diffusion, D_a is the ambipolar diffusion coefficient for electrons. Due to the electron attachment and bipolar diffusion, D_a are low for electronegative plasma. Since electron mobility is much higher than negative ions, the plasmas are expected to be sensitive to the presence of an electronegative gas. Therefore, 6% N_2 showed much stronger effect compared with H_2 since N_2 is electronegative gas but Ar and H_2 are electropositive gases. Accordingly, with reduced bipolar diffusion, a more uniform bulk plasma was expected, T_e for the plasma was expected to be less sensitive to input power, which was observed in our experiments.

For an electronegative plasma, since electrons are lost through both diffusion and attachment, the E/n field intensity was expected to increase.[29] Beltzinger *et al.* showed that in a similar Ar plasma,[33] when SF_6 changed from 0% to 23%, the field intensity for sheath region changed from 52 V/cm to 303 V/cm. The similar behavior was expected for our system. According to Eq. 3.5, the increase of V_1 will increase the ratio of stochastic heating for power absorption. This was demonstrated by the obtained EEPF shape; a strong bi-Maxwellian distribution in capacitively coupled plasma at low pressure is the signature of stochastic heating dominating. Therefore, by adding N_2 into Ar plasma at input power of 100 W and system pressure of 100 mTorr, the system changed to be strongly dominated by stochastic heating. In stochastic heating, electrons gain energy by the interaction with sheath oscillation. Electrons that bounce back by sheath expansion will have higher energy and have higher possibility to ionize the background gas. They lost energy and at the same time generate cold electrons through ionization, which forms a two-electron temperature structure. This is consistent with the EEPF measurement. With the same input power, because stochastic heating is more effective in creating electrons, measurements show that the apparent T_e drops with increased n_e. Turner *et al.* suggested for N_2 plasma that electrons could gain energy through both sheath contraction and expansion.[44] This could further enhance the generation of n_e.

This mechanism was further demonstrated in an Ar-N_2-H_2 plasma. Fig. 3.12 shows EEPF changes in Ar-N_2(3%)-H_2 plasmas with an input power of 100 W and a system pressure of 100 mTorr. With increased H_2 concentration, the EEPF remained similar shape as Ar-N_2 plasma. Fig. 3.13 shows the changes of T_e (top) and n_e (bottom) with H_2 concentration in Ar-N_2(3%)-H_2 plasmas with input powers of 50, 100, and 150 W, and system pressures of 50 and 100 mTorr. The N_2 concentration was 3% and the H_2 concentration changed from 0% to 22%. The result shows the general trends of T_e and n_e change with H_2 concentration are similar to Ar-N_2 plasmas rather than Ar-H_2 plasmas. Therefore, for Ar-N_2(3%)-H_2, N_2 addition is dominant iin the system.

3.5 Conclusion

The method of manipulating electron physical properties in plasma by gas addition was explored and demonstrated in a capacitively coupled Ar plasma system. By adding H_2 and N_2 into plasmas, T_e, n_e, and EEPF were modified effectively. The mechansims for H_2 and N_2 addition in changing the system are different. For H_2 addition, the properties modification was due to cross section and threshold energy difference between Ar and H_2, which further increased the ohmic heating in the plasma. The T_e increased more than 100% and n_e decreased more than 50% for 23% H_2 addition. The use of D_2 led to similar results. For N_2 addition, the electron properties were strongly modified even with low N_2 concentrations. The plasma showed a strong bi-Maxwellian distribution. Opposite to Ar-H_2 plasmas, the n_e increased 40% and T_e decreased more than 100% for 28% N_2 addition. The electronegativity of N_2 was considered the major reason. The H_2 and N_2 addition were applied to Ar-CH_4-H_2 and Ar-N_2-H_2 plasmas. The result showed H_2 effectively modified Ar-CH_4 plasmas with increased T_e and decreased n_e. In Ar-N_2-H_2 plasmas, the electron physical properties are dominated by the presence of N_2 at low levels(3%).

3.6 Future work

To complement the results presented here, we suggest the following work:

- Electrical measurement of the plasma properties changes with gas addition will be very useful to verify the conclusions reached here;
- The OES measurement of excitation state for H_2 and N_2 will indirectly explain the results, since the change of electron energy distribution will modify the concentration of excitation atoms or molecules;
- By solving Boltzman equation directly with gas concentration change, the theoretical work and experimental work can be compared.

The work proposed will require RF voltage and current probe, optical setup, and numerical programs.

3.7 Figures

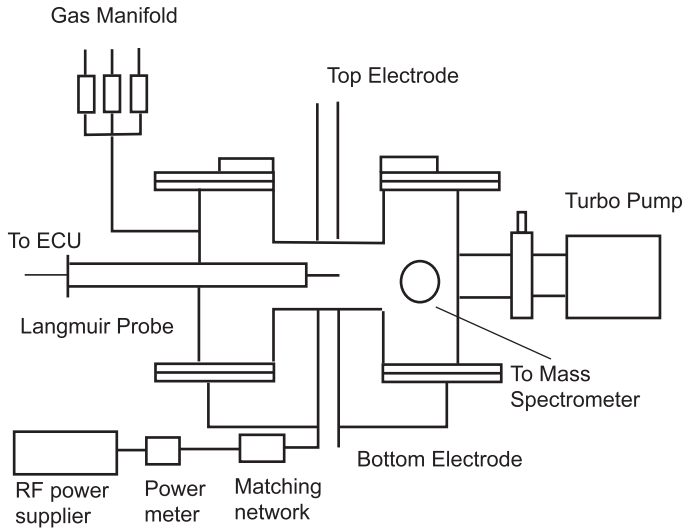

Figure 3.1: Schematic of experimental system showing the GEC chamber, Langmuir probe, RF power supplier, matching network, power meter, mass sepctrometer, and gas manifold.

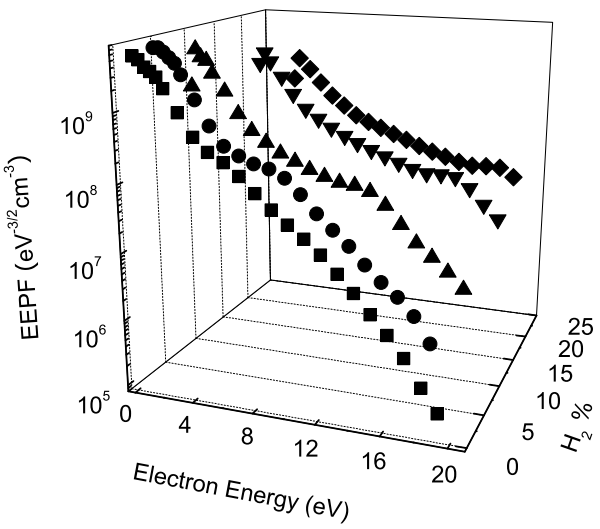

Figure 3.2: EEPF changes with H_2 concentration in Ar-H_2 plasmas at input power of 100 W and system pressure of 100 mTorr. H_2 concentrations were 0%, 2%, 7%, 17%, and 23%.

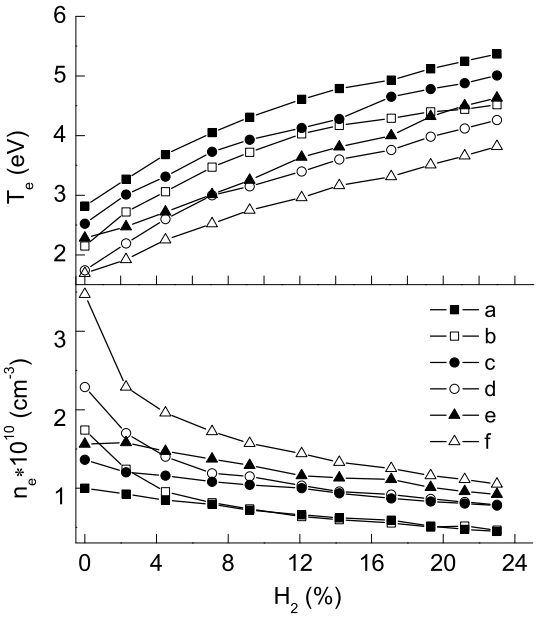

Figure 3.3: T_e (top) and n_e (bottom) changes with H_2 concentration in Ar-H_2 plasmas at input power of 50, 100, and 150 W, system pressures of 50 and 100 mTorr. a. 50 W 50 mTorr; b. 50 W 100 mTorr; c. 100 W 50 mTorr; d. 100 W 100 mTorr; e. 150 W 50 mTorr; f. 150 W 100 mTorr.

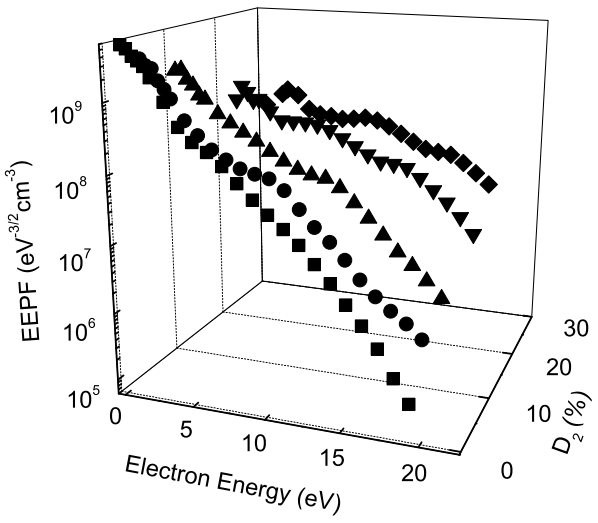

Figure 3.4: EEPF changes with D_2 concentration in Ar-D_2 plasmas at input power of 100 W and system pressure of 100 mTorr. D_2 concentrations were 0%, 3%, 9%, 20%, 28%.

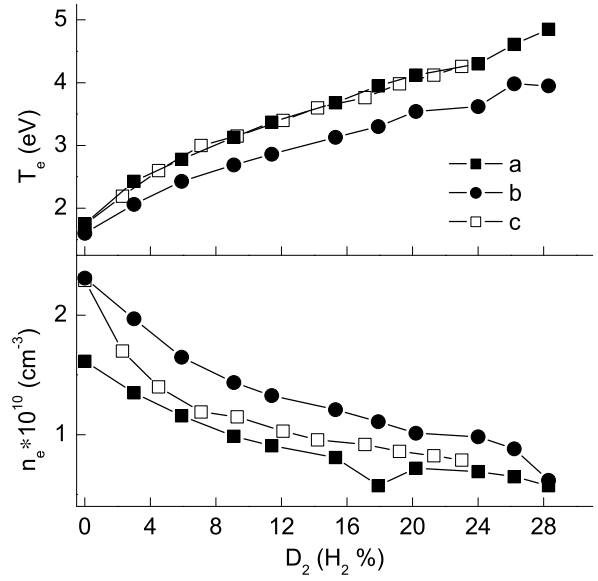

Figure 3.5: T_e (top) and n_e (bottom) changes with D_2 concentration in Ar-D_2 plasmas at input powers of 100, 150 W and system pressures of 100 mTorr, comparison with the Ar-H_2 plasmas at power of 100 W and pressure of 100 mTorr. a. 100 W, 100 mTorr; b. 150 W, 100 mTorr; c. 100 W 100 mTorr, for Ar-H_2 plasma.

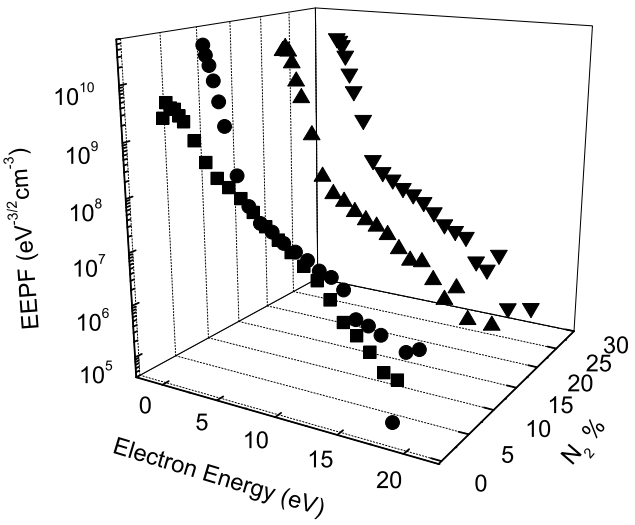

Figure 3.6: EEPF changes with N_2 concentration in Ar-N_2 plasmas at input power of 100 W and system pressure of 100 mTorr. N_2 concentrations were 0%, 6%, 18%, 28%.

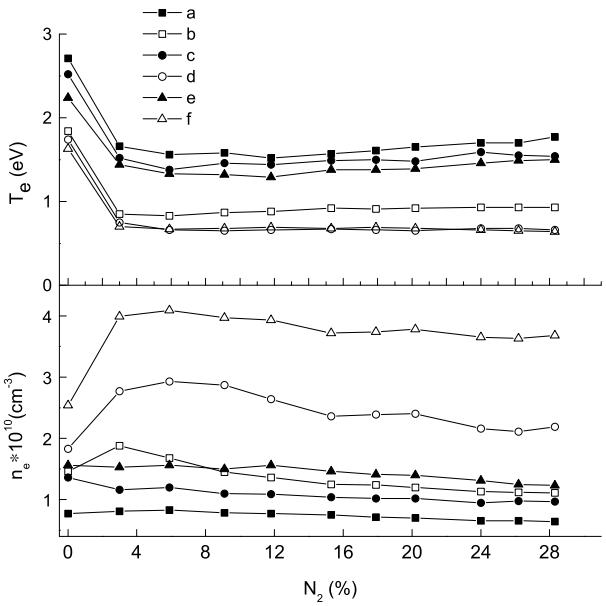

Figure 3.7: T_e (top) and n_e (bottom) changes with N_2 concentration in Ar-N_2 plasmas at input powers of 50, 100, 150 W and system pressures of 50, 100 mTorr. a. 50 W 50 mTorr; b. 50 W 100 mTorr; c. 100 W 50 mTorr; d. 100 W 100 mTorr; e. 150 W 50 mTorr; f. 150 W 100 mTorr.

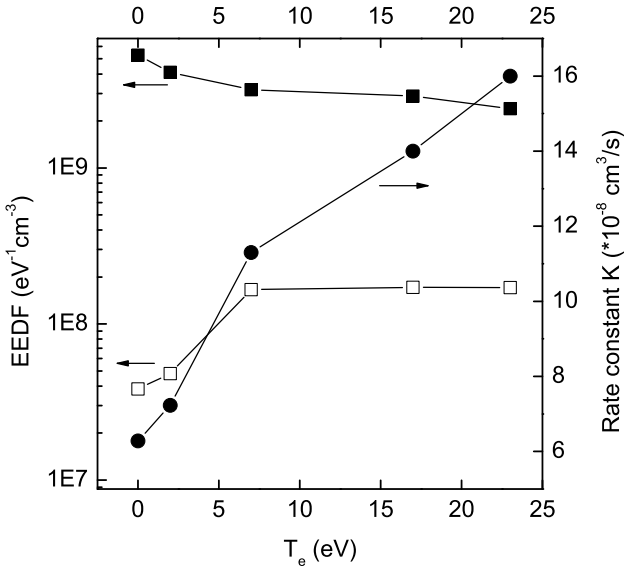

Figure 3.8: Comparison of EEDF value for electron energy at 3 eV and 14 eV, and the comparison of rate constant for integration between 3 to 15 eV based on Eq. 3.6 with H_2 concentration change in Ar-H_2 plasmas

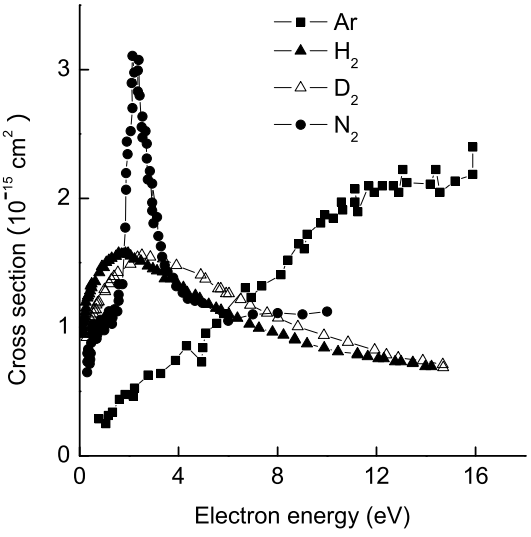

Figure 3.9: Total electron collision cross section change with electron energy for Ar, H_2, D_2, and N_2.

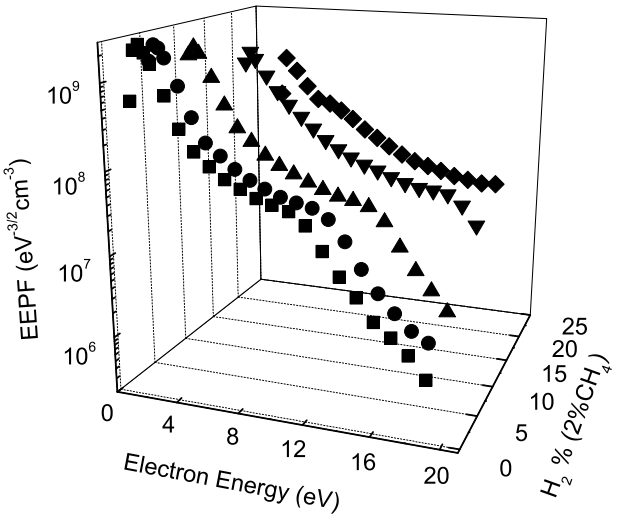

Figure 3.10: EEPF changes with H_2 concentration in Ar-CH_4-H_2 plasmas at input power of 100 W and system pressure of 100 mTorr, with 2% CH_4. H_2 concentrations were 0%, 2%, 7%, 16%, and 23%.

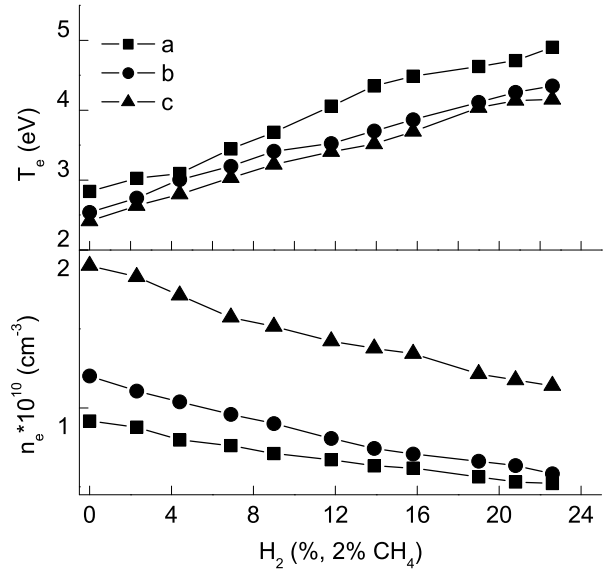

Figure 3.11: T_e (top) and n_e (bottom) changes with H_2 concentration in Ar-CH_4-H_2 plasmas at input powers of 50, 100, 150 W and system pressure of 50 mTorr, with 2% CH_4. a. 50 W 50 mTorr; b. 100 W 50 mTorr; c. 150 W 50 mTorr.

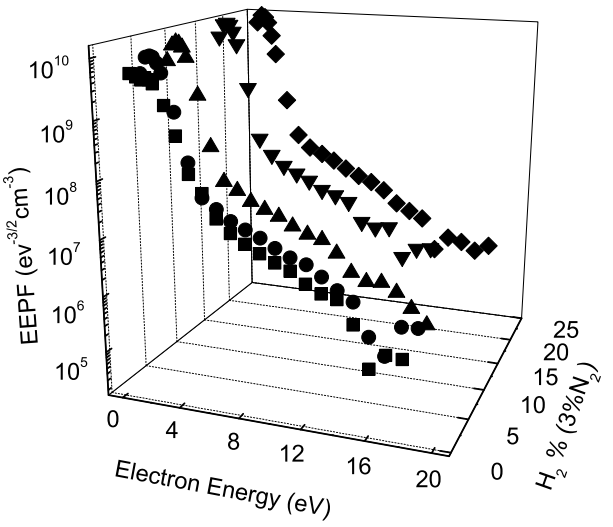

Figure 3.12: EEPF changes with H_2 concentration in Ar-N_2-H_2 plasmas at input power of 100 W and system pressure of 100 mTorr with 3% N_2. H_2 concentrations were 0%, 2%, 7%, 16%, and 22%.

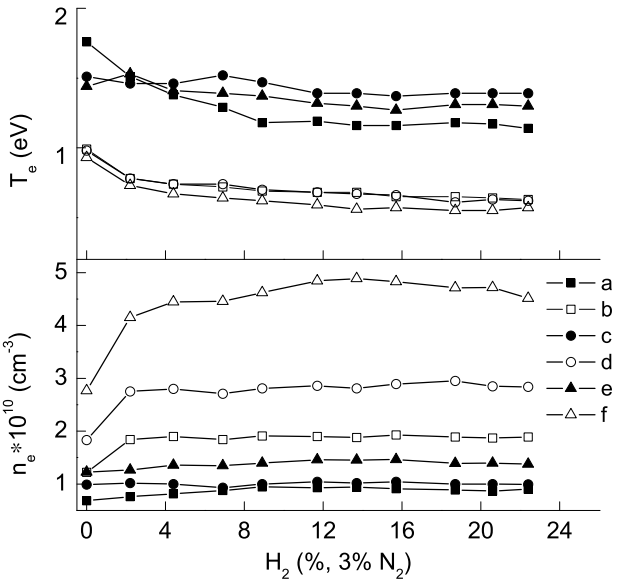

Figure 3.13: T_e (top) and n_e (bottom) changes with H_2 concentration in Ar-N_2-H_2 plasmas at input powers of 50, 100, 150 W and system pressures of 50, 100 mTorr, with 3% N_2. a. 50 W 50 mTorr; b. 50 W 100 mTorr; c. 100 W 50 mTorr; d. 100 W 100 mTorr; e. 150 W 50 mTorr; f. 150 W 100 mTorr.

CHAPTER 4

Ion and Atom Beam System and Characterization

4.1 Introduction to Plasma Etching and Beam Etching

Based on different etching mechanisms, plasma etching can fit into three general categories as illustrated by Fig. 4.1 [7]

- Sputtering. The etching is a pure physical process. Incident ions exchange momentum with target atoms through collision processes. The collision processes may cause the target atoms to leave the surface. The sputtering process is widely used for surface cleaning and thin film deposition. The theory of sputtering yield calculation is discussed in detail in this work.

- Chemical etching. The etching is mainly by chemical reactions. The radicals that are generated by plasma arrive to the target through diffusion or convection. They are then adsorbed on the target and react with target atoms. The formed product desorbes from the target and is pumped out from the system, thus the products must be volatile for the reaction to proceed. Ions may not be presented in the process, or they can be present with very low energy so the physical interaction between ions and solid surface can be neglected. A typical example of chemical etching is photoresist ashing.

- Ion enhanced etching. In this mechanism, both incident ions and reactive ions are important for the reaction. Chemical reaction and physical interaction between plasma and target both need to be considered. Ion enhanced etching is applied when an anisotropical structure is required for the etching process. The anisotropical etching that can be obtained by plasma etching is an important advantage for plasma etching over wet etching. This etching can further be divided into two kinds of reactions based on the role of the ions. (a) Energy-driven etching. The incident

ions enhance the reactions through their effect on adsorption, desorption, or the reaction itself. A typical process is the etching of Si by Cl_2 plasma. (b) Inhibitor-driven etching. The reactions form a polymer layer which covers the surface and stop further reaction. The incident ions are needed to sputter the polymer layer and keep the reaction to proceed. A typical example is the etching of SiO_2 by C_2F_6 plasma.

More detailed description about the different plasma etching mechanism are widely available in literature.[28, 45, 46]

The ion beam usually is composed of discharge tube, an extraction grid, and an acceleration grid. Exerting different voltages on extraction and acceleration screens, the ions that are generated by plasma can be extracted and then accelerated to the desired energy. Molecular beam usually refers to a directed gas flow under vacuum. The operation of atom beam is based on plasma dissociation or thermal cracking. The dissociated atoms or generated radicals can be carried to the target through directed gas flow under vacuum. Ion beam and atom beam (or molecular beam) have various application in semiconductor industry. For example, in PVD (physical vapor deposition), MBE (molecular beam epitaxy), or surface cleaning.[47] When beam technologies are used for etching process, they are named by the different combinations of the chemistry.[48]

- IBE, inert gas is used for generating ion beam.
- RIBE, reactive gas is used for generating ion beam, reactive radicals and atoms are presentes together with ions.
- CAIBE, inert gas is used for generating ion beam, reactive gas is directed to the target.
- RBIBE, inert gas is used for generating ion beam, reactive gas is used to generate an atom beam with reactive radicals and atoms.

The plasma etching is based on gas-solid reactions. A typical gas-solid reaction includes several steps:[49] gas reactants diffusion to the solid surface; adsorption and dis-

sociation of reactants on the surface; reactions between adsorbents and solid atoms; desorption of the products; products diffusion to the bulk gas. The plasma etching provides a more difficult situation compared with traditional gas-solid reactions. First, the reactions in the gas phase of a plasma are very complicated: several hundreds reactions may occur inside the plasma. Second, interactions on the gas-solid interface are complicated due to the presence of energetic ions. Those energetic ions can sputter the target surface, generate defects to enhance the adsorption or adsorption dissociation, sputter the adsorbed products or reaction residue, and pass energy to the reactions directly. These interactions drastically complicate the analysis of surface reactions. Finally, plasma parameters are highly inter-related and it is very difficult to obtain independent control through the change of process parameters. For example, an increase in the input power may increase the reactive radicals concentration, but it may change the ion flux and incident ion energy at the same time. A decrease in the gas pressure may decrease the reactive radicals concentration, but also reduce the ion flux and increase the ion energy.

In the effort to understand plasma etching mechanisms, it is desirable to decouple the ions from the radicals to simplify the complicated situation. With seperate control of ion flux, ion energy, and radical concentration, it is easier to recognize the rate limiting step and to obtain fundamental data. Beam technologies provide this ability to seperatly control the energetic ions and the reactive radicals, which makes them a useful tool to identify the effect of ions on the reaction, as well as to identify the rate limiting step, geometry effects, and surface morphology. For example, the combination of Ar ion beam, Cl_2, and XeF_2 gas has been used to identify the limiting step for etching of Si and SiO_2.[50, 51] Reactive ion beam was used for Al etching and understanding of molecule dissociation.[52, 53] The ion beam and atom (or molecular) beam have been used in detail kinetic research of SiO_2 etching, to collect fundamental data for modeling.[54, 55]

4.2 Experimental Setup

Fig. 4.4 illustrates the schematic of the reactor system. Fig. 4.2 provides the reactor setup. Fig. 4.3 shows the setup of gas handing and control system. Fig. 4.3(a) is the

gas handling system , Fig. 4.3(b) is the Labview control system for gas handling system. The ion beam source (RF 25) and atom beam source (HD 25) were both purchased from Oxford Applied Research Inc. Their operation is based on inductively coupled plasma. Two separated power suppliers provide rf power (13.56 MHz) up to 600 W to each source. The reflected power was minimized to less than 1%. The ionization and dissociation ratio are decided by input power, gas species, and pressure in the discharge tube. For each source, three MFCs (mass flow rate controlers) were used to control the gas species and gas flow rate. The MFCs and valves were controlled by a Labview system through the computer with PCI 6052E, 6503, 6713 (National Instrument Inc.) The system has a base pressure of 2.0×10^{-8} Torr. Depending on the gas flow rate, the operating pressure for the system was around 6×10^{-5} to 6×10^{-4} Torr. Both H_2 and CH_4 were from Matheson Tri-Gas, Ar was from US airweld speciality gas. All gases are ultra high purity. A Baltzers 420 mass spectrometer was attached to the system.

The ion flux that is received by the substrate can be adjusted through source power, gas flow rate, screen grid voltage, and the distance between ion source and sample. The gas flow rate for the ion beam source and atom beam source was 5 sccm unless specified otherwise. The incident ion energy was set at the equivalent of screen grid voltage. The extract grid voltage was fixed at -110 V. A neutralizer was installed at the exit of the ion source and could be used to neutralize the ion beam. The distance between ion source exit and substrate was fixed to 2 positions. 7.6 cm for 400 to 700 V incident ion energy, 5.8 cm for 200 to 400 V incident ion energy. The ion beam was calibrated by a Faraday Cup (FC-72A, Kimball Physics). The FC has a ground grid, a retarding grid, and a suppression grid. The voltage on the suppression grid was set at -20 V to suppress secondary emission electrons. The FC system can measure the incident ion flux and the energy distribution. The receiving area for the FC was 1 cm^2. The calibration results show that typically at 200 W source power and 5 sccm Ar flow rate, the received ion current is 46 μA at 400 V and 77 μA at 700 V, equivalent to an ion flux 2.9×10^{14} and 4.8×10^{14} ions/cm^2s.

The reactive species generated by atom source reach the sample through gas flow. The atom source exit to sample distance was 2.5 cm. The source power was fixed at 300 W. The dissociation ratio, the gas flow rate, and the holes on the outlet plate decide the atom

flux to the sample. Two reflection plates at the exit of the atom source could further deflect possible residual ions in the beam. The method refered to as "the lost parent/precursor (LP) method" was used to estimate the dissociation ratio for the atom source.[56] This method is based on molecule dissociation and recombination: when plasma is on, the molecules are dissociated and recombined on the chamber wall. Therefore, by comparing mass spectrometer signal intensity with plasma off and on, the dissociation ratio can be estimated. The dissociation ratio for CH_4 based on the estimation was higher than 90% at 300 W input power and flow rate 5 sccm. This gave a radical flux around 6×10^{15} to 8×10^{16} /atoms (or radicals) for 1% to 15% CH_4. Since CH_4 dissociation generates H atoms, the atom flux of H is equivalent to CH_4 dissociation plus the dissociation of H_2 molecules, which was estimated as 5% by D_2 from previous research by similar method. The atom or radical concentration in the discharge tube can also be measured indirectly by an OED (optical emission detection) system by measuring the light emission intensity (Oxford Applied Research Inc.). The OED reading was used to monitor the reproducibility and stability for experiments.

4.3 Ion Beam Calibration

The ion incident energy on the target is decided by the voltage on the acceleration grid. The ion fluence is decided by the ionization ratio and the electric field between the acceleration grid and extraction grid. The input power and the discharge tube pressure, which is controled through the gas flow rate, together decide the ionization ratio for a given gas species.

Fig. 4.5 illustrates the change of ion fluence with different input power and acceleration voltage at Ar flow rate 10 sccm. Generally, lower input power had lower ion fluence. Ion fluence at 50 W input power was the lowest. Before 300 V acceleration voltage, the ion fluence from 50 to 300 W input power, especially below 200 V, were very close. After this acceleration voltage, the input power began to show stronger effect in affecting the ion fluence. For example, at acceleration voltage of 1000 V, the ion fluence for 100 W was 50 μA/cm^{2}s, for 300 W, it was 118 μA/cm^{2}s. Therefore, in order to change the ion

fluence effectively by changing the input power, the acceleration voltage needed to be higher that 400 V. Besides the input power, the acceleration voltage had a strong effect on the ion fluence. The ion fluence increased with increased acceleration voltage. When the input power was higher than 100 W, the ion fluence increased very fast with increased acceleration voltage. For example, at input power of 200 W, ion fluence changed from 37 μA/cm^{2}s at acceleration voltage of 400 V to 81 μA/cm^{2}s at 800 V, increased more than two times. Therefore, increase acceleration voltage will increase ion fluence and incident ion energy.

Fig. 4.6 shows the change of ion fluence with Ar flow rate. The input power was 200 W, acceleration voltage was 500 V. The ion fluence had a maximum value at flow rate 2 sccm. It remained relative stable between 2-5 sccm. Below flow rate of 2 sccm, the ion fluence dropped very fast. Possibly the gas pressure in the discharge tube was too low to sustain a reasonable ionization ratio. Above flow rate 5 sccm, the ion fluence decreased slowly, from 88 μA/cm^{2}s at flow rate 5 sccm to 17 μA/cm^{2}s at flow rate 25 sccm. For a fixed source power, the ionization ratio was decided by both electron mean free path and collision frequency. The increased flow rate increased the pressure in the discharge tube, it increased the collision frequency but at the same time it decreased the electron mean free path, which reduced the kinetic energy of electrons. Therefore, the ionization ratio was optimized at approximately 5 sccm.

Besides changing source power and flow rate, changing distance between ion beam exit and sample can also modify the ion flux. With reduced distance, the ion flux increased.

Fig. 4.7 shows the ion energy distribution at three acceleration voltages, 300, 500, and 800 V with Ar at input power of 200 W. This measurement verified the uniformity of ions in the desired energy level. It was done by setting the ion beam at fixed acceleration voltage, then measure the current with changed voltage on the retarding grid of FC. The left ordinate shows the change of ion fluence with the retarding grid voltage on the FC. It shows that the ion fluence slowly decreased with increasing retarding voltage and reached a cut off point when the retarding voltage surpassed the acceleration voltage of the ion beam source. The right ordinate shows the differentiation of ion fluence change with

the retarding voltage. The result shows that the differentiation had a sharp peak at the acceleration voltage for every acceleration voltage. For example, at 500 V acceleration voltage, a sharp peak is seen at 500 V by differentiation. The small peak at 50 V compared with this sharp peak could be neglected. This measurement shows that the ion energy distribution was relatively uniform within the ion beam.

4.4 Atom Beam Calibration

As explained in the experimental section, the dissociation ratio for the specified gas was estimated by measuring the signal intensity with plasma off and on with a mass spectrometer. To monitor the operation of atom beam, it is convenient to use the OED system by monitoring the light intensity. The signal quality can be improved by choosing proper light filter to monitor specified excited atom state. The OED measurement was used to analyze the effect of input power and gas flow rate.

Fig. 4.8 shows the OED readings change with Ar flow rate at input power of 50 W, and the change with H_2 flow rate at input power of 200 W. The OED reading for Ar gas increases drastically when flow rate changed from 0.25 sccm to 1 sccm. The reading reaches a maximum at 2 sccm. Then it slowly decreases with further increased flow rate. H_2 gas had very similar behavior as Ar gas. The OED reading reaches a maximum at flow rate of 2 sccm, and it drops when flow rate was higher than 2 sccm. The measurement suggestes that the best operation range is approximately 2 sccm for Ar or H_2.

Fig. 4.9 shows the OED reading change with input source power for Ar and H_2. Ar flow rate was 1 sccm and H_2 flow rate was 2 sccm. For Ar, a drastical change of OED reading is observed between 25 W to 50 W input power. This is due to the change of operation mode. When input power was too low, the source was operated in capacitive mode. After 50 W, for Ar the source was operated at inductive mode, which gave much stronger light intensity. For H_2, the OED reading steadily increases with input power to a stable value at 400 W input power. The H_2 was operated on inductive mode in the whole measurement range.

Fig. 4.10 shows the change of signal intensity detected by mass spectrometer. The

atom source was adjusted from 0 to 300 W, with 5 sccm total flow rate, 10% CH_4 and 90% Ar. The monitored signals were for m/e=16 and m/e=15. The CH_4 was dissociated and recommbined on the chamber wall, therefore, the signal detected by the mass spectrometer was reduced. By comparing the difference, then the dissociation rate was estimated. As described in experimental set up, the CH_4 dissociation rate according to this method was more than 90% at 300 W.

4.5 Conclusions

A beam reactor system was built for plasma etching mechanism research. Both ion beam and atom beam are commercially available. The ion beam was calibrated by a Faraday cup system. The ion current was measured for different source power, flow rate, ion voltage, and distance between ion beam exit and sample. The ion flux increased with source power and ion voltage. For a fixed source power, an optimized flow rate was obtained at approximately 5 sccm to maximize the ion flux. The reduced distance gave higher ion flux in the sampling position. Therefore, for a fixed ion voltage, chaning source power, flow rate, or distance can give different ion flux. The atom flux was calibrated by an OED system. Different gases, flow rate, and source powere were calibrated. Higher source power increased the atom flux. Similarly, as in ion beam calibration, there was an optimized gas flow rate for maximizing atom flux in a fixed source power. The dissociation ratio was esitmated by mass spectrometer in comparison of signal intensity between plasma off and on. At 300 W and 5 sccm gas flow rate, more than 90% dissociation ratio for methane was estimated based on this method.

4.6 Figures

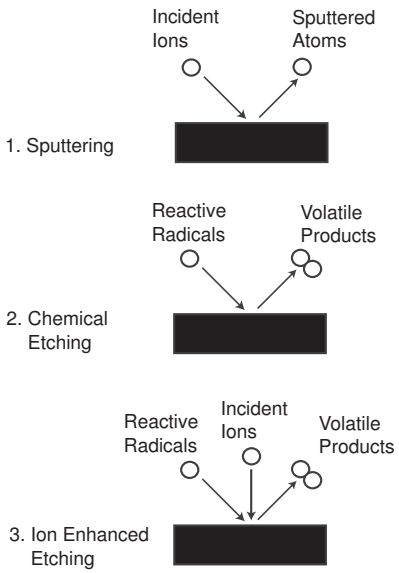

Figure 4.1: Schematic illustration of general plasma etching mechanisms: sputtering, chemical etching, and ion enhanced etching.

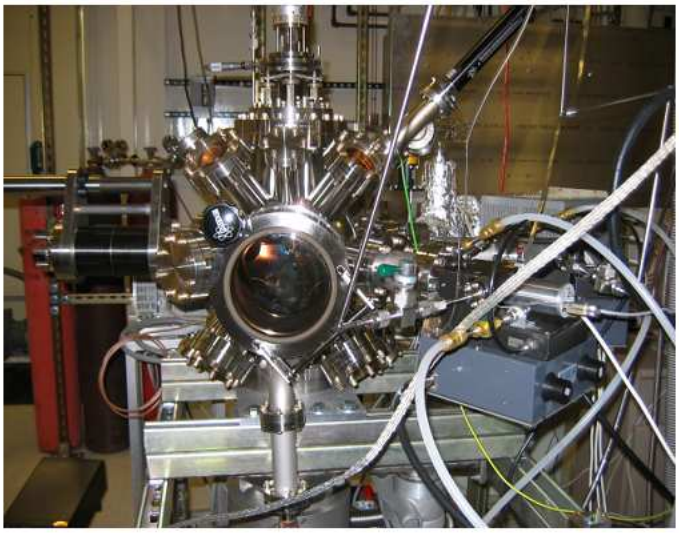

Figure 4.2: Photo for beam reactor system

(a) Photo of gas handling system

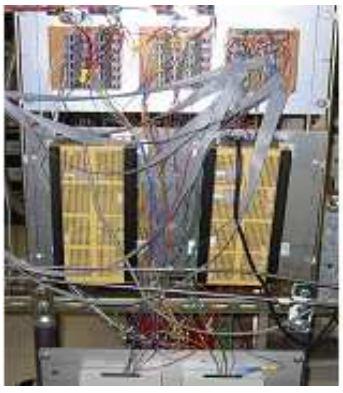

(b) Photo of Labview control electrical setup

Figure 4.3: Photos of gas manifold and Labview controlling system of the beam reactor system.

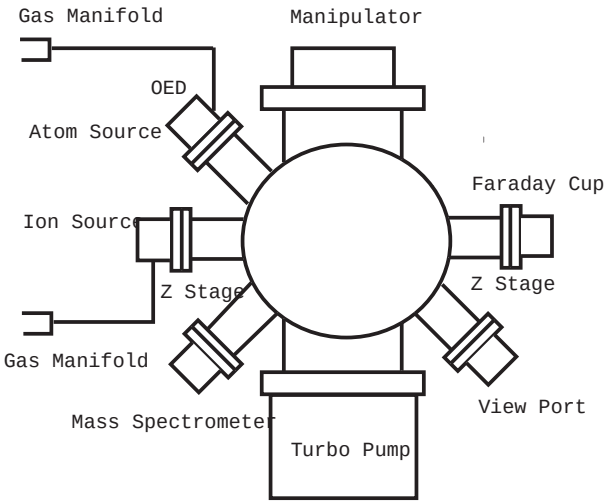

Figure 4.4: Schematic of experimental system, showing atom source, ion source, Faraday Cup, manipulator, mass sepctrometer, gas manifold.

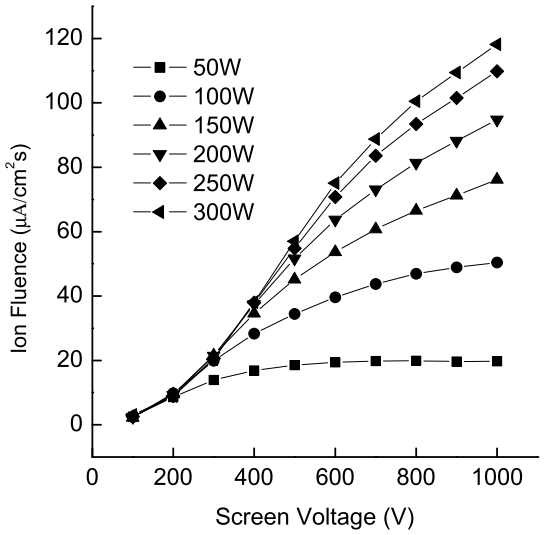

Figure 4.5: The ion fluence change with source power 100, 200, 300 W, acceleration voltage 50-1000 V, at Ar flow rate 10 sccm

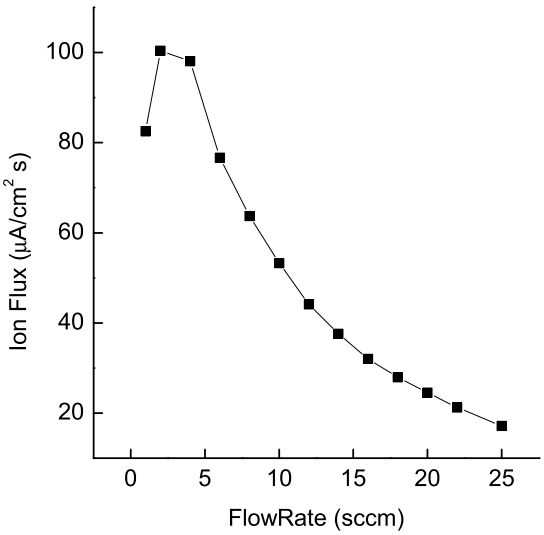

Figure 4.6: The ion fluence change with gas flow rate for Ar, at input power of 200 W, acceleration voltage of 500 V

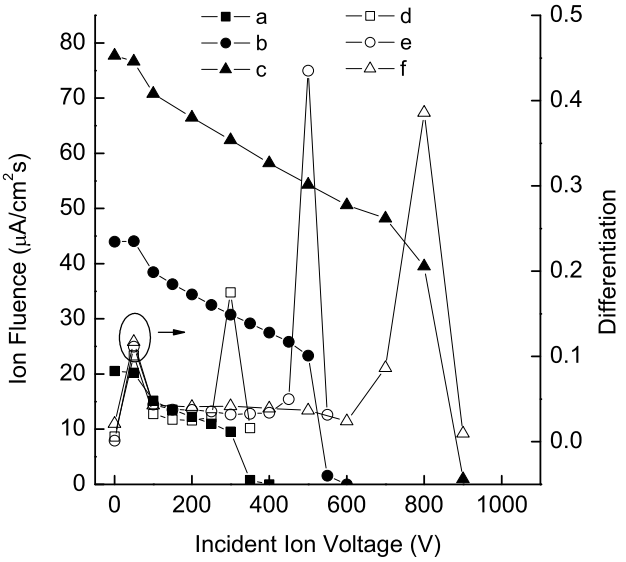

Figure 4.7: Ion energy distribution for Ar flow rate at 10 sccm, input power of 200 W, acceleration voltage of 300, 500, 800 V. Ionfluence change with changed retarding voltage for 3 different incident ion energy: a. 300 V; b. 500 V; c. 800 V. The differentiation of ion fluence with changed retarding voltage for 3 different incident ion energy: e. 300 V; f. 500 V; g. 800 V.

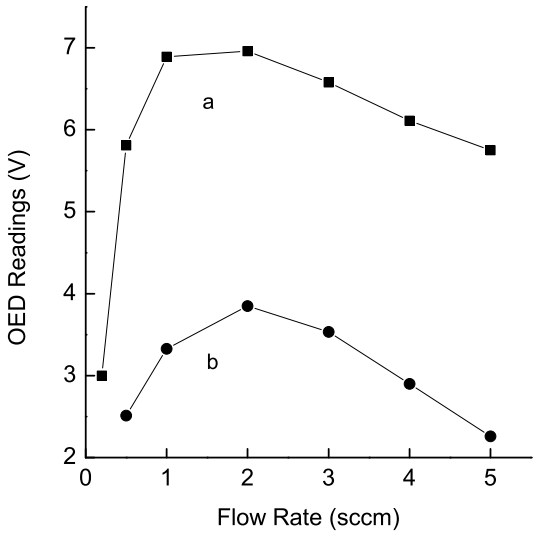

Figure 4.8: OED readings change with: a. H_2 gas flow rate at input power of 200 W; b. Ar gas flow rate at input power of 50 W

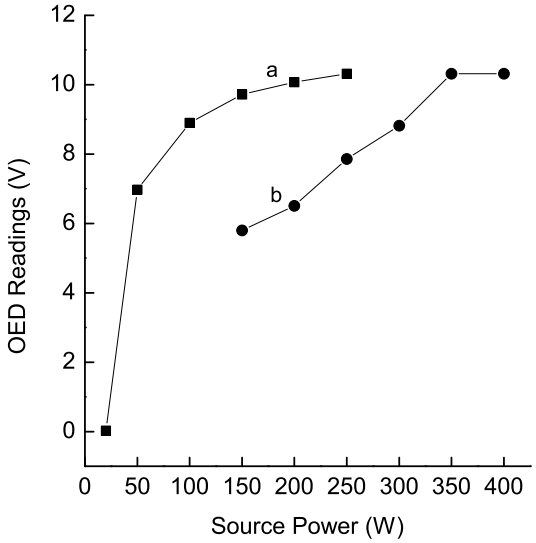

Figure 4.9: OED readings change with input power for: a. Ar flow rate at 1 sccm; b. H_2 flow rate at 2 sccm

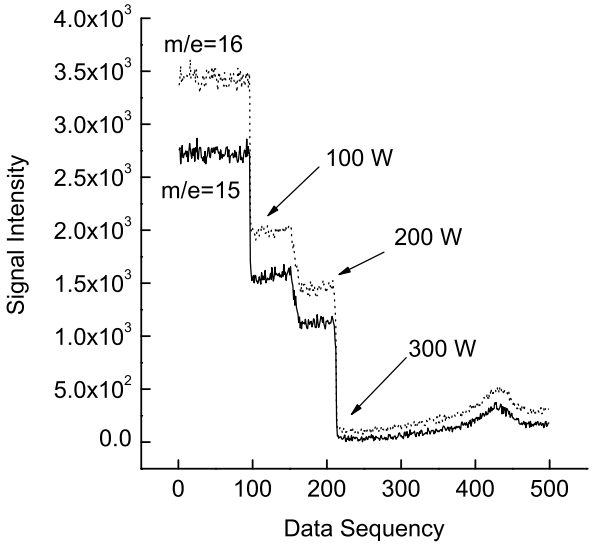

Figure 4.10: The signal intensity comparison of m/e 16 and m/e 15 for CH_4/Ar, atom source power from 0 to 300 W, total flow rate 5 sccm, CH_4 10%

CHAPTER 5

Removal of Silanol from Porous Silicon Dioxide Based Low-*k* Films Using Hydrogen Atoms

5.1 Introduction

With the increase in microelectronic device density, low-*k* dielectric films are needed for devices interconnection to reduce power consumption and cross talk between metal lines, for next generation of device manufacturing.[57, 58] These low-*k* films not only need to have lower *k* values, but also need to have proper chemical and physical properties that allow them to be integrated into the manufacturing line.[59] One problem related with the application of porous methylsilsesquioxane(*p*-MSQ) film, a promising candidate for ultra low-*k* materials,[60, 61] is the damage of films during pattern transfer.[62, 63] In the pattern transfer process, *p*-MSQ film is exposed to plasma in the dry etching process. After etching, O_2 plasma or N_2/H_2 plasma is used for photoresist ashing. Tests on these films showed that after the ashing process the *k* value usually increased over 3.0.[64, 65, 66, 67, 68] Silanol groups, which are generated in *p*-MSQ films during or after photoresist ashing, have been generally considered as the reason for the increase in the dielectric constant. [69, 70] Therefore, it is necessary to remove those silanol groups in order to restore the *k* value before the next integration step. Several approaches such as NH_3 plasma,[71] HMDS solution,[69] $ScCO_2$ with additives,[64, 65] have been used to repair the film to restore the *k* value.

Hydrogen plasma treatments have been used to improve low-*k* film properties.[72, 73, 74, 75, 61] Chang *et al* used H_2 plasma at 300 °C, up to 9 min for as-deposited *p*-MSQ film in a PECVD (plasma enhanced chemical vapor deposition) chamber to improve MSQ film properties.[61] The FTIR measurement, IV, and CV characterization proved H_2 plasma treatment improved film properties and reduced the damage during O_2 plasma ashing. Compared with unprocessed samples, the H_2 plasma treated samples maintained

a dielectric constant below 3.0 and leakage current remained below 10^{-7} A/cm^2 after ashing. Both copper diffusion and moisture taken were reduced. Cheng *et al.* used a 90 s H_2 plasma treatment at 300 °C for as-deposited MSQ and HSQ (Hydrogen Silsequioxane) films.[73] Compared with non-processed samples, the adhesion strength increased from 0.5 to around 2.0 N, leakage current remained less than 10^{-9} A/cm^2. Shieh *et al.* developed a double H_2 plasma treatment for fluorinated amorphous carbon films.[74] It was composed of a 3-9 minutes treatment at 250 °C before and after etching. The results showed that the thermal stability was improved, leakage current was reduced, and the damage caused by ashing was repaired. The film after ashing had a dielectric constant at 2.6. In these researches, it was belived that the H_2 plasma treatment improved film properties through passivating inner structure by satisfying the dangling bonds. The H_2 incorporation into the PECVD film such as α-Si,C:H, α-Si,Ge:H, α-Si,O:H at 100-350 °C and their bonds information have been investigated systematically by Lucovsky.[76] The interatcion between H and silanol groups was investigated in a CVD process for $SiH_4/O_2/H_2$ deposition. The H atom could remove silanol groups directly by forming water with them, or by breaking the O-H bond.[77]

In this research, an H atom beam was used to remove silanol groups from ashed *p*-MSQ samples. The purpose of using an atom beam rather than a direct application of plasma was to simplify the reaction mechanism by reducing ion and surface interactions. The goal of this research was to identify the possibility of a new process, to test different process parameters, and to understand the reaction mechanisms. It was expected in this work that the highly reactive H atom would react with silanol groups and remove them from ashed *p*-MSQ film. At the same time, the film properties would be improved.

5.2 Experimental setup

Fig. 5.1 illustrates the beam reactor system for this work. For detailed information on the beam system and the atom beam calibration and operation refer to chapter 4. In this setup, a sample was mounted on a stage, which consisted of a Kapton heater and was connected to an Omega temperature controller. The heater covered the stage surface, the

thermocouple was sandwiched between the sample and the heater. The stage was attached to a rotatable 3-D manipulator. The space between the sample and atom source exit was 2 cm. A sample was kept out of line-of-sight of the atom source and rotated into the normal position to the atom source when began to count the exposure time after the plasma was on. After the process, the sample was cooled down in the vacuum and then taken out and transfered to FTIR measurement chamber.

Silicon wafers (100 orientation, 200 mm p-type with minimum resistivity of 0.5 ohm$\cdot$ cm) covered with a spin-on methylsilsesquioxane (MSQ) film (JSR LKD 5109) were supplied by Sematech. The *p*-MSQ films were ashed in an oxygen plasma after curing and had a nominal film thickness of 3600 Åand approximately 40% porosity. The dielectric constant of the cured film was approximately 2.4$\pm$0.1 and that of the ashed films was 3.5$\pm$0.1 due to the presence of polarizable O–H groups.[64] The silicon wafers were cleaved into 2$\times$2 cm^2 pieces for processing.

Transmission Fourier transform infrared (FTIR) spectroscopy (Nicolet Nexus 670, MCT/A detector) was used *ex situ* to monitor chemical changes in the low-*k* films (200 scans at 4 cm^{-1} resolution). For low concentration, FTIR absorbance is directly proportional to the concentration of functional groups as shown by Beer's law,[78]

$$A = \varepsilon l c \tag{5.1}$$

where A is absorbance, ε is absorptivity, l is pathlength, and c is concentration. Based on Beer's law, by assuming same ε and l, the integrated FTIR spectrum peak area (absorbance) was used to indicate the silanol groups. The removal fraction was obtained by referencing the difference of the post-process to the initial peak area for wavenumber 3151-3799 cm^{-1}.[64, 65] All spectra were referenced against a bare silicon background spectrum. Film thickness was measured using a spectroscopic ellipsometer (J. A. Woollam Co. M-2000). The model that was used for the calculation of film thickness applied a standard Cauchy distribution for a film stack containing a Si substrate and a *p*-MSQ film. The difference between initial film thickness and processed film thickness yielded the etched thickness. The surface energy was determined by measuring the contact angle of DI water (18.2 $\mathrm{M\Omega \cdot cm}$) with a volume of 10 μL using a goniometer (Rame-Hart Inc.

Model 100-0).

5.3 Results

Fig. 5.2 shows the transmission FTIR spectra for vacuum heating at 150±4 °C for 1 h and H atom beam treatment at 150±8 °C with 300 W source power for 3 min. The wavelength regions associated with functional groups that are of interest (marked by dotted line) are as follows: isolated silanol SiO-H (3749.0 cm^{-1}), hydrogen-bonded silanols SiO-H (3151-3701 cm^{-1}), asymmetric (2977 cm^{-1}) CH_3 stretches, Si-CH_3 deformation (1277 cm^{-1}), Si-O-Si stretches (cage) 1134 cm^{-1} and (network) 1062 cm^{-1}, and Si-OH stretch 942 cm^{-1}.[79, 80] Based on these peaks identification, removal fraction was calculated for silanol groups at 3151-3799 cm^{-1}. Several important features can be seen in Fig. 5.2. First, through the H atom beam process, silanol groups in the wavenumber range of 3151 to 3799 cm^{-1} were reduced since the difference spectrum presented a clear negative peak in this range. This can also be related to the reduced peak of Si-OH stretch at 942 cm^{-1}. But the change of silanol groups by vacuum heating was only around 20% of the removal fraction by H atom beam process. Second, the intensity of both CH_3 asymmetric and deformation peaks decreased after H atom beam process, which indicates the loss of methyl groups from the film, which did not happen in vacuum heating. Third, H atom process decreased Si-O-Si stretches (cage) 1134 cm^{-1}, which was only slightly affected by vacuum heating. For Si-O-Si stretch 1061.5 cm^{-1} (network), both processes formed two peaks in the difference spectra, 1071 cm^{-1} and 1011.1 cm^{-1}, which indicated that both processes shifted the Si-O-Si stretch 1061.5 cm^{-1} (network) peak location. The change was stronger for H atom beam treatment compared with vacuum heating process. Similar shifting due to H atoms were observed in the literature and the inductive effect of Si-Si bonds in the oxide network was suggested as the reason.[77] These changes indicate possible chemical reaction and film etching between H atom and *p*-MSQ film. The difference spectra show that the removal of silanol groups mainly happened between 3200 to 3700 cm^{-1}, which means the H bonded silanol groups were removed. The peak at 3749 cm^{-1} increased slightly for vacuum heating and more obvious for H atom process

that indicated the addition of isolated silanol groups for both processes. For the isolated silanol groups, both original peak intensity and the intensity change during the process were much smaller compared with H bonded silanol groups, therefore, the addition of isolated silanol groups on the removal fraction calculation was trivial.

The relationship between the H atom beam process time, the total removal fraction of silanol groups, and the film thickness change are illustrated in Fig. 5.3. All experiments were conducted at substrate temperature 150 °C, except the $\triangle$ and $\bigtriangledown$ data points were obtained at room temperature with H atom beam exposure for 5 min. The zero minute process time means that the sample only experienced vacuum heating around 1 h in the absence of the H atom process. Without the H atom beam, the removal fraction by vacuum heating was 11%. Vacuum heating with H_2 purge (p<5×10^{-4} Torr) was tested and the result showed no obvious difference with vacuum heating without gas purge. At room temperature, 5 min H atom exposure only removed 15% silanol groups. But at substrate temperature 150 °C, once the sample was exposed to the H atom beam, the removal fraction increased dramatically. A 0.25 min H atom beam process removed 37% silanol groups, close to 4 times higher than vacuum heating process. The removal fraction increased to 50% for 1 min H atom exposure, then increased slowly with further extended exposure time. It is 56% for 5 min H atom beam treatment at 150 °C, which was more than 3 times higher than the H atom beam treatment without heating. Therefore, the combination of vacuum heating and H atom beam process was much more effective in removing silanol groups than using them separately. Fig. 5.3 also shows the relationship between film etching and H atom beam process. With H atom beam treatment at 150 °C substrate heating, the etching rate was calculated as 14±1 Å/min. At room temperature, the calculated etching rate was much lower, around 3 Å/min.

Fig. 5.4 illustrates the relationship between source power, silanol groups removal, and film etching. The samples in Fig. 5.4 were processed with 3 min H atom exposure with source powers from 200 to 400 W at 150 °C. When the source power changes from 200 to 400 W, the removal fraction of silanol groups only changes around 5%, but at an input source power of 400 W, approximately 103 Åp-MSQ film was etched in 3 min, which was 6 times higher than the thickness change at a source power of 200 W.

The relationship between the substrate temperature and the silanol groups removal fraction is presented in Fig. 5.5. All samples were processed for 5 min with 300 W source power. The data at room temperature was obtained from the sample that was not exposed to intentional sample heating. The removal fraction at this temperature was 15%. When the temperature increases to 150 °C, the removal fraction is 56%, an increase of more than three times. Therefore, in the temperature range from 20 °C to 150 °C, the removal fraction increased with the substrate temperature around 3∼4 times. Due to the limitations of the equipment used and the sensitivity of *p*-MSQ films to further heating, no higher sample temperatures were tested. The Arrhenius plot was used for the estimation of activation energy.

Two samples, which both were processed at 150 °C for 3 min H atom process were tested with different N_2 purge time inside the FTIR measurement chamber. The results show that silanol groups intensity increases slightly with purging time, which indicates that the surface possibly regained silanol groups in the FTIR measurement chamber due to residual water vapor. The goniometer measurement showed that the surface remained hydrophilic after the H atom beam process ($<20°$). The aging test showed that after one or two days of exposure to the atmosphere, the H atom beam processed samples would regain their silanol groups as before.

5.4 Discussion

The FTIR spectra showed that by heating the samples under vacuum at 150 °C, the peak intensity in the wavenumber range 3151-3690 cm^{-1} was decreased slightly, and at wavenumber 3690-3799 cm^{-1} the peak intensity increased slightly. Because the absence of the 1620 cm^{-1} HOH deformation mode indicated that no physically adsorbed, or H bonded water was presented on the *p*-MSQ samples.[69, 1] The peak intensity change was considered due to the silanol groups condensation. Similar condensation behaviour of silanol groups was observed by Morrow *et al.* for a silica surface heated from 150 to 450 °C.[1] The condensation mechanism for H bonded silanol groups was proposed as in Fig. 5.6.[1, 4] It shows that under vacuum heating, the H bonds between three -OH

neighbours were broken, a siloxane bridge was built between two Si atoms and formed one isolated Si-OH and water. Water was then desorbed from the surface by heating. In this research work, this reaction mechanism was supposed for the FTIR spectrum change *p*-MSQ film during vacuum heating. The condensation ratio at 150 °C was low since the removal fraction of silanol groups was only 11%.

The experimental results for the H atom beam process at substrate temperature 150 °C show the removal fraction by this process was three to four times higher compared with vacuum heating at 150 °C or H atom beam process at room temperature. It suggests that the H atom beam process combined with heating has very different mechanisms in removing silanol groups compared with either vacuum heating or H atom process without heating. H_2 molecules are not reactive to silanol groups,[81] but H atom as a reactive species is expected to react with silanol groups to form water. For isolated silanol groups, H atoms reacted with -OH bonds directly and formed $\mathrm{H_2O}$, then $\mathrm{H_2O}$ desorbed from the surface.[77]

$$\mathrm{Si-OH + H \rightarrow Si-OH \cdots H} \tag{5.2}$$

For H bonded silanol groups, it is possible that the H atoms first react with -OH groups that without H bonding to form $\mathrm{H_2O}$. Then the water desorbed from the surface and opened another -OH group for reacting with the H atoms as in Fig. 5.7.

Further understanding of the mechanisms could be obtained through the experimental results of different substrate temperatures with the H atom beam process. From room temperature to 150 °C, the removal fraction for silanol groups increased three to four times. The estimated apparent activation energy for the process was 2.4 kcal/mol, which is close to a typical H radical reaction with C_2H_4 (2.0 kcal/mol),[82] but low for typical water desorption activation energy (16.6 kcal/mol) from silica surface.[4] A possible explanation is related to H_2 dissociation inside the plasma: H_2 molecules can be dissociated through different potential interaction paths, for certain dissociation reactions hot H neutral fragments were generated. For example, at a threshold energy of ∼8.8 eV, there is excitation to the repulsive $^3\Sigma_u^+$ state followed by dissociation into two fast H fragments that each carrying ∼2.2 eV.[28, 83] When the hot H atoms react with silanol groups, water was formed, at the same time the carried kinetic energy by H atom could weaken the

surface bonds between Si and the products. Therefore, the bonds between the surface and the products were not as strong as physically adsorbed water. Since the bond strength between Si and product-water was already weakened, the energy needed to desorb the water from the surface is lower compared with typical desorption energy. Heating is still needed to provide the activation energy for the desorption,[1, 4, 3, 84, 2] but the energy was lower compared with typical water desorption process on silica surface.

The experimental results show that the removal fraction of silanol groups was not strongly related with film etching. For example, in Fig. 5.3 around 50% silanol groups were removed, film loss was less than 20 Å. When film was etched close to 100 Å, the removal fraction was 57%, only increased 7%. Similar results were also shown in Fig. 5.4. With more film etched, the removal fraction did not increase accordingly. These results suggest that big amount of silanol groups should be on the film surface within 20 Å. Therefore, etchng more *p*-MSQ film could not be effective in removing silanol groups. The removal fraction in current work reached a limit around 60%. This limitation could be explained by several possible reasons. First, there is a possible thermal equillibrium between the film and the gas phase. Since the water in the chamber could react with the surface and reform silanol groups.[77] The mass spectrometer showed a water partial pressure around 4×10^{-8} Torr during beam treatment. Since increasing temperature increased removal fraction, it suggests a possibility that the removal fraction was limited by thermal equillibrium. Second, silanol groups may be partly trapped inside the film due to the high porosity, therefore, they were difficult to react with H atom or to be desorbed from the film. However, since increase process time did not increase the removal fraction, this may not be a strong factor. Third, the surface may be rehydroxylated during the exposure to the atmosphere. Literature suggested the rehydroxylation of dehydroxylated silica surface could be very fast.[4]. The experiment with different N_2 purge time inside the FTIR chamber indicated that the surface can regain the silanol groups. Therefore, it is possible that the surface experienced a fast rehydroxylation during the transfering process from the vacuum chamber to the FTIR measuremnt chamber. The rehydroxylation of the surface for the formation of isolated silanol groups (Fig. 5.8(a)) and H bonded silanol groups (Fig. 5.8(b)).

The H atom not only reacted with silanol groups, but also reacted with methyl groups and as well as Si-O-Si. This can be confirmed by both FTIR spectra and ellipsometer measurements. The reaction between H and methyl groups formed methane and a broken bond as in Eq. 5.3.[63] The etching of silica by the H atom was suggested as in Eq. 5.4.[85, 86, 84] The etching mechanism for *p*-MSQ film by the H atom could possibly be the same. The etching caused broken bonds and isolated silanol groups.

$$\mathrm{Si} - \mathrm{CH_3} + \mathrm{H} \rightarrow \mathrm{Si} * + \mathrm{CH_4} \tag{5.3}$$

$$\mathrm{Si} - \mathrm{O} - \mathrm{Si} + \mathrm{H} \rightarrow \mathrm{Si} * + \mathrm{Si} - \mathrm{OH} \tag{5.4}$$

The formed broken bonds were possibly exist as dangling bonds or were satisfied by H atom. Thermodynamically, Si-O bond is 191 kcal/mol, Si-H is 84-100 kcal/mol, HO-H is 119 kcal/mol, O-H is 78-107 kcal/mol, the reactions of H atom and broken bonds should be more energy favorable.[85] H_2 plasma had been proved to be effective in passivating low-*k* films,[73, 74, 75] therefore, it was expected that H atom could satisfy those broken bonds by forming Si-H. However, no Si-H peak was identified in FTIR spectra. It is possible that the signal intensity was not strong enough. Another possibility was due to the hot H atoms as discussed in previous section. The H carried extra kinetic energy may cause the Si-H in an unstable state and can be easily dissociated or react with H atom as suggested by [77]

$$\mathrm{H} + \mathrm{Si} - \mathrm{H} \rightarrow \mathrm{Si} * + \mathrm{H_2} \tag{5.5}$$

5.5 Conclusion

The H atom beam with substrate heating was used to remove the silanol groups on *p*-MSQ samples that were generated during the photoresist ashing process. Up to 57% of silanol groups were removed in a three minute process at 150 °C. This process caused an film etching rate of 14 Å/min. A parametric study revealed that chemical reactions between H atom and silanol groups and the substrate heating temperature were important to remove silanol groups. The activation energy required to desorb the product was suggested as the requirement for substrate heating. The H hot neutral fragments which were generated in

plasma dissocation that reacted with silanol groups may weaken the bonds between Si and product at the same time. The H atom also reacted with methyl groups and broke the siloxane bridge. These reactions caused broken bonds and had to be satisfied to obtain stable surfaces before being exposed to the atmosphere. FTIR measurement with different N_2 purging time and the aging test results suggest that the surface can be rehydroxylated.

5.6 Future work

To complement the results presented here, we suggest the following work:

- *in-situ* FTIR measurement, since exposure to the surface may cause rehydroxylation, an *in-situ* measurement will give more meaningful data in recognizing the mechanisms;
- CH_3 group addition by UV activated methanol groups, expected reaction with methanol with dangling bonds or isolated silanol groups.

5.7 Figures

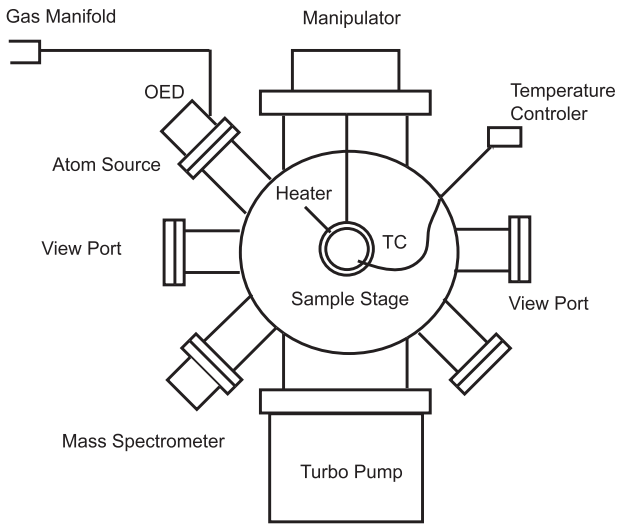

Figure 5.1: Schematic of experimental high vacuum atom beam system showing: atom source, sample stage with heater and thermocouple (TC), temperature controler, manipulator, mass sepctrometer, gas manifold.

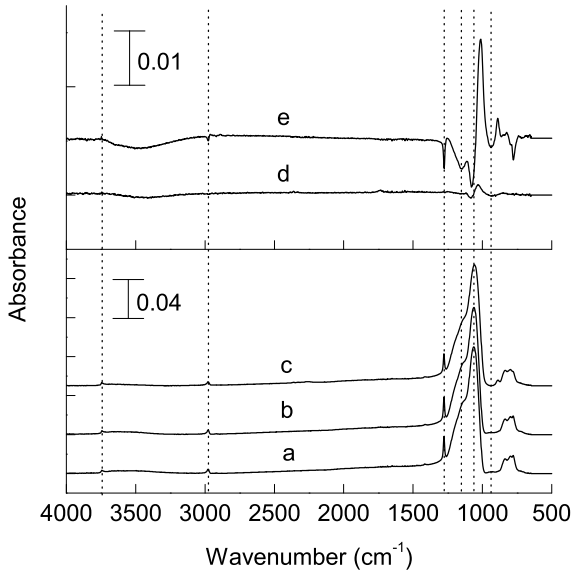

Figure 5.2: FTIR spectra of plasma ashed *p*-MSQ film: (a) initial; (b) after exposing to vacuum heating at 150 °C for 1 h; (c) after a H_2 atom beam treatment, for a plasma source power of 300 W, substrate temperature 150 °C, 3 min exposure. Difference spectrum of post-process minus pre-process: (d) by vacuum heating, (b)-(a); (e) by H_2 atom beam process, (c)-(a). Peak assignment identified by dotted lines: isolated silanol SiO-H (3749.0 cm^{-1}), hydrogen-bonded silanols SiO-H (3151-3690 cm^{-1}), asymmetric (2977 cm^{-1}) CH_3 stretch, Si-CH_3 deformation (1277 cm^{-1}), Si-O-Si stretches (cage) 1134 cm^{-1} and (network) 1062 cm^{-1}, and Si-OH stretch 942 cm^{-1}.

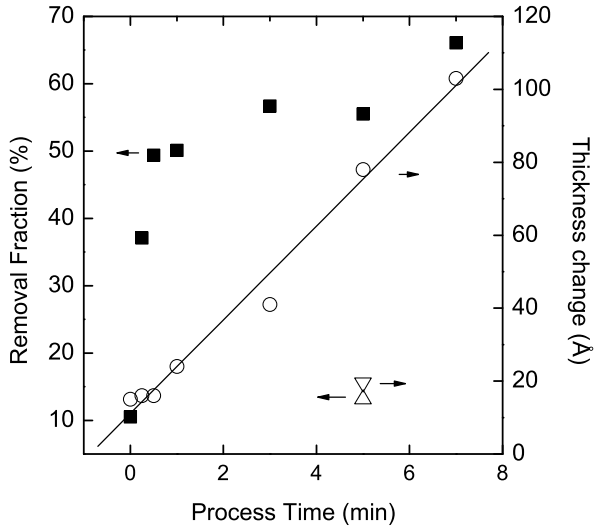

Figure 5.3: The fraction of silanol group removal and the change in *p*-MSQ film thickness as a function of H atom beam process time at a beam source power of 300 W and substrate temperature of 150 °C. Heat only at t=0, H atom beam only of △ and ▽. The data points of ■ were for silanol groups removal fraction, ◯ were for film thickness loss. Norminal film thickness 3600 Å.

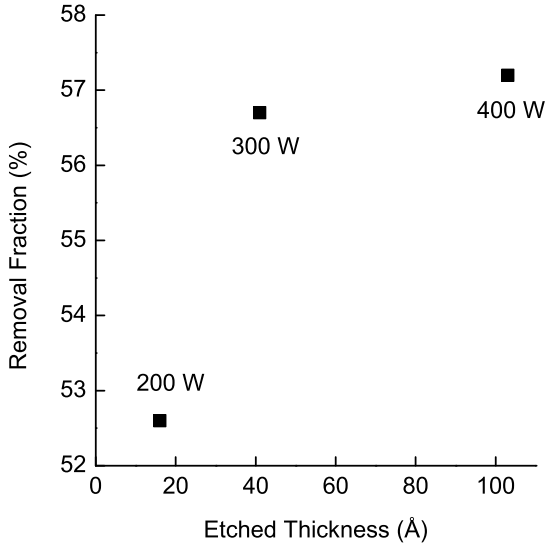

Figure 5.4: The change of removal fraction of silanol groups and film thickness change for *p*-MSQ with different H atom source power at 200, 300, and 400 W at 150 °C.

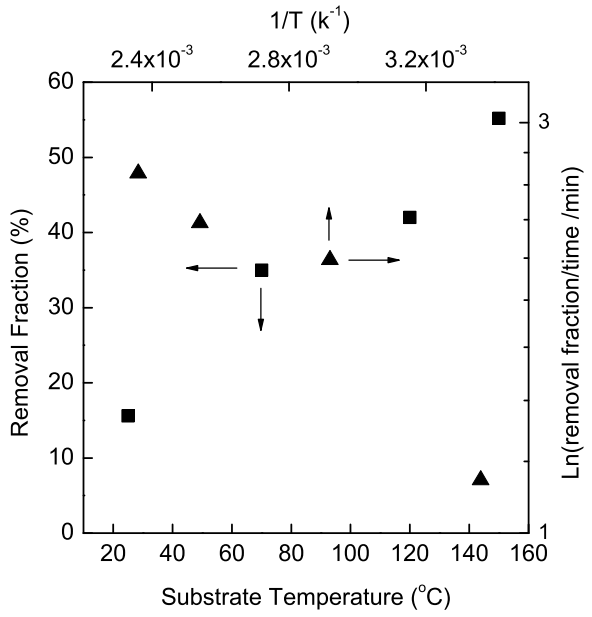

Figure 5.5: The change of total removal fraction of silanol groups with different substrate temperature and the Arrhenius plot. Source power 300 W, process time 5 min.

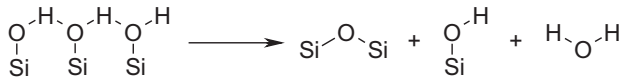

Figure 5.6: The condensation mechanism for H bonded silanol groups during vacuum heating process.[1, 2, 3]

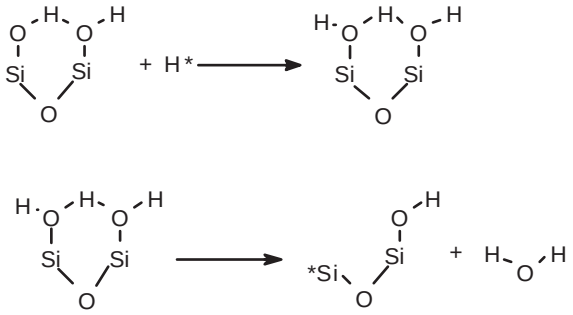

Figure 5.7: The dehydroxylation mechansims for removing silanol groups by H atom beam process with substrate heating for H bonded silanol groups.

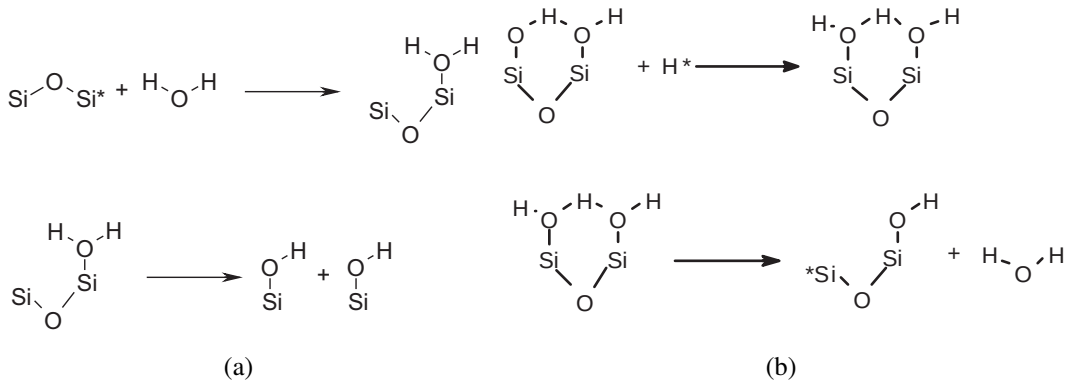

Figure 5.8: The rehydroxylation mechanisms of broken bonds with water vapor: (a) broken bonds formed by removing isolated silanol groups; (b) broken bonds formed by removing H bonded silanol groups.[4]

CHAPTER 6

InP Etching by Ion and Atom Beam

6.1 Introduction

InP as a III-V semiconductor material has higher saturation electron mobility and larger internal energy gap. This provides an advantage for device performance in semiconductor lasers, optoelectronic devices and high speed electronic devices.[87] For InP patterning transfer, generally two kinds of plasma chemistry are used. They are Cl_2 based etching or CH_4/H_2 based etching.[88] In Cl_2 based etching, generally $InCl_3$ and PCl_3 are considered as major etching products. The etching process requires a minimum substrate temperature around 150 °C for etching to proceed. The low volatility of $InCl_3$ is considered as main reason.[89, 90, 91, 92, 93, 94] In an effort to reduce the temperature and improve etching quality, different halogens such as iodine based and bromine based gases have been used.[95, 96, 97, 98] CH_4/H_2 based plasma etching does not require a high substrate temperature and obtained good etching qualities. Generally $In(CH_3)_3$ and PH_3 are considered as major etching products. Problems of this process are relatively lower etching rate and high polymer deposition.[99, 100, 101, 102, 103, 104, 105] Inductively coupled or electron cyclotron resonant plasmas have been applied in the etching process in order to improve the etching rate.[106, 107, 108, 109] The etching mechanism have been discussed. [110, 111] Besides these two kinds of chemistries, other gases and combinations have also been tested.[98]

Beam technologies have been used to etch InP for device manufacturing. The chemistry for beam etching of InP is mainly Cl_2 based or CH_4/H_2 based.[48] Two kinds of beam technologies are frequently used. They are RIBE (reactive ion beam etching), in which ion beam is generated by reactive etching gas directly,[112, 113, 114, 115, 116, 117, 118] and CAIBE (chemically assisted ion beam etching), in which inert gas is used to generate the ion beam, reactive gas is delivered to the target directly.[119, 120, 121, 122, 123,

124, 125, 126] Pure atom beam without incident ions,[127] or reactive atom beam with inert ion beam have also been tested.[128] The difference between RIBE and CAIBE was analyzed by Carlstrom *et al.*[129] Other gases such as N_2/O_2 have also been tested.[130]

Beam technologies have proved to be a useful tool in understanding etching mechanisms for plasma etching.[50, 52, 54, 55] They can simplify the plasma chemistry by decoupling the reactive radicals and incident ions, therefore helping to understand and identify the different roles of ions and atoms in the reaction. In the current work, the detailed mechanism of beam etching of InP was investigated. Independently controlled ion beam and atom beam were used to investigate InP etching mechanism based on $CH_4/H_2/Ar$ chemistry. Different ion flux, ion energy, and component concentration were tested to obtain better understanding of the etching process.

6.2 Experimental Setup

Fig. 6.1 illustrates the schematic of the reactor system. For detailed information of ion flux and atom flux calibration, refer to chapter 4, the sample stage setup and temperature control refer to chapter 5. A sample was kept out of line-of-sight of both sources and rotated into the normal position to the ion source and 45° to the atom source when began to count the exposure time after the plasma was on. The (100) InP was doped with Fe and patterned by AZ 1512. The photoresist was hard baked at 150 °C to form a hard mask. The etching rate was measured by a profiler (Tencor-α stepper 500) after the cleaning of the photoresist. The XPS spectra were measured by a PHI 549 (Physical Electronics) with Al anode. The AFM measurements were taken in a Scanning Probe Microscope (Digital Instruments Dimension 3100).

6.3 Results

Three different types of operations were tested in the experiments as:

- IBE or sputtering, only ion beam with Ar gas was used, atom source was not used;

- CAIBE, chemical assisted ion beam etching. Ar gas was used for ion beam. Reactive gas flow through atom source, but source power was off;
- RBIBE, reactive beam and ion beam etching. Both sources were turned on. Ar gas was used for ion source, reactive gas was used for atom source.

For a more convenient comparison of experimental results, three different etching rates were presented.

- Etching rate, obtained by the etched depth and etching time, Å/min;
- Normalized etching rate, etching rate was normalized with ion current that calibrated by FC, Å/min μA;
- Yield, etched thickness was converted to atoms and normalized with ion flux, atom/ion.

The following equation was used for the yield calculation:

$$Y = \frac{ehd_m}{tjcos\theta} \tag{6.1}$$

where h is etched depth, t is time, d_m is atom density for InP as 3.96×10^{22} atom/cm^3, j is ion current, cosθ is incident angle and in normal incident as 1, e is electron charge. In the calculation, the preferential sputtering effect was neglected. Therefore, the yield was an approximation of apparent yield. Fig. 6.2 shows the etching rate relation with different ion beam source power and ion incident voltage. The data for 200 W source power were measured in the two voltage regimes, from 200 to 400 V and 400 to 700 V with different distance. The 400 to 700 V sputtering data for three different source powers show all similar linear relationships. Basically, higher ion energy has higher sputtering rate. At same ion energy, higher ion flux has higher sputtering rate. For example, at 200 W source power, the sputtering rate changed from 103 Å/min at 200 V to 860 Å/min at 700 V, at 600 V, the sputtering rate changes from 370 Å/min at 100 W to 787 Å/min at 300 W, which corresponds to an ion current change from 40 to 78 μA.

Fig. 6.3 shows the relationship of sputtering yield and incident ion voltage. The yield changes from 3.7 at 200 V to 11.7 at 700 V. The data from 400 to 700 V show a clear linear

relationship but below 300 V the data are more scattered. The higher non-uniformity of ion energy below this voltage could be a possible reason. A linear fit of the data shows a threshold voltage around 60 V. For comparison, the yield that were calculated from ion source power 100 and 300 W are also plotted in the same figure.

Fig. 6.4 illustrates the relationship between methane concentration and ion voltage with normalized etching rate in RBIBE mode. The ion source power was fixed at 200 W and atom source power was at 300 W. The H_2 concentration was fixed at 20% and the CH_4 concentration changed from 0 to 15%, with three different ion voltages, 300, 400, and 700V. The results at three different voltages show similar trend for the relation between etching rate and methane concentration. Generally the etching rate increased fast from 0% to 5%, after that it remains relatively stable. At same methane concentration, higher ion voltage gives higher etching rate; for example, at 15% CH_4, etching rate is 5.7 Å/min μA (429 Å/min) at 300 V and 13.8 Å/min μA (1069 Å/min) at 700 V.

Fig. 6.5 illustrates the relationship between incident ion energy and normalized etching rate in RBIBE. The atom source power was 300 W, input gas as 10% CH_4, 20% H_2, and 70% Ar. The normalized sputtering rate was also plotted for comparison. In RBIBE, the etching rate increases very fast with increased incident ion energy. The normalized etching rate is 4.4 Å/min μA (129 Å/min) at 200 V, but 13.1 Å/min μA (1010 Å/min) at 700 V, increase of more than 3 times. Therefore, ion energy is very important in improving etching rate. XPS results show that after ion energy 300 V, no C signal was detected after processing, consistent P depletion was observed. Under similar condition with ion energy 400 V, the temperature changed from room temperature to 150 °C, but etching rate change was not clearly observed.

Fig. 6.6 shows the relation between ion flux, ion energy, and etching rate for RBIBE. The atom source remained same operation condition as in Fig. 6.5. The ion source power changes from 100 to 300 W. At 200 W source power, the ion beam was operated in two regimes as described in experimental setup, 7.6 cm from source to sample for 400 ot 700 V, and 5.8 cm for 200 to 400 V. For all three different powers, the etching rate increased with ion voltage, similar as illustrated in Fig. 6.5. The etching rate was also strongly affected by ion flux. For the same ion voltage, the ion flux increased with source power,

the etching rate increased with source power was directly related with the increased ion flux. For example, at 600 V, the etching rates are 473, 794, and 953 Å/min for source power at 100, 200, and 300 W. The ion flux effect was further demonstrated in Fig. 6.7. In this figure, the atom source was fixed as in Fig. 6.6. The ion source power was 200 W with 400 V ion energy. But the distance between ion source and sample had been changed to obtain different ion flux. The result shows that the change of ion flux affects the etching rate. With ion flux changes from 53 to 81 μA, the etching rate changed from 547 Å/min to 818 Å/min. It can be approximated by a linear relationship.

In Fig. 6.8, the etching rate for RBIBE is compared with the sputtering rate for three ion source powers, 100, 200, and 300 W. The result shows that for 200 W source power, the ratio increased from 1.25 at 200 V to 1.53 at 400 V, then it dropped to 1.17 at 700 V. At source power 300 W, the ratio had similar trend as 200 W source power, but before 400 V, the ratio was more stabilized around 1.6. After 500 V, the ratio dropped to similar value as 100 and 200 W source power. The ratio was affected by both incident ion energy and ion flux.

Fig. 6.9 illustrates the hydrogen concentration affect in RBIBE mode. The atom source power was fixed at 300 W, CH_4 concentration was fixed at 10%, but H_2 concentration changed between 20% and 80%. The ion source power was 200 W and operated in two voltage regimes similarly as in Fig. 6.6. The result shows that below 400 V the etching rate for 80% H_2 is consistently higher than 20% H_2. For example, at 300 V, the etching rate is 5.9 Å/min μA (315 Å/min) and 7 Å/min μA (371 Å/min) for 20% and 80% H_2. Above 400 V ion voltage, the trend between two different H_2 concentrations is not clear, but the etching rates for both of them stay relatively close from 400 to 700 V.

In Fig. 6.10, three different operation conditions, sputtering, CAIBE, and RBIBE are compared. In both CAIBE and RBIBE, the gas mixture with 10% CH_4 and 20% H_2 were applied to the atom source. Generally, RBIBE provides the highest etching rate and sputtering has the lowest etching rate. For example, at 400 V, the etching rate for these three different situations are 275, 330, and 421 Å/min. However, above 500 V, the difference between CAIBE and sputtering is not clear, although RBIBE etching rates are consistently higher, CAIBE etching rate become even lower compared with sputtering.

For example, at 600 V, it is 639 Å/min for CAIBE and 628 Å/min for sputtering.

Fig. 6.11 illustrates the roughness change between four different processing conditons with ion energy 300 and 600 V by 5 min process. The experimental conditions were sputtering, CAIBE with 10% CH_4, 20% H_2, RBIBE with 10% CH_4, 20% H_2, RBIBE with 10% CH_4, 80% H_2. At 300 V, the roughness between sputtering and CAIBE were similar, both around 24 nm. But for RBIBE, the roughness was lower, they were around 18 nm for 20% H_2 and 14 nm 80% H_2. An increase in H_2 concentration decreases roughness. At 600 V, the sputtering causes very high roughness compared with other etching methods, around 141 nm, much higher than sputtering at 300 V (24 nm). The CH_4 chemistry strongly decreases the roughness. At CAIBE, the roughnessias 52 nm, almost 1/3 of the sputtering roughness. The RBIBE further decreases roughness to around 40 nm for both H_2 concentrations.

6.4 Discussion

The InP etching based on CH_4/H_2/Ar consists of two components, physical sputtering and ion assisted chemical etching. The chemical etching is proposed to follow the equations:

$$\mathrm{In} + 3\mathrm{CH}* \rightarrow \mathrm{In(CH_3)_3}* \rightarrow \mathrm{In(CH_3)_3(gas)} \tag{6.2}$$

$$\mathrm{P} + 3\mathrm{H}* \rightarrow \mathrm{PH_3}* \rightarrow \mathrm{PH_3(gas)} \tag{6.3}$$

Generally the etching of In was considered as the rate limiting step and preferential etching was observed.

The experimental results show that without ion bombardment, the exclusive use of atom source with CH_4/H_2/Ar chemistry could not etch the surface. According to literature,[99] a polymer forms on the surface and the reaction cannot proceed, ion bombardment was needed to expose the fresh surface for reaction to proceed. Results in Fig. 6.10 show that CAIBE had consistent higher etching rate compared with sputtering below 600 V. This phenomenon has been observed in the literature [129] and it was suggested that incident ion caused CH_4 dissociation close to the InP surface. Because the mean

free path in current experiments was approximately 8 cm, the increased etching rate is unlikely due to CH_4 dissociation in the gas phase. Another possibility was gas back flow. Considering the conductance of ion source and the close etching rate between CAIBE and sputtering after 600 V, the etching rate increase in CAIBE is also not likely due to the backflow of reactive gas into ion source. According to the literature, CH_4 has very low sticking probability on solid surfaces,[51] therefore, the increase of etching rate in CAIBE may due to the incident ions enhanced adsorption of CH_4 on InP surfaces. With increased CH_4 adsorption in CAIBE, the reaction rate is increased.

In RBIBE mode, the incident ions also will increase the sticking probability of CH_4 on InP surfaces. At the same time, the dissociated CH_3 radicals have much higher reactivity compared with CH_4 gas. Therefore, there were no dissociative energy barrier for reactions between In and CH_3, and P with H, compared with the reaction between InP with neutral gas. Therefore, the etching rate in RBIBE mode was improved compared with both sputtering and CAIBE.

From Fig. 6.4, the etching rate in RBIBE mode was stabilized after 5% CH_4. So the reaction was in a CH_4 rich mode. Literature pointed out that when CH_4 concentration is too high, the reaction becomes unstable due to the fast deposition of polymer.[99, 100] In current work, C signal was not detected by XPS after 300 V. Therefore, the deposition of polymer was not the rate limiting step. According to literatures, the $In(CH_3)_3$ and PH_3 have high volatility. Current work with sample temperature shows that from room temperature to 150 °C, the changes of etching rate observed are not obvious, therefore, in current work, product desorption was not the rate limiting step. The etching rate in RBIBE was limited by the incident ion energy and ion flux.

The experimental results show that increased ion energy had strong effect on the etching rate. In Fig. 6.5, with ion energy increased from 200 to 700 V, the etching rate increased from 129 Å/min to 1010 Å/min. The increase of etching rate first is related with the increase of sputtering rate, which changed from 103 Å/min at 200 V to 860 Å/min. However, the ion assisted etching has more complicated relation with ion energy. Since RBIBE combines both pyhsical sputtering and ion assisted chemical etching, in Fig. 6.8, the ratio between RBIBE and sputtering reflectes how much that ion incident contributes

to the chemical etching. The higher ratio suggested that incident ion increases the etching rate more effectively through chemical reaction. The result shows it increases with ion energy to 400 V then dropped at 700 V. Therefore, it suggestes that ion energy below 400 V more effectively improved the chemical reaction but the effect is rather reduced when increased to higher ion energy. According to the literature, the incident ions are playing several important roles in affecting the reaction rate by[99]

- Removing polymer to expose the fresh surface;
- Damaging the surface to imporve the adsorption ability;
- Providing energy for CH_3 migration.

Since no polymer deposition was identified on the surface after 300 V ion energy, the incident ion helps to increase the sticking probability and provide energy. But incident ion can also increase the desorption by interacting with the surface. So the results show that below 600 V, the enhancement of ion incident dominates, but after 600 V, the desorption enhancement by incident ion dominates.

Fig. 6.2 shows that the sputtering yield did not depend on flux. The ion flux increases sputtering rate by increasing the ion density. The ion flux effect in increasing the ethcing rate in RBIBE mode is clearly demonstrated in Fig. 6.7. The increase of etching rate could come from the increased physical etching and also the increased ion assisted etching. Fig. 6.8 demonstrates that below 600 V, the higher incident ion flux increases the efficiency of chemical reaction, because higher ion density could enhance the adsorption and CH_3 migration. But with further increase of ion energy, the enhancement on desorption of incident ion is dominating, therefore, the improvement of chemical etching ratio by ion flux is not obvious. The linear relationship in Fig. 6.7 between ion flux and etching rate suggested that the etching rate may be limited by adsorption.

The function of ion incident further helps to explain the roughness change. The roughness formation of InP during reaction is due to different reaction rate between In and P. The reaction rate of In with CH_3 and P with H were not known. But sputtering of InP

causes P depletion had been well known. Inium islands were observed during sputtering process.[131] Fig. 6.11 shows that chemical reaction reduced roughness because the increased etching rate of In with CH_3 helped the In reduction. Therefore, enhanced chemical reactions were expected to reduce the roughness, RBIBE at 300 V gave the lowest roughness.

6.5 Conclusion

The etching mechanism by CH_4/H_2/Ar chemistry for InP plasma etching was analyzed by an ion beam and an atom beam. Different processes such as sputtering, CAIBE, and RBIBE were tested. The results show that sputtering rate between ion energy 200 eV and 700 eV were at 103 Å/min and 860 Å/min with ion beam source power 200 W and Ar flow rate 5 sccm. The sputtering yield in this energy range did not depend on incident ion flux. A threshold energy approximately 60 V was obtained. The combination of neutral reactive gas with ion bombardment increased etching rate below 600 eV ion energy. After 600 eV, the difference between CAIBE and sputtering was not clear. By using ion beam with inert gas and atom beam with reactive gas, higher etching rate was obtained. With ion source power at 200 W, 5 sccm Ar, atom source power 300 W and 10% CH_4, 20% H_2, etching rate changed from 129 Å/min at 200 V to 1010 Å/min at 700 V. The etching rate was not affected by CH_4 concentration when CH_4 concentration was higher than 5% in the atom beam. The etching rate was not affected by temperature change from room temperature to 150 °C.

The etching rate was both affected effectively by ion energy and ion flux. With ion flux change from 53 μA to 81 μA at ion eneryg at 400 eV, the etching rate increased from 547 Å/min to 818 Å/min. The incident ions believed removed polymer deposition on the surface, which was confirmed by XPS results. The change of etching rate by ion energy and ion flux was contributed to the assistance on CH_4 adsorption and CH_3 migration on the surface. However, the comparison between RBIBE and sputtering shows that when ion energy was higher than 400 eV, the chemical reaction could be reduced by incident ions rather than increased. Changing of H_2 concentration in the atom beam increased

etching rate below 400 V but it was not clear after 400 V. The roughness research shows that higher energy sputtering (600 eV) caused higher roughness, but chemical reaction could effectively reduce the roughness, RBIBE had the lowest roughness.

6.6 Future work

To complement the results presented here, we suggest the following work:

- More accurate calibration of atom flux in sampling location is required, a QCM analysis together with line-of-sight mass spectrometer analysis is useful for detail description of the system;
- Validation of beam reactor results in full plasma etching reactor, the GEC reactor can be used for direct plasma etching with paramters obtained through beam research;
- Investigation of CH_4 adsorption and dissociation on InP surfaces under ion bombardment in a TPD chamber;
- Detailed quantitative AES analysis of preferential etching as a function of ion energy and ion flux will be very useful;
- Investigation of the relationship between surface roughness, ion flux, and ion energy, understand how to increase the etching rate and at the same time without increasing roughness;
- Detailed PIC simulation of CH_4 adsorption and CH_3 migration on InP surfaces.

6.7 Figures

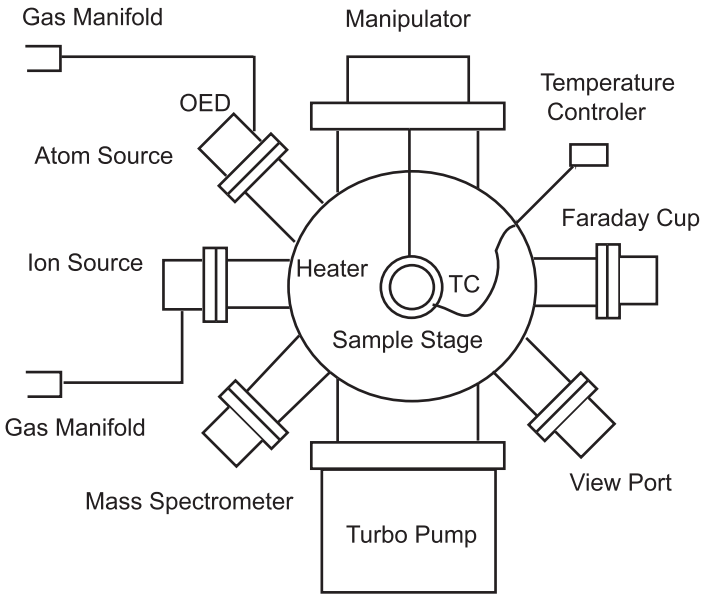

Figure 6.1: Schematic of experimental system showing: atom source, ion source, Faraday Cup, sample stage with heater and thermocouple (TC), temperature controler, manipulator, mass sepctrometer, gas manifold.

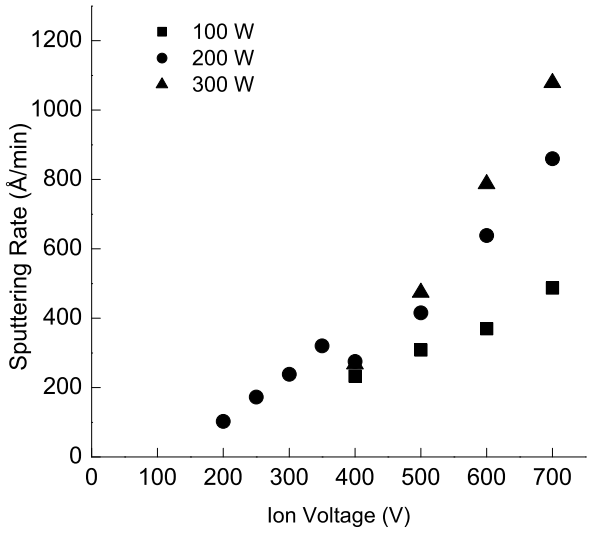

Figure 6.2: Sputtering Rate with ion source power at 200 W, 5 sccm Ar, 200 V to 700 V, and sputtering rate with ion source power at 100, 300 W, 5 sccm Ar, 400 V to 700 V.

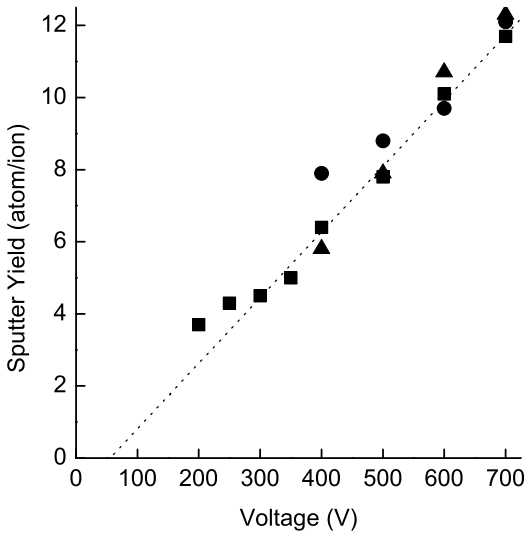

Figure 6.3: Sputtering yield change with ion voltage. Preferential sputtering affect was neglected. The dash line was the linear fit of ion source power 200 W, 5 sccm Ar, ion energy from 200 to 700 V.

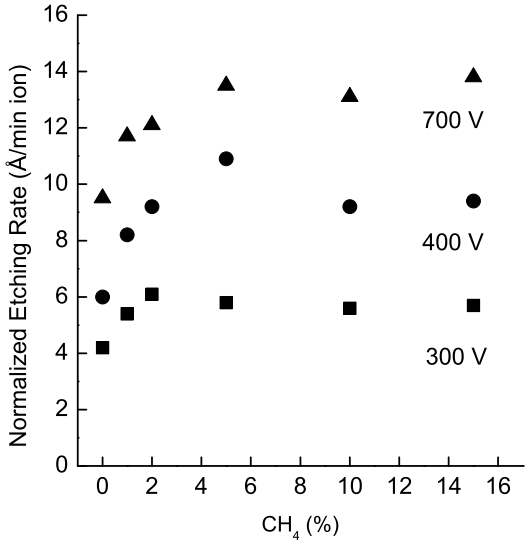

Figure 6.4: Etching rate change with CH_4 concentration in atom beam in RBIBE mode, H concentration was 20%, atom beam source power at 300 W. The ion beam source power was 200 W, for three different incident ion energy 300, 400, and 700 V.

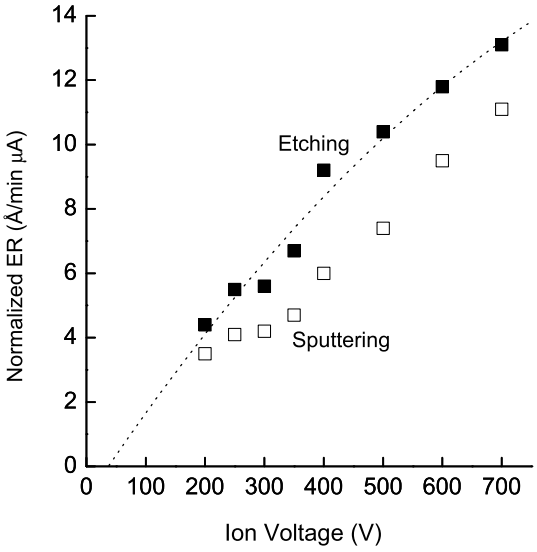

Figure 6.5: The normalized etching rate (■) change with ion voltage in RBIBE mode, 10% CH_4, 20% H_2 for atom beam, source power 200 W. Ion source power was 200 W, Ar flow rate 5 sccm. Normalized sputtering rates were plotted for comparison (□).

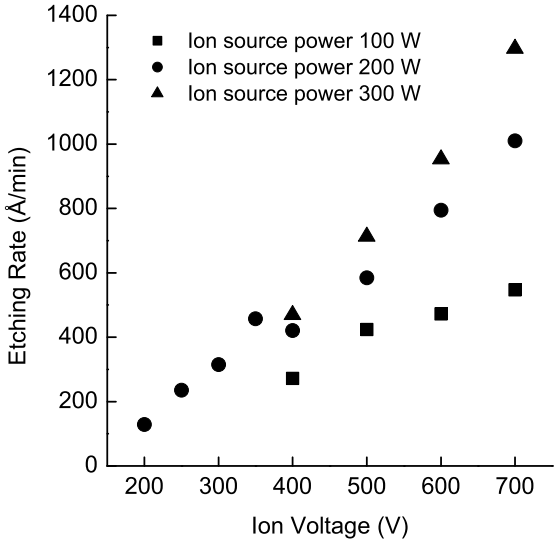

Figure 6.6: Etching rate change with incident ion energy and ion flux in RBIBE. Ion voltage 200 to 700 V for 200 W source power, 400 to 700 V at 100 and 300 W source power. The atom source power was 300 W, 5 sccm total flow rate, 10% CH_4, 20% H_2, 70% Ar

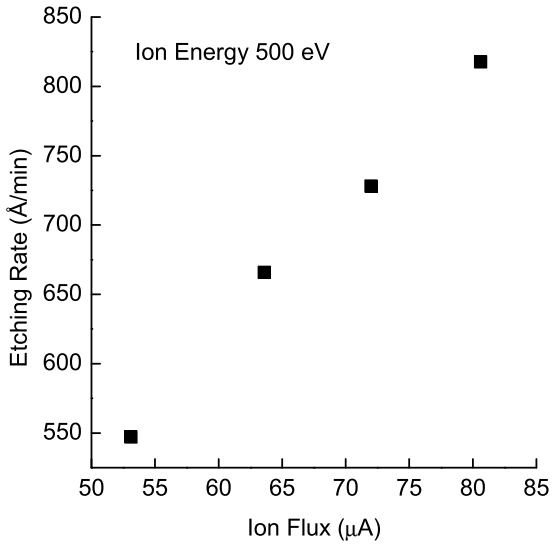

Figure 6.7: Etching rate change with ion flux in RBIBE. The atom source power at 300 W, 10% CH_4, 20% H_2. The ion source power at 200 W, ion energy 400 eV, 5 sccm Ar.

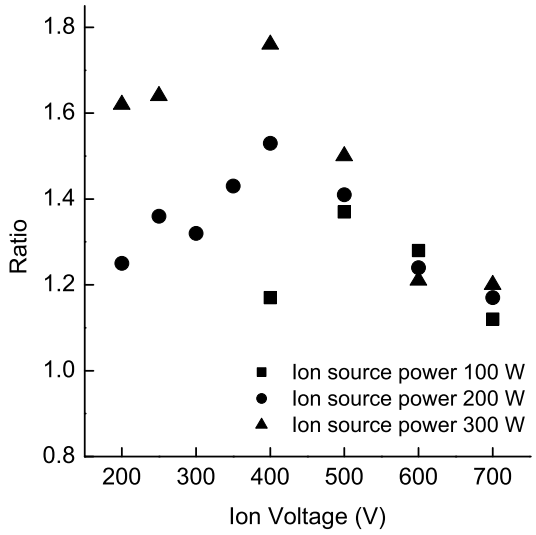

Figure 6.8: The ratio of etching rate by RBIBE with etching rate by sputtering with ion source power 100 to 300 W, ion energy 200 to 700 V. In RBIBE, the atom source power was 300 W, 10% CH_4, 20% H_2.

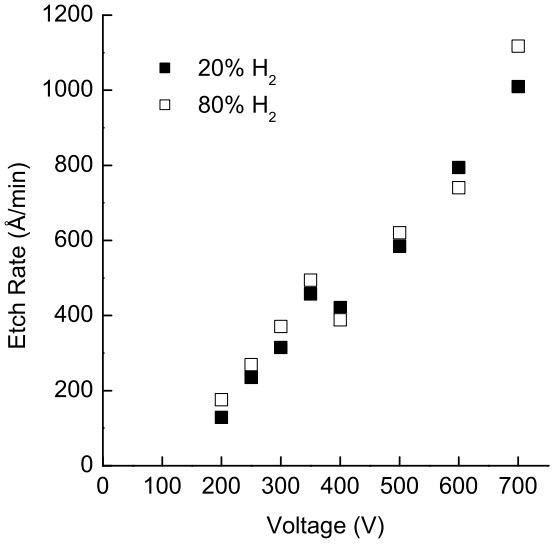

Figure 6.9: Etching rate change with different ion voltage at 20% and 80% H_2 in RBIBE. Atom source power at 300 W, 10% CH_4. Ion source power 200 W, 5 sccm Ar.

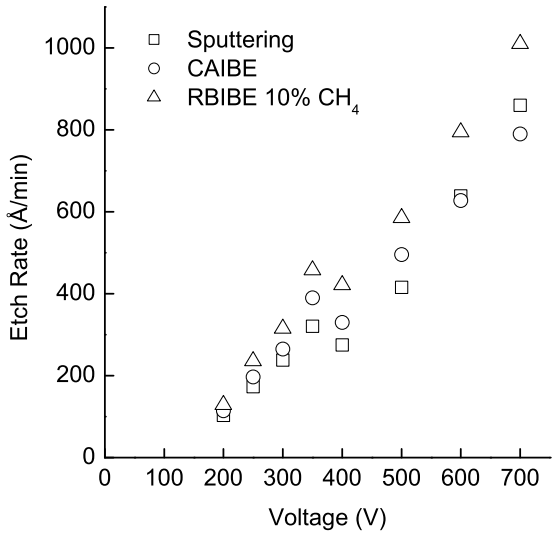

Figure 6.10: Comparison of sputtering, CAIBE, and RBIBE from ion energy 200 to 700 V. Sputtering: ion source power 200 W 5 sccm Ar; CAIBE: ion source power 200 W, 5 sccm Ar, reactive gas in as 10% CH_4, 20% H_2, and 70% Ar; RBIBE: ion source power 200 W, 5 sccm Ar, atom source power 300 W, 10% CH_4, 20% H_2, and 70% Ar.

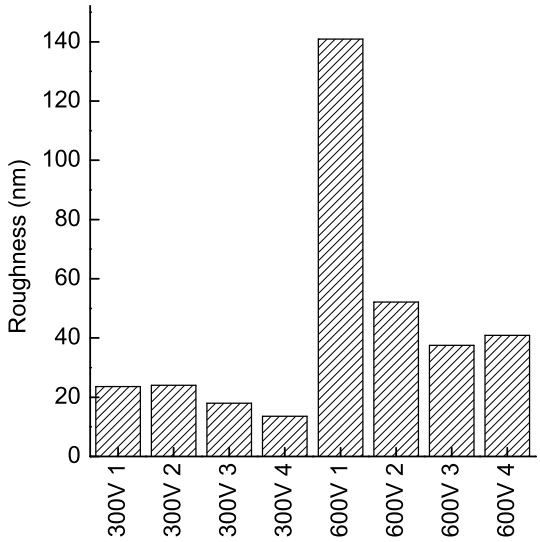

Figure 6.11: Roughness comparison at ion energy 300 and 600 eV for 4 different process conditions. 1. Sputtering: ion source power 200 W, 5 sccm Ar; 2. CAIBE, ion source power 200 W, 5 sccm Ar, reactive gas 10% CH_4, 20% H_2, and 70% Ar; 3. RBIBE, ion source power 200 W, 5 sccm Ar, atom source power 300 W, 10% CH_4, 20% H_2, and 70% Ar; 4. RBIBE, ion source power 200 W, 5 sccm Ar, atom source power 300 W, 10% CH_4, 80% H_2, and 10% Ar.

CHAPTER 7

Conclusions

To analyze a plasma etching process, it is important to understand the reactions both in the gas phase and on the gas-solid interface. In this research, the analysis of plasma etching process has been divided into three tasks to simplify the complicated etching system and still obtain a general and systematical understanding. Through tasks that focused on gas phase physics, chemical reactions and ion assisted chemical reactions on the interface, improved understanding of plasma etching are obtained.

In task 1, the change of electro-physical properties of the plasma with gas addition was investigated. Hydrogen and nitrogen were added into a capactively coupled Ar plasma and their effect on electro-physical properties as investigated in detail. The system was more sensitive to N_2 concentration than to H_2 concentration. When both H_2 and N_2 were added into the system, the electro-physical properties were dominated by N_2. The transparency effect of H_2 addition and the electronegativity with N_2 addition were considered as the reasons behind these phenomena. Through those factors, the ratio between ohmic heating and stochastic heating was modified, which caused the change of electro-physical properties. The results suggest that for general plasma systems, gas addition can have a strong effect on electro-physical properties, transparency effect and electronegativity are important for plasma properties and need to be considered for the process.

The task 2 focused on the understanding of plasma based surface reactions. A H_2 atom beam was used to remove silanol groups from *p*-MSQ films. H atom reacted with silanol groups and the product water could be removed through substrate heating. By changing substrate temperature, H atom flux, and process time, the film loss could be minimized with silanol groups removed. It improves our understanding in plasma reactions control without ion interaction and provided a practical method for *p*-MSQ film process in manufacturing line.

In task 3, $CH_4/H_2/Ar$ plasma etching of InP was investigated by an ion beam and an

atom beam in a beam reactor system. The combination of ion beam and atom beam gave closer approximation of plasma etching, at the same time, it provided individual control of ion and atom properties to simplify the mechanism analysis. A systematic analysis of ion energy, ion flux, and atom flux suggested that the adsorption was the rate limiting step. The analysis of ion energy effect in etching rate showed that low energy ion incidence increased but high energy ion incidence weakened the chemical reactions on InP surface. The ion energy was optimized approximately at 400 eV in current system. At low ion energy, ion flux effect was stronger on chemical reactions compared with the effect at higher ion energy. Through this research, for general plasma etching system, it suggestes that for an adsorption controlled plasma etching, depends on the energy and flux, the incident ions can have very different effect in chemical reactions.

Through these three tasks, plasma etching process was analyzed in both gas phase and gas-solid interface, a completed picture of plasma etching was obtained. The results not only improved the understanding on current specific subjects, but also are useful for understanding of general plasma etching systems. Future work has been propsed in order to further improve the understanding of the observed phenomena and apply our knowledge to practical applications.

APPENDIX A

A.1 Abbreviations and Symbols

EEDF: electron energy distribution function

EEPF: electron energy probability function

GEC: gas electronic conference

p-MSQ: porous-methylsilsesquioxane

FTIR: Fourier transform infrared

RF: radio frequency

ICP: inductively coupled plasma

CAIBE: chemically assisted ion beam etching

RIBE: reactive ion beam etching

RBIBE: reactive beam ion beam assisted etching

OED: optical emission detector

OML: orbital motion limited

FC: Faraday cup

CVD: chemical vapor deposition

PECVD: plasma enhanced chemical vapor deposition

HSQ: hydrogen silsequioxane

UV: ultra-violet

TC: thermalcouple

XPS: x-ray photospectroscopy

AFM: atomic force microscopy

V_B: probe bias

V_p: plasma potential

V_f: floating potential

kT_e: electron temperature or average electron kinetic energy

kT_i: ion temperature or average ion kinetic energy

n_e: electron density

n_i: ion density

$g_e(\epsilon)$: EEDF

$g_p(\epsilon)$: EEPF

χ: Laframboise theory scaling factor

R_p: probe radius

A_p: probe collecting area

e: electron charge

Z: atom number

a: Lindhard screening radius

a_0: Bohr radius

U(R): interaction potential

e: elementary charge

$e^{'}$: electron charge

E_0: hydrogen atom base energy

Y(E): sputtering yield function

$S_n(E)$: nuclear stopping cross section or nuclear stopping power

M_1: incident ion mass

M_2: target atom mass

$s_n(\epsilon)$: reduced stopping power

ϵ: reduced energy

U_0: surface binding energy

E_B: surface binding energy

Q: yield factor

Y_N: normalized yield

Y_i^c: component i sputtering yield

n_A: sputtered component A atom number

c_A: bulk concentration of A

c_A^s: surface concentration of A

A.2 Brief Description of Boltzman Equation

A.2.1 Boltzman equation and EEDF

The EEDF for a weakly ionized plasma can be obtained by solving Boltzman equation (Slova equation) directly. The Boltzman equation is defined as follows [28]

$$\frac{\partial f}{\partial t} + \bar{v} \bullet \nabla_{\bar{r}} f + \frac{\bar{F}}{m} \bullet \nabla_{\bar{v}} f = \left(\frac{\partial f}{\partial t}\right)_c \tag{A.1}$$

where $f(\bar{v}, \bar{r}, t)$ is the distribution function for electrons in six dimensions of both velocity space and space position. The $\bar{F}$ is the field force,for an electric field it can be expressed as $\mathrm{e}\bar{\mathrm{E}}/\mathrm{m}$. $(\partial f/\partial t)_c$ is the collision term which includes different collision types for electrons inside the plasma.

When consider one dimension space position, this equation can be simplified as

$$\frac{\partial f}{\partial t} = -v_x \frac{\partial f}{\partial x} - \frac{e}{m}\frac{\partial f}{\partial v_z} + \left(\frac{\partial f}{\partial t}\right)_{coll} \tag{A.2}$$

If only consider the velocity space, then this equation can be expressed as

$$\frac{\partial f}{\partial t} = -\frac{e}{m}\bar{E} \bullet \nabla_v f + \left(\frac{\partial f}{\partial t}\right)_s \tag{A.3}$$

where now f is only a function of $f(\bar{v}, t)$.

The Boltzman equation has been attempted both analytically and numerically. To obtain a analytical form, certain assumptions and simplifications must be made.[132, 133] If electrons move in an electric field and interact strongly, the EEDF is expressed by a Maxwellian distribution

$$N(v)dv = \frac{4N_e}{\sqrt{\pi}}\left(\frac{v}{v_m}\right)^2 e^{-(v/v_m)^2} d\frac{v}{v_m} \tag{A.4}$$

if define $\epsilon = mv^2/2$ and $\epsilon_m = mv^2/2 = kT_e$, then the distribution function can be expressed as

$$N(\epsilon)d\epsilon = \frac{2N_e}{\sqrt{\pi}}\left[\left(\frac{\epsilon}{\epsilon_m}\right)^{\frac{1}{2}} e^{-\epsilon/\epsilon_m} d\left(\frac{\epsilon}{\epsilon_m}\right)\right] \tag{A.5}$$

If electrons move in a weak electric field, suffering elastic collisions only and drawing energy from the field without exchanging it with other electrons, then the EEDF is

expressed as a Druyveysteyn distribution.[27]

$$N(\epsilon)d\epsilon = \frac{2}{\Gamma\left(\frac{3}{4}\right)} N_e \left[\left(\frac{\epsilon}{\epsilon_m} \right)^{\frac{1}{2}} e^{-0.55\left(\frac{\epsilon}{\epsilon_0}\right)^2} d\left(\frac{\epsilon}{\epsilon_0} \right) \right] \tag{A.6}$$

With the development of numerical analysis method and the increase of computation power, different numerical methods were developed and many different works were done.[28] Generally, the numerical methods of solving Boltzman equation need MC(Montre-Carlo) or PIC (particle in cell) methods.

A.2.2 EEDF Measurement by Langmuir Probe Based on Druyvesteyn Method

More frequently, EEDF is obtained by Langmuir probe measurement. The common process is based on Druyvesteyn method. For its importancy, the illustration by Lieberman *et al.* was illustrated and explained in following section.[28]

Suppose an arbitrary distribution function $f(\bar{v})$, the electron current to the planar probe in retarding potential region $\Phi_p - V_B > 0$ ($\Phi_p$is the plasma potential, V_B is the probe bias)can be written as

$$I_e = eA \int_{-\infty}^{\infty} dv_x \int_{-\infty}^{\infty} dv_y \int_{v_{min}}^{\infty} dv_z v_z f_e(\bar{v}) \tag{A.7}$$

This is simply the integration of electron thermal flux that arrives on the plane, A is probe collection area. Plane edge effect has been neglected. The v_{min} is defined by

$$v_{min} = \left[\frac{2e(\Phi_p - V_B)}{m} \right]^{1/2} \tag{A.8}$$

v_{min} correponds to the minimum kinetic energy required for the electrons to overcome the potential barrier across the sheath region. A spherical polar coordinates in velocity can be introduced by assuming an isotropic distribution based on Druvyvesteyn assumption.[]

$$I_e = eA \int_{v_{min}}^{\infty} dv \int_0^{\theta} d\theta \int_0^{2\phi} d\phi v \cos(\theta) v^2 \sin(\theta) f_e(v) \tag{A.9}$$

where

$$\theta_{min} = \arccos\left(\frac{v_{min}}{v} \right) \tag{A.10}$$

This easily leads to

$$I_e = \pi e A \int_{v_{min}}^{\infty} dv v^3 \left(1 - \frac{v_{min}}{v^2}\right) f_e(v) \tag{A.11}$$

or

$$I_e = \frac{\pi e A}{2} \int_{v_{min}}^{\infty} dv^2 v^2 \left(1 - \frac{v_{min}}{v^2}\right) f_e(v) \tag{A.12}$$

for convenience in following transformation.

By introducing $V = \Phi_p - V_B$ (voltage difference between plasma potential and probe bias) and $\varepsilon = \frac{1}{2} m v^2 / e$, the above equation easily changes to

$$I_e = \frac{2\pi e^3}{m^2} A \int_V^{\infty} \varepsilon \left\{ \left(1 - \frac{V}{\varepsilon}\right) f_e[v(\varepsilon)] \right\} d\varepsilon \tag{A.13}$$

note now $v(\varepsilon) = (2e\varepsilon/m)^{1/2}$.

Using the following transformation

$$\text{if} \quad G = \int_{x_1}^{x_2} g(x_1, x) dx \quad \text{then} \quad \partial G / \partial x_1 = \int_{x_1}^{x_2} \left(\partial g / \partial x_1\right) dx - g\left(x_1, x_1\right) \tag{A.14}$$

and let $x = \varepsilon$, $x_1 = V$, $x_2 = \infty$, then $g\left(x_1, x\right) = \varepsilon \left\{ \left(1 - \frac{V}{\varepsilon}\right) f_e[v(\varepsilon)] \right\}$. Now $\partial \varepsilon / \partial V = 0$, and $\partial \left\{ V f_e[v(\varepsilon)] \right\} / \partial V = f_e[v(\varepsilon)]$. The differetiation of I_e over V is

$$\frac{dI_e}{dV} = -\frac{2\pi e^3}{m^2} A \int_V^{\infty} f_e[v(\varepsilon)] d\varepsilon \tag{A.15}$$

Use the transformation one more time for second differentiation, it yields

$$\frac{d^2 I_e}{dV^2} = \frac{2\pi e^3}{m^2} A f_e[v(V)] \tag{A.16}$$

The electron energy distribution function is defined as $g_e(\varepsilon)$ with respect to kinetic energy

$$g_e(\varepsilon) d\varepsilon = 4\pi v^2 f_e(v) dv \tag{A.17}$$

note $v(\varepsilon) = (2e\varepsilon/m)^{1/2}$ then

$$g_e(\varepsilon) = 2\pi \left(\frac{2e}{m}\right)^{3/2} \varepsilon^{1/2} f_e[v(\varepsilon)] \tag{A.18}$$

Since $e\Phi = m v^2 / 2$, let $\varepsilon = V$, then

$$g_e(V) = 2\pi \left(\frac{2e}{m}\right)^{3/2} \varepsilon^{1/2} f_e[v(V)] \tag{A.19}$$

Use the result above (eqA.16) for $f_e[v(V)]$, then

$$g_e(V) = \frac{2m}{e^2 A}\left(\frac{2eV}{m}\right)^{1/2}\frac{d^2 I_e}{dV^2} \tag{A.20}$$

Therefore, EEDF with respect to V can be obtained from the $I-V$ curve and V stands for the electron kinetic energy.

The electron energy probability function (EEPF) is defined as

$$g_p(\varepsilon) = \varepsilon^{-1/2} g_e(\varepsilon) \tag{A.21}$$

If electrons have a Maxwellian distribution, then $g_e(\varepsilon)$ is defined as

$$g_e(\varepsilon) = 2\pi n_e \left(\frac{1}{\pi k T_e}\right)\varepsilon^{1/2} e^{\left(\frac{-\varepsilon}{kT_e}\right)} \tag{A.22}$$

by the definition of $g_p(\varepsilon)$

$$g_p(\varepsilon) = \frac{2}{\sqrt{\pi}} n_e k T_e^{-3/2} e^{-\varepsilon/kT_e} \tag{A.23}$$

For a given plasma system, then $\ln g_p$ is linear with ε. Therefore, the plot of EEPF for a Maxwellian distribution in a semi-log coordinate will give a straight line. For this reason, $g_p(\varepsilon)$ (EEPF) rather than $g_e(\varepsilon)$ (EEDF) is more often used in literature to present experimental results.

A.3 An Introduction to Sputtering Process

A.3.1 Description of Sputtering Mechanism

Sputtering is a phenomenon involving the ejection of material from solid surfaces under bombardment by energetic ions (or neutrals). The sputtering process causes the erosion of the target surfaces. If a substrate is located near the target, the atoms fly away from the target, forming a film on the substrate. In this case, sputtering involves two separate actions: an erosion process for the target and a deposition process for the substrate. The mechanisms of target erosion during the sputtering process fall into two categories, physical sputtering and chemical sputtering. For chemical sputtering, chemical reactions are involved during the sputtering process. For physical sputtering, inert gases are used to

generate ions, and no chemical reactions are involved, only the transfer of kinetic energy. The physical sputtering processes can happen in two different situations. One condition is called knock on sputtering, which is the focus of the discussion in this brief review. For another situation, electronic excitation is involved. Detailed description of sputtering is found in publications.[6]

Knock on sputtering is based on an atomic collision cascade wherein the incident ion knocks atoms off of their equillibrium sites in the target, thus causing these atoms to move through the material, to undergo further collisions, and eventually to cause the ejection of atoms through the target surface. The possible collision processes that occur under ion bombardment are illustrated in Fig. A.1.[5]

The collision processes for knock on sputtering that are illustrated in figure A.1 can be further divided into three qualitatively different situations based on the condition of recoiled atoms that are caused by ion incident.[6] These three situations are single-knock on regime, linear cascade regime, and spike regime. They are illustrated in Fig. A.2. In single-knock on regime, the recoil atoms are sputtered from the target but they are not strong enough to generate recoil cascade in the target. The incident ion energy is usually in the range of eV to lower keV. In linear cascade regime, recoil atoms have sufficient energy to cause further cascading of atoms in the target, but the density of these recoil atoms is low. Lacking sufficient density, the incidence of collision frequency between those atoms that move in the target is low. The incident ion energy usually is in the range of tens of keV to hundreds of keV or MeV. In spike regime, similar to linear cascade, the recoiled atoms caused by ion target collision generate multiple recoils. But in this regime, the density of recoil atoms is high and the majority of atoms in a certain volume in the target are moving. Therefore, the collision frequency among these atoms is higher compared to the linear cascade regime.

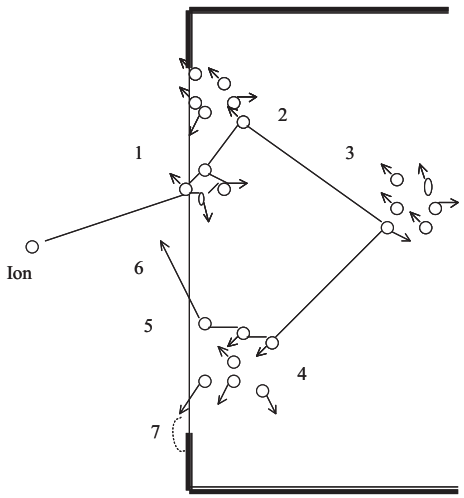

Figure A.1: Schematic of possible collision processes caused by incident ions during sputtering, reproduced from literature.[5](1) Surface atom receive energy and after several collisions is reflected away from the target; (2) the incoming ion creates a primary recoil which in turn produces a collision cascade that penetrates in surfaces; (3) collision cascade which does not penetrate the surface; (4) reflected ion creates a cascade which penetrates the surface; (5) reflected ion gives energy to a surface atom which is sputtered; (6) ion reflected into the vacuum with kinetic energy; and (7) atom with momentum component directed away from the surface returns because of attractive forces.

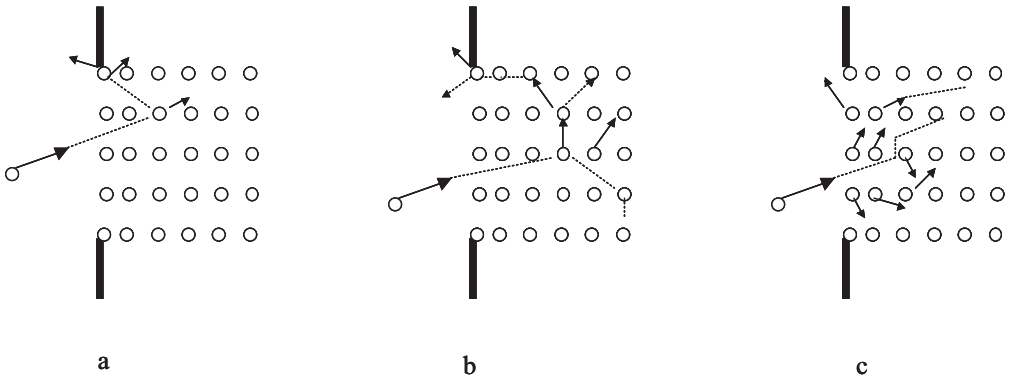

Figure A.2: Three regimes of sputtering by elastic collisions. (a) The single-knock on regime. (b) The linear cascade regime. (c) The spike regime. Reproduced from literature.[6]

The erosion rates of the target during the sputtering process are characterized primarily by the sputtering yield Y which is defined as the mean number of emitted atoms per incident particles.[134] It is one of the most important parameters for the sputtering process. It relates to ion incident angle, energy, and target properties such as target atom mass, crystalline structure, surface binding energy and so on. Many experiment and theoretical works have been done in predicting and measuring the sputtering yield for different incident ion energy ranges and ion-target combinations. In the following section, the theoretical equations for calculating the sputtering yield under normal ion incident are presented.

A.3.2 Yield calculation for normal ion incident

In the theoretical calculation of sputtering yield, two basic assumptions were made. One assumption was the binary collision process in which the process of interaction during collision was demonstrated using two atoms, even though there might be multiple atoms colliding. This assumption was proved to be a good approximation both theoretically and experimentally. The second assumption involved the calculation of the interaction potentials based on the Thomas-Feri approach. It means that the potential took the same form as

$$V(r) = \frac{Ze^2}{r}\phi\left(\frac{r}{a}\right) \tag{A.24}$$

In theoretical analysis, this potential was assumed as

$$U(R) = \frac{Z_1 Z_2 e^2}{R}\phi\left(\frac{R}{a}\right) \tag{A.25}$$

where Z was the atom number, the subfix 1, 2 represented the incident ion and target atom, note e^2 was elementary charge and was defined as $\mathrm{e} = \mathrm{e}'/4\pi\varepsilon_0$ and $\mathrm{e}^2 = 14.39\mathrm{eV\AA}$, where e' is electron charge. The a was called accelerationing radius and was obtained by [5]

$$a = 0.8853a_0\left[Z_1^{2/3} + Z_2^{2/3}\right]^{-1/2} \tag{A.26}$$

a_0 is Bohr radius defined by $\pi \mathrm{a}_0^2 = 8.82 \times 10^{-17}$ cm^2 $\mathrm{a}_0 = 0.529$ Å. For a_0, e^2 and E_0 it is

$$E_0 = \frac{-\mu e^4}{8h^2\varepsilon_0^2} = -13.598eV = \frac{e^2}{2a_0} \tag{A.27}$$

and E_0 is the hydrogen atom base energy.

The yield equation from theoretical analysis was given as:[5, 135]

$$Y(E) = 0.042\alpha \frac{S_n(E)}{U_0} \tag{A.28}$$

For this equation, U_0 was surface binding energy and the unit was in eV. And eV was defined by $1\mathrm{eV} = 1.6 \times 10^{-19}\mathrm{C} \times 1\mathrm{J/C} = 1.6 \times 10^{-19}\mathrm{J}$

In Eq. A.28, α is a dimensionless quantity depending on the relative masses and the angles of incidence and can be checked in references.[5] The S_n(E) was defined by Sigmund as the nuclear stopping cross section, sometimes called nuclear stopping power, which is one of the basic input quantities and can be expressed by

$$S_n(E) = \frac{C}{1-m}\left[\frac{4M_1M_2}{(M_1+M_2)}\right]^{1-m} E^{1-2m} \tag{A.29}$$

where M is mass, and γ is $\gamma = 4M_1M_2/\left(M_1+M_2\right)^2$ m is a coefficient and changes from 0 to 1 depends on incident ion energy. C is a coefficient decided by

$$C = \frac{1}{2}\pi\lambda_m a^2 \left(\frac{M_1}{M_2}\right)^m \left(\frac{2Z_1Z_2e^2}{a}\right)^{2m} \tag{A.30}$$

λ_m is a dimensionless function depends on m, some values were given in literatures.[6] For keV energy and heavy-to-medium masss ions, the nuclear stopping power is modified as

$$S_n(E) = 4\pi a Z_1 Z_2 e^2 \frac{M_1}{M_1+M_2} s_n(\varepsilon) \tag{A.31}$$

where $s_n(\varepsilon)$ is called reduced stopping power and was defined by

$$s_n(\varepsilon) = \frac{3.441\sqrt{\varepsilon}\ln\varepsilon + 2.718}{1.6.35\sqrt{\varepsilon} + \varepsilon(-1.708 + 6.882\sqrt{\varepsilon})} \tag{A.32}$$

ε is called reduced energy and is defined by

$$\varepsilon = \frac{M_2E}{M_1+M_2} \bullet \frac{a}{Z_1Z_2e^2} \tag{A.33}$$

Therefore the yield equation for linear cascade for heavy to medium ion target atom mass is

$$Y(E) = 3.56\alpha \frac{Z_1Z_2}{\left[Z_1^{2/3}+Z_1^{2/3}\right]^{1/2}} \frac{M_1}{[M_1+M_2]} \frac{s_n(\varepsilon)}{U_0}; \tag{A.34}$$

The detail deduction of the process was available in literatures.[6, 5]

The application of this equation can be illustrated by an Ar sputtering of Cu for 45keV. Using the equation A.34 the calculation shows that for $\mathrm{Z_1} = 18, \mathrm{Z_2} = 29, \mathrm{M_1} = 40\mathrm{g/mol}, \mathrm{M_2} = 64\mathrm{g/mol}, \mathrm{U_0} = 3.46\mathrm{eV}, \mathrm{E} = 45\mathrm{keV}$ Then $\mathrm{M_2/M_1} = 1.6$, checked graph $\alpha = 0.34$, and acceleration radius $\mathrm{a} = 0.116$ Å, $\varepsilon = 0.428$, the $\mathrm{s_m}(\varepsilon)$ could be obtained through reference or by equation A.32 and obtained $\mathrm{s_n}(\varepsilon) = 0.41$. By applying equation A.34 obtained $\mathrm{Y(E)} = 0.71$, the experimental data shows a sputtering yield of 0.67, which is close to the theoretical result.

A.3.3 Low energy sputtering yield calculation in Normal incident

For low energy range where $E \leq 1keV$, equation A.28 can be modified as

$$Y(E) = \frac{3}{4\pi^2}\alpha\frac{4M_1M_2}{(M_1+M_2)^2}\frac{E}{U_0} \quad E \leq 1keV \tag{A.35}$$

The experimental results showed that this theoretical calculation resulted in relatively large error when applied to low energy situations, especially for energy levels close to threshold energy, or for light ions such as Hydrogen or Helium ions.[136] For improvement, Bohdansky suggested that the yield could still be expressed as:[137]

$$Y = QY_N(K, E) \tag{A.36}$$

where $\mathrm{Y_N}$ was normalized yield, Q was yield factor. For $\mathrm{M_1/M_2} < 1$ the sputtering yield was expressed as

$$Y = \left(6.4 \times 10^{-3}\right) M_2\gamma^{5/3}E^{1/4}\left(1 - E'^{-1}\right)^{7/2} \quad E' = E/E_{th} \tag{A.37}$$

The threshold voltage could be estimated by

$$E_{th} = E_B/\gamma(1-\gamma) \qquad M_1/M_2 \leq 0.3 \tag{A.38}$$

$$= E_B 8\left(M_1/M_2\right)^{\frac{5}{2}} \qquad M_1/M_2 > 0.3 \tag{A.39}$$

if experimental measurements were not available. The $\mathrm{E_B}$ is the surface binding energy as $\mathrm{U_0}$ in formal discussion.

For more general conditions where $\mathrm{M_1/M_2} < 1$ was not satisfied, Bohdansky proposed that the low energy sputtering yield could be directly obtained by modifying the equation A.28.[138] A new nuclear stopping power $\mathrm{S_n^*(E)}$ was defined as

$$S_n^*(E) = S_n(E)\left[1 - (E_{th}/E)^{1-m}\right] \tag{A.40}$$

by assuming a cosine distribution for desorption, the equation for general low energy sputtering was expressed as

$$Y(E) = \frac{0.042}{U_0}\left(R_p/R\right)\alpha S_n(E)\left[1 - (E_{th}/E)^{\frac{2}{3}}\right]\left[1 - (E_{th}/E)\right]^2 \tag{A.41}$$

E_{th} was obtained as equations above, and

$$R/R_p = K\frac{M_2}{M_1} + 1 \quad K = 0.4 \quad \text{when} \quad 0.5 < \frac{M_2}{M_1} < 10 \tag{A.42}$$

the coefficient of α is defined by $\alpha = 0.3\left(\mathrm{M_2/M_1}\right)^{\frac{2}{3}}$.

Eq. A.41 can be illustrated by following calculation. For example, as Ar sputtering Cu at 200eV, by Eq. A.37 the $\mathrm{M_1/M_2} = 0.625$, the $\mathrm{E_{th}}$ is 8.548eV, $\mathrm{R/R_p} = \mathrm{KM_2/M_1} + 1 = 1.64$, and $\alpha = 0.3\left(\mathrm{M_2/M_1}\right)^{2/3} = 0.41$, and $\varepsilon = 0.0019$ by equation A.33, therefore, the calculation gave $\mathrm{s_n}(\varepsilon) = 0.118$ and $\mathrm{S_n(E)} = 496.69$, the sputtering yield of Y(E) is 1.21, close to measured value around 1.5.

In current research, the single knock-on regime was expected in the interested energy range. In this regime, the particles which are ejected during ion bombardment originate from the first layer or layers very close to the top. The surface atoms are assumed to be ejected by either interaction with the primary ion or by collision with upward moving atoms from below the first layer. The sputtering yield calculation was based on low energy sputtering process.

A.3.4 Preferential sputtering

When a target has more than one element during sputtering process, the different components may not be sputtered in proportion to their original composition in the target. This phenomenon is called preferential sputtering. The target surface composition change depends on ion mass, ion energy, target temperature, and ion fluence. Preferential sputtering

forms an altered layer on the target. This layer has a different composition than the bulk target. When a steady state is reached, if the temperature is low enough so that the thermal diffusion from the bulk target to the altered layer can be neglected, the sputtered atoms will be of the same composition as it in the bulk target based on mass balance restriction. However, the formed altered layer will principally have a different composition than the bulk target. It is also very common for this layer to have a different surface morphology compared with the original surface.[139]

Experimental results generally showed that the sputtering yield for components are different from the yield that would be produced from a pure state. The interaction between components certainly plays an important role in affecting the sputtering yield. The detail analysis of preferential sputtering mechanisms is rather complicated, but qualitatively two factors are considered the most important: the mass difference and the surface binding energy or chemical bonding energy difference.[140, 139]

During a collision cascade process, the momentum and energy distribution will not be uniform for atoms with different masses. Therefore, different ejection probabilities are expected for different atoms. Generally this results in more effective removal of light atoms and the enrichment of heavy atoms on the target. Components with a lower surface binding energy will be preferentially sputtered and cause the enrichment of higher surface binding energy components. For compounds, the different chemical bonding energy will also affect the process since it is necessary for chemical bonds to be broken for the atoms to leave the target.

For theoretical calculation, due to the multicomponent situation, different yield definitions were introduced.[139] The partial sputtering yield $\mathrm{Y_i}$ is defined as the average number of sputtered atoms of component *i* per incident ion. The total sputtering yield *Y* is defined as the average number of sputtered atoms per incident particle. The relationship for them are

$$Y = \sum_i Y_i \tag{A.43}$$

The component sputtering yield $\mathrm{Y_i^c}$ is defined by

$$Y_i^c = Y_i / c_i^s \tag{A.44}$$

where c_i^s is the equilibrium surface concentration.

Since at the steady state, the sputtered atoms must balance to the bulk concentration, therefore

$$n_A/n_B = c_A/c_B \tag{A.45}$$

where A, B stands for the components, n is the number of sputtered atoms, c is the bulk concentration.

Combining the above equations, an expression was obtained as

$$Y_A^c/Y_B^c = (c_A/c_B) \,/\, (c_A^s/c_B^s) \tag{A.46}$$

By this equation, through the measurement of surface concentration and bulk concentration, the surface sputtering yield can be obtained and the difficult process of measuring yield directly may be avoided.

A.3.5 The Calculation for InP

InP is a binary semiconductor with a mass ratio 115/31. The bond energy for In-P is 2.05 eV, the surface binding energy for In is 2.52 eV, for P is 3.44 eV.[131] Therefore, preferential sputtering was expected. Malherbe *et al.* used AES measured the preferential sputtering for normal incident and calculated theoretically. It formed a surface layer with $c_p^s/c_{In}^s = 0.8$.

Fig. A.3 shows the calculated and measured sputtering yield of InP. The theoretical calculation was based on Eq. A.37. For the measurement, the sputtered thickness was converted to atom number with atom density was used for the calculation. The experimental results are converted from etched thickness with atom density 3.96×10^{22}/cm^3 and assumed In:P as 1:1. The difference between theoretical calculation and experimental measurement may originate from the preferential etching effect.

the preferential sputtering factor on the modified layer was predicted by Malherbe *et al.* as $P/In = 0.72$ for normal incident and the results were compared with AES research.[131]

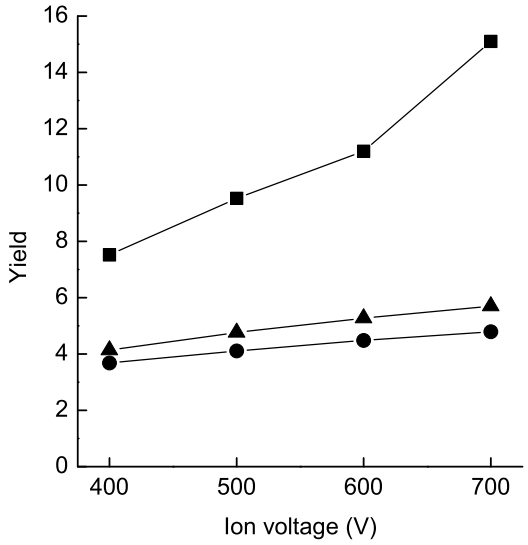

Figure A.3: The comparison of yield between theoretical calculation and experimental measurement. The ■ for experimental measurement. In theoretical calculation ○ for Y_{In} and △ for Y_P, □ for Y_{InP}=Y_{In}+Y_P.

A.4 Literature Comparison of InP Etching

Table A.1: Comparison of etching rate InP etching by CH_4/H_2/Ar plasma etching with different parameters

React	Power	Sub Volt	CH_4	H_2	Ar	mTorr	Å/min	Sub T(°C)	Ref
Cap	0.59 /cm^2	270	9.7	90.3	0	90	620	80	[99]
Cap	0.45 /cm^2	435	2.5 9.7	30-	0	50	230 380	NA	[100]
Cap	100 W	190 335	10	80	0	10 200	650	NA	[104]
Cap	150 W	200	6	20	10	10	123	100	[103]
ICP	150 W	30	2	20	10	30	710	100	[103]
ICP	500 W	400	5	10	5	5	5	NA	[108]
ECR	250 W	100	5	15	7	1	250	NA	[106]
ECR	600 W	125	2	18	25	1.5	3000	NA	[107]
ECR	80 W	120	2.8	18	8	2	NA	NA	[105]
ECR	1000 W	300 W	40	25	10	30	720	27	[141]

Table A.2: References summary for beam technologies in InP etching

Beam	Chemistry	Parameters	Results (ER:Å/min)	Ref
CAIBE	Cl_2,CH_3I,IBr_3	300-500V 0-120°C	ER400-1400, Prof	[122]
CAIBE	Cl_2/Ar	50-250°C, 300V	ER0-25000, Prof, Rough	[119]
CAIBE	Ar, I_2	3keV, conc	ER3000-12000, Rough	[126]
CAIBE	BCl_3,Cl_2,IBr_3,Ar	50-12-°C, 400V, 0-60°	ER400-750, Prof	[125]
CAIBE	BCl_3,Cl_2,IBr_3,Ar	50-12-°C, 400V, conc	Prof	[124]
CAIBE	Cl_2, Ar	50-300°C, 500V	ER0-30000, Prof	[123]
CAIBE	Cl_2, Ar	75-250°C, 500V	ER5000-17500, Prof	[121]
CAIBE	Cl_2, HCl, Ar	100-325°C, 500V	ER2000-4000, Prof	[120]
CAIBE	Br, Ar	25-200°C 500V	ER0-1500, Prof	[114]
RIBE	Cl_2	100-800V 100-200°C	ER100-2000, Prof	[117]
RIBE	$CH_4/H_2/N_2$	100-700V	ER0-650, Prof, Yield	[118]
RIBE	N_2,N_2/O_2	250-1000V, angle, conc	ER100-1200, Provile	[130]
RIBE	Cl_2	500-1500V 200°C	Prof, Damage	[115]
RIBE	CH_4/H_2	300V 20°	Prof, Damage	[112]
RIBE	Cl_2	80-340°C 1keV	ER300-20000, Prof, Rough	[115]
RIBE,C	CH_4/H_2/Ar/N_2	50-450V Ex-190 -500V	ER150-1200, Prof	[129]
RBE	Cl_2, HCl	50-250°C	ER1500, E_A 55$\pm$15kcal/mol	[127]
RBIBE	Cl_2	125-200°C 300V	ER10000, Prof	[128]

REFERENCES

[1] B.A. Morrow and A.J. Mcfarlan. Chemical reactions at silica surfaces. *J. Non-Crystal Solids*, 120:61–71, 1990.

[2] J. Proost, E. Kondoh, G. Vereecke, M. Heyns, and K. Maex. Critical role of degassing for hot aluminum filling. *J. Vac. Sci. Technol. B*, 16(4):2091–2098, 1998.

[3] J. Proost, M. Baklanov, K. Maex, and L. Delaey. Compensation effect during water desorption from siloxane-based spin-on dielectric thin films. *J. Vac. Sci. Technol. B*, 18(1):303–306, 2000.

[4] A. Feng, B.J. McCoy, Z.A. Munir, and D.E. Cagliostro. Water adsorption and desorption kinetics on silica insulation. *J. Colloid Interface Sci.*, 180:276–284, 1996.

[5] H.F. Winters. Physical sputtering: A discussion of experiment and theory. In M. Kaminsky, editor, *Radiation effects on solid surfaces: a symposium*. American Chemical Society, Washington, 1976.

[6] P. Sigmund. Sputtering by ion bombardment: Theoretical concepts. In R. Behrisch, editor, *Sputtering by Particle Bombardment I*. Springer-Verlag Berlin Heidelberg, Berlin, 1981.

[7] O. Auciello and D. L. Flamm. *Plasma diagnostics*. Academic Presses, Inc., San Diego, 1989.

[8] H. M. Mott-Smith and Irving Langmuir. The theory of collectors in gaseous discharges. *Phys. Rev.*, 28:727–763, 1926.

[9] J. Laframboise. Theory of cylindrical and spherical langmuir probes in a collisionless plasma at rest. In J. H. de Leeuw, editor, *Rarefield gas dynamics*. Academic presses, Inc, New York, 1965.

[10] V.A. Godyak, R. B. Piejak, and B. M. Alexandrovich. Measurements of electron energy distribution in low-pressure rf discharges. *Plasma Sources Sci. Technol.*, 1:36–58, 1992.

[11] N. Hershkowitz. How langmuir probes work. In O. Auciello and D. L. Flamm, editors, *Plasma Diagnostics*. Academic presses, Inc., New York, 1988.

[12] F. F. Chen. Electric probes. In R. H. Huddlestone and S. L. Leonard, editors, *Plasma diagnostic techniques*. Academic presses, Inc, New York, 1965.

[13] M. B. Hopkins. Langmuir probe measurements in the gaseours electronics conference rf reference cell. *J. Res. Natl. Inst. Stand. Technol.*, 100:415–425, 1995.

[14] L. J. Overzet and M. B. Hopkins. Comparison of electron-density measurements made using a langmuir probe and microwave interferometer in the gaseous electronics conference reference reactor. *J. Appl. Phys.*, 74(7):4323–4330, 1993.

[15] J S Kim, M. V. V. S. Rao, M. A. Cappelli, S. P. Sharma, and M. Meyyappan. Mass spectrometric and langmuir probe measurements in inductively coupled plasmas in ar, chf_3/ar and chf_3/ar/o_2 mixtures. *Plasma Sources Sci. Technol.*, 10:191–204, 2001.

[16] M. V. V. S. Rao, S. P. Sharma, B. A. Cruden, and M. Meyyappan. Langmuir probe and mass spectrometric measurements in inductively coupled cf_4 plasmas. *Plasma Sources Sci. Technol.*, 11:69–76, 2002.

[17] M.V. Malyshev and V. M. Donnelly. Trace rare gases optical emission spectroscopy: Nonintrusive method for measuring electron temperatures in low-pressure, low-temperature plasmas. *Phys. Rev. E*, 60(5):6016–6029, 1999.

[18] J.K. Olthoff and K.E. Greenberg. The gaseous electronics conference rf reference cell-an introduction. *J. Res. Natl. Inst. Stand. Technol.*, 100:327–339, 1995.

[19] J. Hopwood, C. R. Guarnieri, S. J. Whitehair, and J. J. Cuomo. Langmuir probe measurements of a radio frequency induction plasma. *J. Vac. Sci. Technol. A*, 11(1):152–156, 1992.

[20] M. B. Hopkins and W. G. Graham. Langmuir probe technique for plasma parameter measurement in a medium density discharge. *Rev. Sci. Instrum.*, 57(9):2210–2217, 1986.

[21] J. V. Scanlan and M. B. Hopkins. Langmuir probe measurements of the electron energy distribution function in radio-frequency plasmas. *J. Vac. Sci. Technol. A*, 10(4):1207–1211, 1992.

[22] C. Lai, R. A. Breun, P. W. Sandstrom, A. E. Wendt, and N. Hershkowitz. Langmuir probe measurements of electron temperature and density scaling in multidipole radio frequency plasmas. *J. Vac. Sci. Technol. A*, 11(4):1199–1205, 1993.

[23] A. P. Paranjpe, J. P. McVittie, and S. A. Self. A tuned langmuir probe for measurements in rf glow discharges. *J. Appl. Phys.*, 67(11):6718–6727, 1990.

[24] G. Neumann and U. Banziger. Plasma-density measurements by microwave interferometry and langmuir probes in an rf discharge. *Rev. Sci. Instrum.*, 64(1):19–25, 1993.

[25] W. G. Graham, C. M. O. Mahony, and P. G. Steen. Electrical and optical characterisation of capacitively and inductively coupled gec reference cells. *Vacuum*, 56:3–8, 2000.

[26] G. Franz. Comprehensive analysis of chlorine-containing capacitively coupled plasmas. *J. Vac. Sci. Technol. A*, 23(3):369–387, 2005.

[27] A. Von Engel and M. A. D. Sc. *Ionized gases*. Oxford University press, Great Britan, 1965.

[28] M. A. Lieberman and A. J. Lichtenberg. *Principles of plasma discharges and materials processing*. John Wiley and Sons, Inc., New York, 1994.

[29] J. P. Boeuf and T. Letardi. Fundamental properties of rf glow discharges: An approach based on self-consistent numberical models. In M. Capitelli and J. N. Bardsley, editors, *Nonequilibrium processes in Partially Ionized Gases*, 1989.

[30] V.A. Godyak and R. B. Piejak. Abnormally low electron energy and heating-mode transition in a low-pressure argon rf discharge at 13.56mhz. *Phys. Rev. Lett.*, 65(8):996–999, 1990.

[31] V.A. Godyak, R. B. Piejak, and B. M. Alexandrovich. Electron energy distribution function measurements and plasma parameters in inductively coupled argon plasma. *Plasma Sources Sci. Technol.*, 11:525–543, 2002.

[32] E. Abdel-Fattah and H. Sugai. Electron heating mode transition observed in a very high frequency capacitive discharge. *Appl. Phys. Lett.*, 83(8):1533–1535, 2003.

[33] P. Bletzinger. Experimental characteristics of rf parallel-plate discharges: Influence of attaching gases. *J. Appl. Phys.*, 67(1):130–138, 1990.

[34] C. Lee and M. A. Lieberman. Global model of ar, o_2, cl_2, and ar/o_2 high-density plasma discharges. *J. Vac. Sci. Technol. A*, 13(2):368–380, 1995.

[35] C. Schaffnit, L. Thomas, F. Rossi, R. Hugon, and Y. Pauleau. Plasma diagnostics of r.f. pacvd of boron nitride using a bcl_3-n_2-h_2-ar gas mixture. *Surf. Coat. Technol.*, 98:1262–1266, 1998.

[36] L. Thomas, J. L. Jauberteau, I. Jauberteau, J. Aubreton, and A. Catherinot. Characterization of a argon-hydrogen microwave discharge used as an atomic hydrogen source. effect of hydrogen dilution on the atomic hydrogen production. *Plasma Chem. Plasma Proc.*, 17(2):193–206, 1997.

[37] H. Muta, M. Koga, N. Itagaki, and Y. Kawai. Numerical investigation of a low-electron-temperature ecr plasma in ar/n_2 mixtures. *Surf. Coat. Technol.*, 171:157–161, 2003.

[38] B. N. Ganguly and P. Bletzinger. Comparison of hydrogen atom density measurements in three types of discharges using h_2-n_2 gas mixtures. *J. Appl. Phys.*, 82(10):4772–4776, 1997.

[39] J. L. Jauberteau, I. Jauberteau, and J. Aubreton. Nh_3 and $nh_x < 3$ radicals synthesis downstream a microwave discharges sustained in an ar-n_2-h_2 gas mixture. study of surface reaction processes and determination of rate constants. *J. Phys. D: Appl. Phys.*, 35:665–674, 2002.

[40] Hongbin Zhu and Anthony J. Muscat. Selective control of chemical reactions with plasmas. Technical report, Department of Energy, 2004.

[41] A.M. Efremov, Dong-Pyo Kim, and Chang-II Kim. On mechanisms of argon addition influence on etching rate in chlorine plasma. *Thin Solid Films*, 435:232–237, 2003.

[42] M. A. Sobolewski. Current and voltage measurements in the gaseous electronics conference rf reference cell. *J. Res. Natl. Inst. Stand. Technol.*, 100:341–351, 1995.

[43] A. P. Paranjpe, J. P. McVittie, and S. A. Self. Scaling lasws for radio frequency glow discharges for dry etching. *J. Vac. Sci. Technol. A*, 8(3):1654–1662, 1990.

[44] M.M. Turner and M. B. Hopkins. Anomalous sheath heating in a low pressure rf discharge in nitrogen. *Phys. Rev. Lett.*, 69(24):3511–3514, 1992.

[45] D.L. Flamm. Mechanisms of silicon etching in fluorine- and chlorine-containing plasmas. *Pure&Appl. Chem.*, 62(9):1709–1720, 1990.

[46] H.H. Sawin. A review of plasma processing fundamentals. *Solid State Technol.*, 28(4):211–216, 1985.

[47] J.L. Vossen and W. Kern. *thin film processes*. Academic Press Inc., New York, 1978.

[48] G.A. Vawter. Ion beam etching of compound semiconductors. In R. H. Huddlestone and S. L. Leonard, editors, *Handbook of Advanced Plasma Processing Techniques*. Springer, Germany, 2000.

[49] J.M. Smith. *Chemical Engineering Kinetics*. McGraw-Hill, Inc., New York, 1981.

[50] J.W. Coburn and H. F. Winters. Ion- and electron-assisted gas-surface chemistry-an important effect in plasma etching. *J. Appl. Phys.*, 50(5):3189–3196, 1979.

[51] Y-Y. Tu, T.J. Chuang, and H. F. Winters. Chemical sputtering of fluorinated silicon. *Phys. Rev.*, 23(2):823–835, 1981.

[52] Ch. Steinbrucher. Reactive ion beam etching with chlorinated gases: Beam characterization and etching of aluminum. *J. Appl. Phys.*, 59(12):4151–4157, 1986.

[53] Ch. Steinbrucher. Reactive ion beam etching: Dissociation of molecular ions upon impact. *J. Vac. Sci. Technol. B*, 2(1):38–44, 1984.

[54] D. C. Gray, H.H. Sawin, and J.W. Butterbaugh. Quantification of surface film formation effects in fluorocarbon plasma etching of polysilicon. *J. Vac. Sci. Technol. B*, 9(3):779–785, 1991.

[55] J.P. Chang, J.C. Arnold, G.C.H. Zau, H.S. Shin, and H. H. Sawin. Kinetic study of low energy argon ion-enhanced plasma etching of polysilicon with atomic/molecular chlorine. *J. Vac. Sci. Technol. A*, 15(4):1853–1863, 1997.

[56] J-P. Locquet and E. Machler. Characterization of a radio frequency plasma source for molecular beam epitaxial growth of high-tc superconductor films. *J. Vac. Sci. Technol. A*, 10(5):3100–3103, 1992.

[57] K. Maex, M.R. Baklanov, D. Shamiryan, F. Iacopi, Z.S. Yanovitskaya, and S.H. Brongersma. Low dielectric constant materials for microelectronics. *J. Appl. Phys.*, 93(11):8793–8841, 2003.

[58] D. L. Keil, B. A. Helmer, and S. Lassig. Review of trench and via plasma etch issues for copper dual damascene in undoped and fluorine-doped silicate glass oxide. *J. Vac. Sci. Technol. B*, 21(5):1969–1985, 2003.

[59] Alexander E. Braun. Low-k bursts into the mainstream...incrementally. *semicond. Int.*, 28(5):41–46, 2005.

[60] S. Yang, J. C. H. Pai, C. S. Pai, G. Dabbagh, O. Nalamasu, E. Reichmanis, J. Seputro, and Y. S. Obeng. Processing and characterization of ultralow-dielectric constant organosilicate. *J. Vac. Sci. Technol. B*, 19(6):2155–2161, 2001.

[61] T. C. Chang, P. T Liu, Y. J. Mei, Y. S. Mor, T. H. Peng, Y. L. Yang, and S. M. Sze. Effects of h_2 plasma treatment on low dielectric constant methylsilsesquioxane. *J. Vac. Sci. Technol. B*, 17(5):2325–2330, 1999.

[62] S. Satyanarayana, R. McGowan, B. White, and S. Hosali. Damage mechanisms in porous low-*k* integration. *Semicond. Int.*, 28(6):63–72, 2005.

[63] M. A. Worsley, S. F. Bent, S. M. Gates, N. C. M. Fuller, W. Volksen, M. Steen, and T. Dalton. Effect of plasma interactions with low-*k* films as a function of porosity, plasma chemistry, and temperature. *J. Vac. Sci. Technol. B*, 23(2):395–405, 2005.

[64] B. Xie and A. J. Muscat. Silylation of porous methylsilsesquioxane films in supercritical carbon dioxide. *Microelec. Eng.*, 76:52–59, 2004.

[65] B. Xie and A. J. Muscat. Condensation of silanol groups in porous methylsilsesquioxane films using supercritical co_2 and alcohol cosolvents. *IEEE Trans. Semicond. Manufact.*, 17(4):544–553, 2004.

[66] C. H. Chen and F. S. Huang. Surface modification on low dielectric constant material–methylsilsesquioxane. *Thin solid films*, 441:248–254, 2003.

[67] E. Kondoh, T. Asano, A. Nakashima, and M. Komatu. Effect of oxygen plasma exposure of porous spin-on-glass films. *J. Vac. Sci. Technol. B*, 18(3):1276–1280, 2000.

[68] K. Yonekura, S. Sakamori, K. Goto, M. Matsuura, N. Fujiwara, and M. Yoneda. Investigation of ash damage to ultralow-k inorganic materials. *J. Vac. Sci. Technol. B*, 22(2):548–553, 2004.

[69] P. G. Clark, B. D. Schwab, J. W. Butterbaugh, H. J. Martinez, and P. Josh Wolf. Cleaning and restoring k value of porous msq films. *Semicond. Int.*, 9:46–52, 2003.

[70] Badih El-Kareh. *Fundamentals of semiconductor processing technologies*. Kluwer Academic Publishers, 3300 AH Dordrecht, The Netherlands, 1998.

[71] Y.H. Wang, R. Kumar D. Gui, and P.D. Foo. *Electrochem. Solid-State Lett.*, 6(1):F1–F3, 2003.

[72] Y.C. Quan, S. Yeo, C. Shim, J. Yang, and D. Jung. Significant improvement of electrical and thermal properties of low dielectric constant plasma polymerized paraxylene thin films by postdeposition h_2+he plasma treatment. *J. Appl. Phys.*, 89(2):1402–1404, 2001.

[73] Y.Y. Chen, J. Y. Kan, and I.S. Lin. Adhesion studies of low-k silsesquioxane. *Thin Solid Films*, 462-463:297–301, 2004.

[74] J.M. Shieh, K.C. Tsai, B.T. Dai, Y.C. Wu, and Y.H. Wu. Reduction of etching plasma damage on low dielectric constant fluorinated amorphous carbon films by multiple h_2 plasma treatment. *J. Vac. Sci. Technol. B*, 20(4):1476–1481, 2002.

[75] T. C. Chang, Y. S. Mor, P. T. Liu, T. M. Tsai, C. W. Chen, Y. J. Mei, F. M. Pan, W. F. Wu, and S. M. Sze. Preventing dielectric damage of low-k organic siloxane by passivation treatment. *Microelec. Eng.*, 60(3-4):469–475, 2002.

[76] G. Lucovsky. Hydrogen in amorphous silicon: local bonding and vibrational properties. *J. Non-crystal Solids*, 141:241–256, 1992.

[77] A. Gupta and G. N. Parsons. Bond strain, chemical induction, and oh incorporation in low-temperature (350-100 °c) plasma deposited silicon dioxide films. *J. Vac. Sci. Technol. B*, 18(3):1764–1769, 2000.

[78] Brian Smith. *Infrared Spectral Interpretation: A System Approach*. CRC Press LLC, Boca Raton, Florida, 1998.

[79] C.Y. Wang, Z.X. Shen, and J.Z. Zheng. *Appl. Spectrosc.*, 54:209–213, 2000.

[80] C.Y. Wang, Z.X. Shen, and J.Z. Zheng. *Appl. Spectrosc.*, 55:1347–1351, 2001.

[81] S. Wlodek, A. Fox, and D.K. Bohme. Gas-phase reactions of si^+ and $sioh^+$ with molecules containing hydroxyl groups: Possible ion-molecule reaction pathways toward silicon monoxide, silanoic acid, and trihydroxy-, trimethoxy-, and triethoxysilane. *J. Am. Chem. Soc.*, 109:6663–6667, 1987.

[82] S. W. Benson. *Thermochemical Kinetics*. John Wiley & Sons, New York, 1976.

[83] H.S.W. Massey and E.H.S. Burhop. *Electronic and ionic impact phenomena*. Oxford University Press, Amen House, London, 1952.

[84] O. Sneh and S. M. George. Thermal stability of hydroxyl groups on a well-defined silica surface. *J. Phys. Chem.*, 99:4639–4647, 1995.

[85] M. Delfino, W. Tsai, G. Reynolds, and M.E. Day. Hydrogenating silicon dioxide in an electron cyclotron plasma. *Appl. Phys. Lett.*, 63(25):3426–3428, 1993.

[86] W. Tsai, M. Delfino, M.E. Day, T. Sheng, B.C. Chung, and S. Salimian. Correlation of plasma and surface chemistry during electron cyclotron resonance hydrogen etching of native silicon oxide. *J. Vac. Sci. Technol. A*, 11(5):2525–2529, 1993.

[87] T. P. Pearsal. *Properties, processing and applications of Indium Phosphide*. INSPEC, The institution of electrical engineers, London, United Kingdom, 2000.

[88] C. Youtsey and I. Adesida. Plasma processing of iii-v materials. In R. H. Huddlestone and S. L. Leonard, editors, *Handbook of Advanced Plasma Processing Techniques*. Springer, Germany, 2000.

[89] S. Thomas III, K.K. Ko, and S.W. Pang. Monitoring inp and gaas etched in cl_2/ar using optical emission spectroscopy and mass spectrometry. *J. Vac. Sci. Technol. A*, 13(3):894–899, 1995.

[90] R.J. Shul, G.B. McClellan, R.D. Briggs, D.J. Rieger, S.J. Pearton, C.R. Abernathy, J.W. Lee, C. Constantine, and C. Barratt. High-density plasma etching of compound semiconductors. *J. Vac. Sci. Technol. A*, 15(3):633–637, 1997.

[91] J.W.Lee, E.S. Lambers, C.R. Abernathy, S.J. Pearton, R.J. Shul, F. Ren, W.S. Hobson, and C. Constantine. Inductively coupled plasma etching of iii-v semiconductors in cl_2-based chemistries. *Mat. Sci. Semicond. Proc.*, 1:65–73, 1998.

[92] Y.B. Hahn, D.C. Hays, H. Cho, K.B. Jung, C.R. Abernathy, S.J. Pearton, and R.J. Shul. Effect of inert gas additive species on cl_2 high density plasma etching of compound semiconductors part ii. inp, insb, ingap and ingaas. *Appl. Surf. Sci.*, 147:215–221, 1999.

[93] G.F. McLane, M.C. Wood, D.W. Eckart, J.W. Lee, K.N. Lee, S.J. Pearton, and C.R. Abernathy. Dry etching of ingap in magnetron enhanced bcl_3 plasmas. *J. Vac. Sci. Technol. A*, 15(3):622–625, 1997.

[94] T. Maeda, J.W. Lee, R.J. Shul, J. Han, J. Hong, E.S. Lambers, S.J. Pearton, C.R. Abernathy, and W.S. Hobson. Inductively coupled plasma etching of iii-v semiconductors in bcl_3-based chemistries ii. inp, ingaas, ingaasp, inas and alinas. *Appl. Surf. Sci.*, 143:183–190, 1999.

[95] U.K. Chakrabarti, F. Ren, S.J. Pearton, and C.R. Abernathy. Effect of substrate temperature on dry etching of inp, gaas, and algaas in iodine- and bromine-based plasmas. *J. Vac. Sci. Technol. A*, 12(4):1129–1133, 1994.

[96] J.W. Lee, J. Hong, E.S. Lambers, C.R. Abernathy, and S.J. Pearton. Dry etching of iii-v semiconductors in ibr/ar electron cyclotron resonanace plasmas. *J. Electron. Mat.*, 26(5):429–435, 1997.

[97] J.W. Lee, J. Hong, E.S. Lambers, and S.J. Pearton. Icl plasma etching of iii-v semiconductors. *J. Vac. Sci. Technol. B*, 15(3):652–656, 1997.

[98] H.Y. Chen, H.E. Ruda, and A.Z. Navarro. Inductively coupled plasma etching of inp using n_2/h_2. *J. Appl. Phys.*, 89(10):5322–5325, 2001.

[99] T.R. Hayes, M.A. Dreisbach, P.M. Thomas, and W.C. Dautremont-Smith. Reactive ion etching of inp using ch_4/h_2 mixtures: Mechanisms of etching and anisotropy. *J. Vac. Sci. Technol. B*, 7(5):1130–1140, 1989.

[100] Y. Feurprier, Ch. Cardinaud, and G. Turban. Influence of the gas mixture on the reactive ion etching of inp in ch_4-h_2 plasmas. *J. Vac. Sci. Technol. B*, 15(5):1733–1740, 1997.

[101] Y. Feurprier, Ch. Cardinaud, B. Grollear, and G. Turban. Etch product identification during ch_4-h_2 rie of inp using mass spectrometry. *Plasma Sources Sci. Techno.*, 6:561–568, 1997.

[102] Y. Feurprier, Ch. Cardinaud, and G. Turban. Surface modification and etch product detention during reactive ion enching of inp in ch_4-h_2 plasma. *Plasma Sources Sci. Techno.*, 6:334–342, 1997.

[103] J.E. Parmeter, R. J. Shul, A.J. Howard, and P.R. Miller. Treatment of inp in radio frequency h_2 and h_2/ch_4/ar plasmas: *in situ* compositional analysis, etch rates, and surface roughness. *J. Vac. Sci. Technol. B*, 14(6):3563–3574, 1996.

[104] J.S. Yu and Y.T. Lee. Parametric reactive ion etching of inp using cl_2 and ch_4 gases: effects of h_2 and ar addition. *Semicond. Sci. Technol.*, 17:230–236, 2002.

[105] D.L. Melville, J.G. Simmons, and D.A. Thompson. Identification of volatile products in low pressure hydrocarbon electron cyclotron resonance reactive ion etching of inp and gaas. *J. Vac. Sci. Technol. B*, 16(4):1823–1832, 1993.

[106] C. Constantine, D. Johnson, S.J. Pearton, U.K. Chakrabarti, A.B. Emerson, W.S. Hobson, and A.P. Kinsella. Plasma etching of iii-v semiconductors in ch_4/h_2/ar electron cyclotron resonance discharges. *J. Vac. Sci. Technol. B*, 8(4):596–606, 1990.

[107] S.J. Pearton, J.W. Lee, E.S. Lambers, J.R. Mileham, C.R. Abernathy, W.S. Hobson, F. Ren, and R.J. Shul. High microwave power electron cyclotron resonance etching of iii-v semiconductors in ch_4/h_2/ar. *J. Vac. Sci. Technol. B*, 14(1):118–125, 1996.

[108] J.A. Diniz, J.W. Swart, K.B. Jung, J. Hong, and S.J. Pearton. Inductively coupled plasma etching of in-based compound semiconductors in ch_4/h_2/ar. *Solid-State Electronics*, 42(11):1947–1951, 1998.

[109] S. Thomas III and J.J. Brown. Dry etching of inp vias. In R. H. Huddlestone and S. L. Leonard, editors, *Handbook of Advanced Plasma Processing Techniques*. Springer, Germany, 2000.

[110] Y. Feurprier, Ch. Cardinaud, B. Grolleau, and G. Turban. Proposal for an etching mechanism of inp in ch_4-h_2 mixtures based on plasma diagnostics and surface analysis. *J. Vac. Sci. Technol. A*, 16(3):1552–1559, 1998.

[111] L. Houlet, A. Rhallabi, and G. Turban. Microscopic modeling of inp etching in ch_4-h_2 plasma. *J. Vac. Sci. Technol. A*, 17(5):2598–2606, 1999.

[112] N. Bouadma and J. Semo. 1.3-μm gainasp/inp buried-ridge-structure laser and its monolithic integration with photodetector using reactive ion beam etching. *J. Lightwave Technol.*, 12(5):742–748, 1994.

[113] G. A. Vawter and C. H. Ashby. Reactive-ion-beam etching of inp in a chlorine-hydrogen mixture. *J. Vac. Sci. Technol. B*, 12(6):3374–3377, 1994.

[114] J.M. Rossler, Y. Royter, D.E. Mull, W.D. Goodhue, and C.G. Fonstad. Bromine ion-beam-assisted etching of inp and gaas. *J. Vac. Sci. Technol. B*, 16(4):1012–1017, 1998.

[115] T. Yoshikawa, S. Kohmoto, M. Anan, N. Hamao an dM. Baba, N. Takado, Y. Sugimoto, M. Sugimoto, and K. Asakawa. Chlorine-based smooth reaction ion beam etching of indium-containing iii-v compound semiconductor. *Jpn. J. Appl. Phys. pt. 1*, 31(12B):4381–4386, 1992.

[116] T. Yoshikawa, Y. Sugimoto, Y. Sakata, T. Takeuchi, M. Yamamoto, H. Hotta, and S. Kohmoto. Smooth etching of various iii/v and ii/vi semicondutors by cl_2 reactive ion beam etching. *J. Vac. Sci. Technol. B*, 14(3):1764–1772, 1996.

[117] T. Tadokoro, F. Koyama, and K. Iga. A study on etching parameters of a reactive ion beam etch for gaas and inp. *Jpn. J. Appl. Phys.*, 27(3):389–392, 1988.

[118] J. R. Sendra and J. Anguita. Reactive ion beam etching of indium phosphide in electron cyclotron resonanace plasma using methane/hydrogen/nitrogen mixtures. *Jpn. J. Appl. Phys. pt. 2*, 33(3A):L390–L393, 1994.

[119] C. Youtsey, R. Grundbacher, R. Panepucci, and I. Adesida. Characterization of chemically assisted ion beam etching of inp. *J. Vac. Sci. Technol. B*, 12(6):3317–3321, 1994.

[120] C.Youtsey and I. Adesida. A comparative study of cl_2 and hcl gases for the chemically assisted ion beam etching of inp. *J. Vac. Sci. Technol. B*, 13(6):2360–2365, 1995.

[121] S. Dzioba, J.P.D. Cook, T.V. Herak, S. Livermore, M. Yound, R. Rousina, and S. Jatar. Wafer scale processing of ingaasp/inp lasers. *J. Vac. Sci. Technol. B*, 12(4):2848–2851, 1994.

[122] K.M. Eisele, J. Daleiden, and J. Ralston. Low temperature chemically assisted ion-beam etching processes using cl_2, ch_3, and ibr_3 to etch inp optoelectronic devices. *J. Vac. Sci. Technol. B*, 14(3):1780–1783, 1996.

[123] C. Youtsey, I. Adesida, J.B.D. Soole, M.R. Amersfoort, H.P. Leblanc, N.C. Andreadakis, A. Rajhel, C. Caneau, M. A. Koza, and R. Bhat. Fabrication of inp-based wavelength division multiplexing arrayed waveguide filters using chemically assisted ion beam etching. *J. Vac. Sci. Technol. B*, 14(6):4091–4095, 1996.

[124] J. Daleiden, K. Eisele, R.E. Sah, K.H. Schmidt, and J.D. Ralston. Chemical analysis of a cl_2/bcl_3/ibr_3 chemically assisted ion-beam etching process for gaas and inp laser-mirror fabrication under cryo-pumped ultrahigh vacuum conditions. *J. Vac. Sci. Technol. B*, 13(5):2022–2024, 1995.

[125] J. Daleiden, K. Czotscher, C. Hoffmann, R. Kiefer, S. Klussmann, S. Muller, A. Nutsch, W. Pletschen, S. Weisser, G. Trankle, J. braunstein, and G. Weimann. Sidewall slope control of chemically assisted ion-beam etched structures in inp-based materials. *J. Vac. Sci. Technol. B*, 16(4):1864–1866, 19948.

[126] L.M. Bharadwaj, P. Bonhomme, J. Faure, G. Balossier, and R. P. Bajpi. Chemically assisted ion beam etching of inp and insb using reactive flux of iodine and ar^+ beam. *J. Vac. Sci. Technol. B*, 9(3):1440–1444, 1991.

[127] D.G. Lishan and E. L. Hu. Cl_2 and hcl radical beam etching of gaas and inp. *Appl. Phys. Lett.*, 56(17):1667–1669, 1990.

[128] D.G. Yu, E. L. Hu, and G. Hasnain. Radical beam ion-beam etching of inalas/inp using cl_2. *J. Vac. Sci. Technol. B*, 12(6):3378–3381, 1994.

[129] C. F. Carlstrom, G. Landgren, and S. Anand. Low energy ion beam etching of inp using methane chemistry. *J. Vac. Sci. Technol. B*, 16(3):1018–1023, 1998.

[130] W. Katzschner, U. Niggebrugge, R. Loffler, and H. Schroter-Janssen. Reactive ion beam etching of inp with n_2 and n_2/o_2 mixtures. *Appl. Phys. Lett.*, 48(3):230–232, 1986.

[131] J.B. Malherbe and W.O. Barnard. Preferential sputtering of inp: an aes investigation. *Surf. Sci.*, 255:309–320, 1991.

[132] T. Holstein. Energy distribution of electrons in high frequency gas discharges. *Phys, Rev.*, 70(5–6):367–384, 1946.

[133] H. Dreicer. Electron velocity distribution in a partially ionized gas. *Phys, Rev.*, 117(2):343–354, 1960.

[134] R. Behrisch. Introduction and overview. In R. Behrisch, editor, *Sputtering by Particle Bombardment I*. Springer-Verlag Berlin Heidelberg, Berlin, 1981.

[135] Y.Yamamura, N. Matsunami, and N. Itoh. Theoretical studies on an empirical formula for sputtering yield at normal incidence. *Radiation Effects*, 71:65–86, 1983.

[136] Y. Yamamura and J. Bohdansky. Few collisions approach for threshold sputtering. *Vacuum*, 35(12):561–571, 1985.

[137] J. Bohdansky, J. Roth, and H.L. Bay. An analytical formula and important parameters for low-energy ion sputtering. *J. Appl. Phys.*, 51(5):2861–2865, 1980.

[138] J. Bohdansky. A universal relation for sputtering yield of monatomic solids at normal ion incidence. *Nucl. Instrum. Methods Phys. Res., Sect. B*, 2:587–591, 1984.

[139] G. Betz and G.K. Wehner. Sputtering of multicomponent materials. In *Sputtering by Particle Bombardment II*. Springer-Verlag Berlin Heidelberg, 1981.

[140] B. J. Garrison. Preferential sputtering of binary compounds: A model study. *Surf. Sci.*, 114:23–37, 1982.

[141] C.S. Whelan, T.E. Kazior, and K. Y. Hur. High rate ch_4:h_2 plasma etch processes for inp. *J. Vac. Sci. Technol. B*, 15(5):1728–1732, 1997.